Title
Stable Isotope Studies of Meteorites with Applications to Terrestrial Planet Formation and Evolution

Author
Jordan, Michelle

Publication Date
2017

Peer reviewed|Thesis/dissertation

UNIVERSITY OF CALIFORNIA

Los Angeles

Stable Isotope Studies of Meteorites with Applications to Terrestrial Planet Formation and Evolution

A dissertation submitted in partial satisfaction of the requirements for the degree Doctor of Philosophy in Geochemistry

by

Michelle Kay Jordan

2017

ABSTRACT OF THE DISSERTATION

Stable Isotope Studies of Meteorites with Applications to

Terrestrial Planet Formation and Evolution

by

Michelle Kay Jordan

Doctor of Philosophy in Geochemistry

University of California, Los Angeles, 2017

Professor Edward Donald Young, Chair

Stable isotopes serve as tracers of processes. Through analysis of the stable isotope compositions of meteorites, we can look back in time and learn about the conditions present in our nascent Solar System as well as the processes that were occurring. Here we characterize aspects of terrestrial planet formation and evolution using stable isotopes as our tool.

To understand how the first rocky material in our Solar System formed, we measure the isotopic compositions of several major rock-forming elements in the oldest surviving solids that formed in the Solar System (calcium-aluminum-rich inclusions). Measurements of δ^{25}Mg, δ^{29}Si, δ^{44}Ca, δ^{49}Ti, and anomalous ^{50}Ti in these refractory inclusions indicate that CAIs are not primary condensates, but instead, aggregates of pre-existing materials. Furthermore, they display signs of

heterogeneity, which are echoes of larger scale heterogeneity that existed in the precursor material from which they formed. The compositions of CAIs are consistent with averaging of the precursor material; this averaging has the effect of dampening the heterogeneity exhibited by the precursor material.

We also use stable isotopes to understand the nature of core formation in planetesimals. Measurements of the iron isotopic composition, δ^{57}Fe, of differentiated aubrite, iron, and chondrite meteorites allow us to form a more complete picture of core formation. The δ^{57}Fe of the metal and silicate phases in aubrite meteorites indicate that the metallic phase is enriched in ^{57}Fe/^{54}Fe. The magnitude of this fractionation cannot explain the observed difference in the compositions of iron meteorites and chondrites. Instead, the elevated ^{57}Fe/^{54}Fe of iron meteorites relative to chondrites, is likely due to evaporation and not core-mantle differentiation.

The dissertation of Michelle Kay Jordan is approved.

Bradley M. Hansen

Kevin D. McKeegan

Edwin Arthur Schauble

Edward Donald Young, Committee Chair

University of California, Los Angeles

2017

Table of Contents

List of Figures

List of Tables

ACKNOWLEDGEMENTS

Chapter 1 is a version of Simon, J. I., Jordan, M. K., Tappa, M. J., Schauble, E. A., Kohl, I. E., and Young, E.D. 2017. Calcium and titanium isotope fractionation in refractory inclusions: Tracers of condensation and inheritance in the early solar protoplanetary disk. EPSL **472**: 277-288. DOI: 10.1016/j.epsl.2017.05.002.

Dr. Issaku Kohl's maintenance of the instrumentation and laboratory facilities at UCLA was essential to the success of the research presented here. His assistance with data collection for several of the CAI samples as well as helpful scientific discussions are also incredibly appreciated.

The collaboration with Dr. Justin Simon allowed for the collection of calcium isotope data that was significant to the study of CAIs and the early Solar System. I thank Justin for his extensive contribution to this research as well as his academic mentoring.

Michael Tappa is thanked for the facility training at NASA-JSC, assistance with the development of Ti solution chemistry, processing of CAI samples, and Ca analyses.

Kaitlyn McCain is thanked for her contribution to the sample characterization of and data collection for the CAIs. Her work on the SEM has greatly improved our knowledge of the samples.

Haolan Tang is thanked for the collection of the carbonaceous chondrite data as well as her help in establishing a successful wet chemistry procedure for purifying Fe.

Prof. Edwin Schauble has provided theoretical knowledge and useful discussions for all the research presented in this dissertation. I thank him immensely for contributing to my understanding of isotope geochemistry and the advancement of this research.

I would like to express my gratitude to my additional committee members Prof. Brad Hansen and Prof. Kevin McKeegan. I thank you for your time and thoughtfulness over the years. I would like to particularly thank Kevin for his perspective and suggestions for bettering my research.

Finally, I would like the thank my advisor, Prof. Edward Young. He has fostered a research group that explores a diverse and innovative range of topics in isotope geochemistry and I thank him for the opportunity to be a part of this group. His guidance and intellectual contribution to the research presented here is invaluable.

Michelle Kay Jordan

Education

University of California, Los Angeles. Los Angeles, CA
Master of Science in Geochemistry, 2014

Boston University. Boston, MA
Bachelor of Arts with distinction in Earth Sciences; minor in Economics, 2009

Research and Teaching Experience

2017 *Teaching Fellow*; Dept. of Undergraduate Education Initiatives, UCLA

2016-2017 *Teaching Fellow*; Dept. of Earth, Planetary, and Space Sciences, UCLA

2014 *Researcher*; Center for Isotope Cosmochemistry & Geochronology, Astromaterials Research and Exploration Science Division, NASA-JSC

2010-2015 *Teaching Assistant*; Dept. of Earth, Planetary, and Space Sciences, UCLA

2010-2017 *Graduate Student Researcher*; Dept. of Earth, Planetary, and Space Sciences, UCLA

2008-2009 *TIMS Facility Laboratory Assistant, Independent Work for Distinction*; Dept. of Earth Sciences, Boston University

2008-2009 *Coastal Group Laboratory Assistant*, Dept. of Earth Sciences, Boston University

Publications

Simon, J. I., Jordan, M. K., Tappa, M. J., Schauble, E. A., Kohl, I. E., and Young, E.D. 2017. Calcium and titanium isotope fractionation in refractory inclusions: Tracers of condensation and inheritance in the early solar protoplanetary disk. EPSL **472**: 277-288.

Young, E. D., Manning, C. E., Schauble, E. A., Shahar, A., Macris, C. A., Lazar, C., and Jordan, M. 2015. High temperature equilibrium isotope fractionation of non-traditional stable isotopes: Experiments, theory, and applications. Chem. Geol. **395**: 176-195

Oral Presentations

Jordan, M. K., Kohl, I. E., McCain, K. A., Simon, J. I., and Young, E. D. 2017 Ti isotopes: Echoes of grain-scale heterogeneity in the protoplanetary disk. LPSC XLVIII, Abstract #3032

Jordan, M. K. and Young, E.D. 2016. Iron Isotope Constraints on Planetesimal Core Formation. AGU Annual Fall Meeting.

Jordan, M. K. and Young, E. D. 2016. Equilibrium metal-silicate Fe isotope fractionation and the implications for planetary differentiation. LPSC XLVII, Abstract #3032

Jordan, M. K., Kohl, I. E., Young, E. D., Simon, J. I., and Jacobsen, S. B. 2015. Comparing measured and modeled Ti isotope fractionation in CAI SJ101 and implications for the origin of CAIs. LPSC XLVI, Abstract #2472

Jordan, M. K., and Young, E. D. 2014 Equilibrium metal-silicate Fe isotope fractionation and the implications for differentiation in planetary bodies. LPSC XLV, Abstract #2318

Chapter 1: Calcium and titanium isotope fractionation in refractory inclusions: tracers of condensation and inheritance in the early solar protoplanetary disk

J. I. Simon[1], M. K. Jordan[2], M. J. Tappa[1*], E. A. Schauble[2], I. E. Kohl[2], and E. D. Young[2].

[1]Center for Isotope Cosmochemistry & Geochronology, Astromaterials Research and Exploration Science Division, NASA-Johnson Space Center, Houston, TX, USA. (Justin.I.Simon@NASA.gov)
[2]Department of Earth, Planetary, and Space Sciences, UCLA, Los Angeles, CA, USA.
*Now at Department of Earth and Environmental Sciences, Boston College, Chestnut Hill, MA, USA.

Abstract.

Measured and modeled Ca and Ti isotopic fractionation effects in a diverse suite of refractory inclusions are used to understand processes of condensation in the solar protoplanetary disk where they and their precursor materials formed. This coordinated approach reveals largely decoupled isotopic signatures and implies that few, if any, of the studied inclusions can be considered primary condensates. All studied inclusions are enriched in light Ca isotopes (~ -0.2 to -2.8 ‰/amu), but only two show correspondingly light Ti isotopes. Studied inclusions exhibit both heavy and light Ti isotope enrichments (~0.3 to -0.4 ‰/amu). These refractory element isotopic signatures, therefore, suggest admixture and reprocessing of earlier formed materials with distinct condensation histories. Along with coordinated measurements of ^{50}Ti isotopic anomalies, which span a range from ~0 to ~40 epsilon-unit excesses, the comparison of measured and modeled fractionation of Ca and Ti isotopes provides a powerful approach to understanding primitive nebular processes and environments in the protoplanetary disk. Remarkable evidence for Ca isotopic zoning within a typical Type B1 inclusion exemplifies the potential record of the earliest

solar nebula that is likely lost and/or overprinted in the isotopic compositions of more volatile elements (e.g., Mg, Si, and O) by later modification processes.

1.1. Introduction

Calcium-, aluminum-rich refractory inclusions (CAIs) are among the oldest surviving solids in the Solar System. Their chemical and isotopic compositions provide a record of the conditions present in the protoplanetary disk where they formed and guide our understanding of how solids formed in the solar nebula, an important step in the eventual process of planet building. Thermal events that drove evaporation and condensation in the solar nebula resulted in significant mass-dependent isotopic variations in CAIs (e.g., Clayton and Mayeda, 1977; Wasserburg et al., 1977; Niederer and Papanastassiou, 1984; Niederer et al., 1985; Davis et al., 1990; Nagahara and Ozawa, 2000; Richter et al., 2002; Shahar and Young, 2007; Yamada et al., 2006; Young et al., 1998). The magnitudes of these effects are primarily controlled by chemical volatility. While evaporation/ sublimation is well explained by both theory and experimental work to produce enrichments in the heavy isotopes that are often exhibited by the moderately refractory elements Mg and Si (e.g., Young et al., 2002), less is understood about the effects of condensation. Because the isotopic effects of condensation are likely to be complicated (e.g., Niederer and Papanastassiou, 1984 and Uyeda et al., 1991), it is unknown if any CAI is a primary condensate that retains evidence of its primordial formation history.

The approach of this study is to compare the isotopic signatures of the refractory elements Ca and Ti to each other and to moderately refractory elements more generally, and to evaluate the results in the context of a theoretical condensation model. Many existing CAI studies target the isotopic composition of an individual element, which upon comparison to the record of other

elements often reveal conflicting interpretations. Along with measured ^{50}Ti anomalies, these divergent signatures may indicate real differences in their formation and/or may reflect artifacts produced by comparing the compositions of early formed solids with unrelated histories. This uncertainty can be critically addressed by our coordinated multi-isotopic approach of a common suite of CAIs, which builds on the pioneering work of Niederer and Papanastassiou (1984), Niederer et al. (1985), and Papanastassiou and Brigham (1989). Additionally, our novel theoretical approach to the condensation problem affords a self-consistent model for Ca and Ti (as well as Mg and Si) that allows a direct comparison to the measured isotopic compositions of the studied CAIs. This comparison helps us evaluate the effects of condensation and the overall formation history of these objects. In particular, using Ca and Ti to understand the isotopic effect of condensation will allow us to more accurately assess the initial isotopic ratios of the more volatile Mg and Si potentially overprinted by later evaporation events. Furthermore, these results allow us to assess whether a given CAI is a primary condensate from a homogenous solar gas or instead represents a mixture of materials from a variety of early reservoirs. Thus, these results can be used to understand key nebular processes and environments in the protoplanetary disk that CAI compositions recorded as they formed.

1.2. Samples

A diverse group of 6 inclusions from two CV3 meteorites were studied. The suite of samples included: a Type A CAI (EK5-2-1R), a Type B1 CAI (AL4884), two fine-grained inclusions (3B3 and 461 B), and a forsterite-bearing Type B CAI SJ101 from Allende, and a "reworked" Type B CAI (Crucible) from Northwest Africa (NWA 2364). Ca isotope measurements were also performed on a range of planetary materials for reference, including an

Allende chondrule, terrestrial basalts and minerals (melilite and augite), and lunar basalts (Apollo samples 12051, 15555, 70035, 70215, 74205, 75015, and 75075). The Smithsonian mineral standards were prepared from rock fragments that were gently crushed, hand-picked, and imaged by SEM, to avoid mixed mineral phases, prior to subsequently being hand powdered and dissolved. The fine-grained 3B3 and 461 B, coarse-grained Type A EK5-2-1R, and chondrule all come from slabs cut from a single sample of Allende.

In general, the studied CAIs exhibit textures and mineralogy that are typical for their sub-type classifications. Exceptions include apparent "mélanges" of accessory refractory hibonite and perovskite (±spinel) within the melilite interior of Type A CAI EK5-2-1R (Figure 1.1) and the potentially reworked nature of Type B CAI Crucible (Friedrich et al., 2005). Similar to other coarse-grained Allende CAIs, EK5-2-1R exhibits some secondary sodalite and nepheline at the outer edge of its melilite interior. In Figure 1.1, EK5-2-1R appears to be about 3x3 mm, but this sample is a non-diametric slice of a previously much larger (~10x10 mm) inclusion (Harper et al., 1990). Crucible, 18 mm in its largest apparent diameter, is cup shaped (hence it has been called "the Crucible") and envelops a portion of the host chondrite (Friedrich et al., 2005). Crucible contains coarsely grained melilite, fassaite, and primary anorthite, with abundant euhedral spinel heterogeneously disturbed throughout. Some anorthite has been altered to secondary melilite (Friedrich et al., 2005). AL4884 is an ~6x10 mm CAI with a heavily microfaulted surface that has been studied extensively by Bullock et al. (2013). The core of AL4884 contains the typical abundant coarse-grained melilite, fassaite, and anorthite of Type B1 inclusions. Its melilite mantle is ~250-500 μm thick and consists mainly of gehlenitic melilite and minor spinel (Bullock et al., 2013). The microfractures across AL4884 are filled with secondary alteration and there are patchy areas of alteration within the CAI consistent with at least one previous secondary mineralization

event. AL4884 was selected for this work in part because of its large size and in part because its pyroxene is particularly Ti-rich (~5-17 wt.% TiO_2, Bullock et al. (2013). SJ101 is a very large ~15x25 mm sized, forsterite-bearing Type B CAI described in detailed by Petaev and Jacobsen (2009). It consists of coarse-grained grossular, melilite, anorthite, and clinopyroxene crystals separated by sinuous finer-grained forsterite-, clinopyroxene-rich bands. Small spinel grains enclosed in the silicates are distributed homogenously throughout the inclusion. Minimal amounts of andradite and nepheline are observed in cavities and at the edge of the inclusion. The image shown of the fine-grain inclusion 3B3 in Figure 1.2 is a fragment of a large CAI that was originally at least ~10x10 mm in size. It is comprised of ~5-10 μm sized spinel, hibonite, and alkali-rich melilite. The fine-grained CAIs lack obvious Wark-Lovering rims (Wark and Lovering, 1977). Fine-grained CAI 461 B is relatively small, only about ~250x500 μm in size. Its hibonite 'mantle' is ~100 μm thick. It contains spinel and hibonite grains within its aggregate interior.

1.3. Methods

1.3.1 Theoretical mass-dependent fractionation models

We considered the isotopic consequences of condensation from a nebular gas in terms of the kinetics of condensation, the degree of undercooling, and potential reservoir effects. While it is possible to directly measure fractionation factors for evaporation (α_{evap}) in the laboratory, this is not the case for condensation fractionation factors (α_{cond}). Instead, a condensation model is needed to indirectly obtain α_{cond}. Invoking the law of mass action, we make use of the relationship $\alpha_{\mathrm{eq}} = \frac{\alpha_{\mathrm{cond}}}{\alpha_{\mathrm{evap}}}$. Equilibrium fractionation factors (α_{eq}) can be calculated, allowing us to solve for α_{cond}. This model considers the possibility for near-equilibrium insertion of condensing atoms and molecules where undercooling is minimal.

Kinetic fractionation during condensation depends upon the relative roles of collisional frequency (between molecular species and the grain surface), compared to the ability of a molecule to incorporate into the condensed phase structure (Simon and DePaolo, 2010). Partition of the lighter isotopes into the condensates is favored when collisional frequency is the dominant controlling effect.

Ultimately, the relative importance of equilibrium versus the potentially much larger kinetic effects in the isotope fractionation depends on the degree of "overstepping" thermodynamic equilibrium as measured by the saturation index $S_i = P_i/P_{i,eq}$ with $S_i > 1$ implying condensation. S_i can be equated with a temperature difference (i.e., undercooling) from the equilibrium condensation temperature using the Van't Hoff equation and the enthalpy for the condensation reaction (Simon and DePaolo, 2010). Combining these we arrive at a model for fractionation during condensation:

$$\alpha_{\mathrm{cond}} = \frac{\alpha_{\mathrm{eq}}\alpha_{\mathrm{kin}}\mathrm{S_i}}{\alpha_{\mathrm{eq}}(\mathrm{S_i}-1)+\alpha_{\mathrm{kin}}} \tag{1.1}$$

where

$$\alpha_{\mathrm{kin}} = \alpha_{\mathrm{evap}}\alpha_{\mathrm{eq}}\sqrt{\frac{m_i}{m_i'}} \tag{1.2}$$

with m_i being the mass of the lighter isotopic species of interest and m_i' being the mass of the heavier isotopic species.

1.3.2 Analytical Approaches

1.3.2.1Ca isotope analysis by thermal ionization mass spectrometry

Mass dependent Ca isotopic compositions are measured by a ^{42}Ca-^{48}Ca double spike method on a Thermo Fisher Scientific Triton thermal ionization multi-collector mass spectrometer

(TIMS) housed in the Center for Isotope Cosmochemistry and Geochronology at NASA Johnson Space Center. The specific procedures including sample loading and analysis methodologies are similar, but improved on those described by Simon and DePaolo (2010). About 3 μg of separated calcium is loaded in nitrate form with H_3PO_4 on outgassed double Re filaments. A multi-step cup configuration sequence is used in order to obtain ^{40}Ca, ^{42}Ca, ^{43}Ca, ^{44}Ca, and ^{48}Ca ion beams using Faraday collectors with 10^{11} Ω resistors and to obtain potential mass interferences using electron multipliers. The magnitudes of potential interferences from ^{40}K and ^{48}Ti (determined by measuring ^{39}K and ^{49}Ti, respectively) are found to be insignificant; no corrections were applied. Each analysis consists of 200 cycle measurements. Instrumental mass discrimination corrections based on the difference between the sample subtracted ^{42}Ca/^{48}Ca ratio and the double tracer composition are calculated offline for each cycle to account for possible changes in the mass discrimination in the spectrometer over the duration of each ~3 hour analysis. An exponential law is used for the instrumental mass discrimination corrections. Given that the magnitude of Ca isotopic anomalies in common Types A and B inclusions are small (Niederer and Papanastassiou, 1984; Simon et al., 2009; Shiller et al., 2015) we assume that their Ca compositions are normal, except for the mass fractionation effects. This study follows the approach of Simon and DePaolo (2010) who report sample measurements relative to the normal value of most planetary materials (igneous materials from Earth, Moon, Mars, and differentiated achondrites). After accounting for the spike and mass discrimination, the "absolute" ^{40}Ca/^{44}Ca in the sample is normalized so that ^{42}Ca/^{44}Ca = 0.31221 (Russell et al., 1978) and expressed in delta notation where:

$$\delta^{44}\mathrm{Ca}/^{40}\mathrm{Ca} = \left[\frac{\left({}^{44Ca}/_{40Ca}\right)_{sample}}{\left({}^{44Ca}/_{40Ca}\right)_{normal}} - 1\right] \times 1000 \qquad (1.3).$$

In this notation, positive values indicate enrichments in the heavier Ca isotopes and negative values indicate enrichments in the lighter isotopes. Measured seawater, BCR-1 & 2, and SRM915a & b standards, as well as, melilite and augite terrestrial minerals (from the Smithsonian Institute) yielded their expected values (Table 1). All samples were replicated and yielded internal precisions similar to the ~0.04 to 0.06‰ 2 standard errors (SE) of the rock standards. The weighted averages of replicate measurements and their 2 SE are included in Table 1.

1.3.2.2 Ti isotope analysis by laser ablation multiple-collector inductively coupled plasma-source mass spectrometry

Titanium isotope analyses were conducted using the LA-MC-ICPMS (Thermo Fisher Scientific Neptune^{TM}) housed at UCLA. Most analyses in the CAIs are dominated by the Ti-bearing pyroxene phase. Some measurements also include pevoskite and minor hibonite as well. All mass-dependent $^{49}Ti/^{47}Ti$ isotope ratios measured in this study are reported in per mil deviations ($\delta^{49}Ti/^{47}Ti$) from a terrestrial rutile reference material (USNM 83191).

$$\delta^{49}Ti/^{47}Ti = \left[\frac{\left({}^{49Ti}/_{47Ti}\right)_{sample}}{\left({}^{49Ti}/_{47Ti}\right)_{normal}} - 1\right] \times 1000 \qquad (1.4).$$

It is generally agreed that in common Types A and B inclusions $^{49}Ti/^{47}Ti$ is effectively free from nuclear anomalies at the 0.1 ‰ level or greater (Zhang et al., 2011) and we have demonstrated that we can measure $^{49}Ti/^{47}Ti$ (Figure 1.4) free from matrix effects within our analytical precision of ~0.3 ‰ (2 SE). Ru and Mo doubly-charged interferences are well below detection and have no influence. The lack of matrix effects is illustrated here by comparing our UCLA Glass #5 (P10) standard (fassaite composition, previously measured for Ti isotopes by Chen et al., 2009) with pure TiO_2 (Figure 1.4); there is limited fractionation among terrestrial materials in general (< 0.1

‰, e.g., Zhang et al., 2011; Zhu et al., 2002) and we see no spurious fractionation between this fassaite glass and pure TiO_2.

There is a rich history of measurements of ^{50}Ti isotope effects in CAIs, including some recently reported results using laser ablation (Niederer et al., 1980, 1981, 1985; Papanatassiou and Brigham, 1989; Niemeyer, 1988; Chen et al., 2009; Leya et al., 2009; Trinquier et al., 2009; Zhang et al., 2012; Williams et al., 2016). These studies find that mass-fractionation-corrected ^{50}Ti anomalies, expressed as ε^{50}Ti (parts per 10,000) in common Types A and B inclusions are generally between +2 and +15 with the most typical values near +10. Although laser ablation sampling of ^{50}Ti excesses has been reported (Williams et al., 2012) there are still no systematic *in situ* studies of potential correlations between mass-fractionation effects and the large ε^{50}Ti in CAIs. In order to measure ^{50}Ti/^{47}Ti excesses we peak strip interferences from ^{50}Cr and ^{50}V by monitoring ^{52}Cr and ^{51}V during each analysis and correcting for instrumental fractionation in the usual way (β exponents characterizing instrumental fractionation). The validity of this stripping approach can be seen by the accuracy and reproducibility of a range of standard materials, Figure 1.5.

Ion currents for $^{47}Ti^+$, $^{49}Ti^+$, $^{50}Ti^+$, $^{51}V^+$, and $^{52}Cr^+$ were measured for each laser run on Faraday collectors with 10^{11} Ω resistors. Each measurement comprises 10 cycles of 4s integrations. The mass resolving power (m/Δm) was 7000 or greater for these analyses. The effects of instrumental fractionation were corrected for by sample-standard bracketing. An instrumental mass fractionation factor, α_{inst}, was also calculated by comparing measured ^{49}Ti/^{47}Ti to a nominal ratio of 0.74500. This instrumental fractionation factor was used to derive an exponent β for the general fractionation law ($\alpha_{inst} = (m_2/m_1)^{\beta}$) that was then used for both V and Cr with the relationship $\beta = \ln(\alpha_{inst})/\ln(m_{49}/m_{47})$ where m_i refers to the atomic mass of interest. Typical values for α_{inst} and β for the operating conditions used in this study are 1.083 and 1.91, respectively. We

find that these values pertain for Fe as well as for Ti and are characteristic of instrumental conditions at UCLA for transition metals in this mass range. The Ti-derived fractionation law was applied to the measured $^{51}V^+$ and $^{52}Cr^+$ to derive $^{50}V^+$ and $^{50}Cr^+$ ion currents interfering with that for $^{50}Ti^+$. These interferences were subtracted from the mass/charge = 50 ion current to obtain the $^{50}Ti^+$ ion current.

An excimer laser with 193 nm wavelength and ~4 ns pulse length (Photon-Machines, Analyte.193) was operated at fluences of ~28 J/cm^2 for ablation. For this study the laser was operated at pulse repetition rates of between 1 and 6 Hz using spot sizes of 28 to 172 μm (typical ablation pit depths are ~ 25 to 30 μm), with the combination of pulse rate and spot size depending on the concentration of Ti. Tests of the effects of pulse rate and spot size showed no correlations with measured isotope ratios. The laser ablation sample chamber is flushed with He (0.29 L/min) and mixed with Ar (0.69 L/min) and N_2 (8 ml/min) in a mixing cell just prior to introduction into the plasma.

1.4. Analytical Results

All studied CAIs have $\delta^{44}Ca/^{40}Ca$ values less than "normal" planetary-like compositions (~0‰), similar to the isotopically "light" values reported in the early studies of Russell et al. (1978) and Neiderer et al. (1989) and more recently by Huang et al. (2012). These signatures are also consistent with the enriched light isotopic compositions in Eu, Sr, and Ba reported by Moynier et al. (2006, 2010, 2015). None of the objects studied in this work yield positive $\delta^{44}Ca/^{40}Ca$ values (cf. Niederer and Papanastassiou, 1984; the Type C inclusion of Huang et al., 2012). Measured CAI $\delta^{44}Ca/^{40}Ca$ values range from approximately -0.6 to -11.3‰ (a majority yielded values between -0.6 to –1.7‰) that are clearly resolved from measured planetary silicate materials

including the Allende chondrule (0.00±0.06‰, 2 SE), terrestrial basalts (-0.10±0.06‰, 2 SE), terrestrial melilite (-0.06±0.15‰, 2 SE), terrestrial augite (-0.03±0.06‰, 2 SE), and lunar basalts (0.02±0.03‰, 2 SE). The value measured for the second carbonate standard SRM915b was slightly less than planetary (-0.16±0.06‰, 2 SE) and IAPSO seawater standard was higher (0.79±0.16‰, 2 SE) as is expected. The CAIs exhibit values lower than the value measured herein for bulk Allende powder (-0.42±0.11‰, 2 SE) reported previously by Simon and DePaolo (2010);Valdes et al. (2014) (Figure 1.5, Table 1.1).

Due to their relatively large size, subsamples of Type B inclusions Crucible and AL4884 were obtained by micromilling. No resolvable difference was observed between the core and outer edge of Crucible, $\delta^{44}Ca/^{40}Ca$ = -0.57±0.02‰ (2 SE) and -0.66±0.14‰ (2 SE), respectively. However, a clear difference can be seen across AL4884, with the core yielding $\delta^{44}Ca/^{40}Ca$ = -1.66±0.08‰ (2 SE), outer core yielding -1.50±0.03‰ (2 SE), and the melilite mantle yielding $\delta^{44}Ca/^{40}Ca$ = -0.97±0.07‰ (2 SE; Figure 1.6). To our knowledge no evidence of intraCAI mass dependent Ca isotopic heterogeneity has been reported previously in any nebular material.

In contrast to the "light" $\delta^{44}Ca/^{40}Ca$ values measured, most measured $\delta^{49}Ti/^{47}Ti$ ratios in the studied CAIs have "normal" compositions, although small mass dependent Ti isotope effects exist. The Ti isotopic compositions of Crucible, AL4884, and SJ101 (i.e., $\delta^{49}Ti/^{47}Ti$ = 0.06 to 0.15‰), are unresolvable from a planetary value, see Figure 1.4. A similar value was measured for the accessory hibonite/perovskite/spinel mélange in EK5-2-1R (0.23±0.32‰, 2 SE). The primary phases within the interiors of EK5-2-1R and 461 B appear to exhibit slightly lower $\delta^{49}Ti/^{47}Ti$ values of about -0.40 and -0.70‰, respectively. The fine-grained CAI 3B3 has a slightly positive $\delta^{49}Ti/^{47}Ti$ value (0.64±0.10‰, 2 SE) that is resolvable from the normal planetary composition. It should be noted that measurements of Ti isotope mass fractionation in CAIs date

back to the early 1980's. Niederer et al. (1985) found CAIs to be between +0.2 to +1.0‰ per amu among both normal and FUN CAIs. However, reports at conferences of wider ranges in $^{49}Ti/^{47}Ti$ of -2.7 to +4.0 exist (Zhang et al., 2012).

Anomalous $^{50}Ti/^{47}Ti$ isotope effects ($\varepsilon^{50}Ti$) were also measured by laser ablation MC-ICPMS (UCLA). Most measured ^{50}Ti excesses were found to be ~6 to 13 epsilon units in the studied CAIs (Figure 1.5). The measured $\varepsilon^{50}Ti = 11.3\pm3.0$ (2 SE) for SJ101 and the unpublished TIMS analysis measured at NASA JSC, i.e., Harper et al. (1990) of the fine-grained CAI 3B3 of $\varepsilon^{50}Ti = 13.2\pm1.2$ (2 SE) represent typical values of the studied samples. These analyses are similar to those previously reported (see Figure 1.6). The first exception is EK5-2-1R that appears to show little to no $\varepsilon^{50}Ti$ effect (1.0±0.8, 2 SE), which is consistent with the $\varepsilon^{50}Ti$ value of 0.0±1.0 (2 SE) measured by TIMS. It is noteworthy that an average of just the spots dominated by major minerals appears to exhibit a resolvable excess (1.5±0.5, 2 SE), as they also appear isotopically "light" (see above). The second exception is 461 B that exhibits a large $\varepsilon^{50}Ti$ excess (41.6±5.2, 2 SE), which also exhibits a negative $\delta^{49}Ti/^{47}Ti$ value (Figure 1.6). This isotopic anomaly is the largest excess observed for common Type A and B CAIs, as opposed to spinel-hibonite inclusions (SHIBs), platy hibonite crystals (PLACs), and those that exhibit Fractionated and Unidentified Nuclear (FUN) isotopic properties (Wasserburg et al., 1977). Although extensive tests were made to demonstrate the validity of our peak-stripping and mass bias correction method, other investigations (e.g., Williams et al., 2016) have found that a high Ca/Ti ratio like that measured in 461 B (Figure 1.5, inset) can artificially enhance the $^{50}Ti/^{47}Ti$ ratio of up to ~10 epsilon units. The effect in question is much larger than 10 epsilon units and does not follow the expected linear relationship that an interference would produce.

1.5. Discussion

1.5.1 Condensation model for isotope fractionation

In order to calculate the isotope fractionation factors ($\alpha_{\mathrm{cond}} = R_{cond}/R_{vapor}$) needed to construct theoretical condensation model curves that can account for non-equilibrium conditions, one must consider multiple processes contributing to the fractionation. As outlined in Section 3.1, α_{cond} is a function of equilibrium fractionation factors (α_{eq}), fractionation associated with evaporation (α_{evap}) through the law of mass action, and fractionation related to gas phase transport ($\alpha_{\mathrm{trans}} = \sqrt{(m/m')}$). Equilibrium fractionation factors (α_{eq}) can be determined by thermodynamic considerations (e.g., Simon and DePaolo 2010). Values for α_{eq} between solid and vapor can be estimated from reduced partition function ratios (β), following the approach of Schauble (2011). The magnitude of fractionation is controlled mainly by the transformation from vapor to solid with the exact identity of the solid phase(s) being of less importance. For calcium models, we assume an α_{eq} for the simple reaction where Ca vapor condenses to silicate (i.e., diopside). At 1600 K, the Ca α_{eq} equates to 1.000477. This is justified because at realistic nebular temperatures and pressures Ca >> CaO (Zhang et al., 2014). For titanium models, we assume equilibrium between TiO and TiO_2 in the vapor phase and rutile. This leads to a Ti α_{eq} at 1600 K that is less than unity (0.999995). The relative abundances of the titanium gas species (TiO ~0.8 and TiO_2 ~0.2) are based on the equilibrium condensation calculations of the type described in Ebel and Grossman (2000). The α values empirically determined for evaporation (α_{evap}) for Ca (~0.9562) and Ti (~0.9880) come from Zhang et al. (2014). The α values associated with vapor transport (α_{trans}) assume collision frequency ratios for the vapor phase species involving the atomic masses in the case of calcium vapor (i.e., Ca α_{trans} = 0.953499) and the oxides TiO and TiO_2 for titanium vapor (i.e., Ti α_{trans} = 0.985246).

1.5.2 Isotopic reservoir effects related to distillation of nebular gas

Calculations combining equations 1-3 afford α_{cond} values that can be used to model the magnitude of Ca and Ti isotopic fractionation effects produced by condensation of nebular gas. Although these likely oversimplify the condensation process(es) that occurred in the early Solar System, they are illustrative. Using α_{cond} (e.g., from section 5.1), the magnitude of isotope fractionation that occurs as the result of the Rayleigh distillation process expected during condensation leads to the model curves shown in Figures 1.8, 1.9 and 1.11. For the sake of completion both bulk and instantaneous (in section 5.3) condensation models are considered. Substitution of α_{cond} into the typical bulk Rayleigh equation:

$$\delta = (\delta_0 + 1000)\left(\frac{(1-F^{\alpha_{cond}})}{(1-F)}\right) \qquad (4),$$

where *F* is the fraction of gas remaining shows the effects of condensation where early formed nebular materials are expected to record an increased degree of light isotopic enrichment due to the depletion of the heavy isotopes by prior vapor-gas fractionation (Figure 1.8). The computed relatively light Ca isotopic signatures are consistent with those measured in CAIs by Niederer and Papanastassiou (1984), Huang et al. (2012), and this study.

During equilibrium condensation (i.e., ~no undercooling), however, the Ca fractionation model calculations show that small positive mass dependent isotope effects of up to ~0.5‰ can be produced. Under equilibrium conditions there is a slight depletion of light isotopes induced by vapor-gas fractionation leading to a heavy isotope enriched gas reservoir (Figure 1.8, left panel). In the case of Ca this is an especially robust result as Ca bonded to other atoms will always favor the heavy isotopes relative to the atomic Ca (i.e., logarithms of the reduced partition functions are greater than zero). In the case of the Ti isotope fractionation models there is effectively no α_{eq}

contribution (α_{eq} = 0.999995) because Ti is bonded to oxygen in the dominant gas species, limiting differences in reduced partition function ratios. As a result, there are no heavy isotope enrichments in the condensates at equilibrium as there are for Ca (Figure 1.8, left panel). Comparison of the Ca and Ti condensation models in Figure 1.8 show that the magnitudes, and in some cases the signs, of isotopic fractionations between chemically similar elements can be non-intuitive.

1.5.3 Comparison of measurements to condensation models

A comparison of the coeval Ca and Ti isotope ratios to the condensation models is shown in Figure 1.9. The model curve for condensation in Figure 1.9 is based on an assumption that the degree of saturation for Ca and Ti should be similar given their broadly similar condensation temperatures (Figure 1.10) (i.e., S_{Ca}=S_{Ti}). The measured Ca and Ti isotopic fractionation effects in most of the CAIs of this study do not follow the S_{Ca}=S_{Ti} curve, suggesting a decoupling of the Ca and Ti systems in terms of saturation. Type B inclusions AL4884, Crucible, and forsterite-bearing SJ101 (Huang et al., 2012) exhibit fractionated Ca isotopes with correspondingly little Ti isotope fractionation and dramatically lie off the theoretical Ca-Ti-condensation curve (Figure 1.9).

The shallow (negative?) "trend" of the CAI data in Figure 1.9 implies that Ti experienced limited fractionation in comparison to expectations from the large heavy isotope depletions observed in Ca. One explanation is that the Ti and Ca are inherited from distinct reservoirs, as the pervasive and sometimes variable ^{50}Ti anomalies imply (Figure 1.7, Table 1.1). In this case, the CAIs can be regarded as processed (e.g., melted) aggregates of pre-existing materials as opposed to condensates from a well-mixed gas. This hypothesis is supported by the textural relationships seen in Type A CAI EK5-2-1R (Figure 1.1) that suggest localized partial resorbtion ±overgrowth of refractory minerals, possibly indicating that coarse-grained inclusions grow in part by the

consumption of earlier-formed refractory spinel-hibonite inclusions (SHIBs), a class of CAIs that often have large positive and negative ^{50}Ti anomalies (e.g., Ireland, 1988, 1990; Kööp et al., 2016c; Sahijpal et al., 2000). On the other hand, the measurements from a couple of the inclusions (major phases in EK5-2-1R and 461 B) do follow the theoretical fractionation model curve and thus can be explained by small (≤2 ºC) degrees of non-equilibrium condensation (i.e., undercooling).

Alternatively, the shallow slope defined by the data in Figure 1.9 may indicate condensation from a well-mixed gas, but where Ca and Ti condensed in response to different degrees of undercooling (i.e., $S_{Ca} \neq S_{Ti}$). This is possible because in detail Ti has a higher T_{eq} than Ca by ~50 ºC at their respective 50% condensation temperatures (at nebular pressures of 10^{-5} bar, Figure 1.10 (Ebel and Grossman, 2000). In this case, a difference in undercooling of ~2 degrees is all that is required to produce these decoupled signatures (Figures 1.8 and 1.11). The implication would be that the cooling rate during Ti condensation was slower than that when Ca condensed.

It can also be shown that the evidently uncorrelated Ca and Ti isotope records could be explained by a single condensation process, if the isotopic records reflect condensation of a localized 'droplet' and/or extremely fractionated nebular reservoir. This can be seen in Figure 1.11 that shows the effects of instantaneous condensation where:

$$\delta = (\delta_0 + 1000\,)(\alpha_{cond} F^{\alpha_{cond}}) \qquad (5).$$

We believe that models computed for instantaneous, rather than bulk condensation, are more representative of the processes dictating isotope fractionation recorded by the earliest formed condensates in the solar nebula. In general, all of the coarse-grained CAIs can be modeled by similar degrees of undercooling (e.g., ~1-2 degrees) by instantaneous condensation. Likewise, the relatively extreme values measured in fine-grained CAI 3B3 can be explained by the endmember case of this scenario. The curves in Figure 1.11 show that near-equilibrium condensation at more

than ~95% depletion of the gas reservoir in both Ca and Ti can explain the isotope ratios in both systems. If the model is taken at face value, i.e., the gaseous reservoir from which 3B3 condensed is the nebula and not an isolated portion of nebular gas, then fine-grained inclusions like 3B3 would have formed extremely late after >95% of the Ca in the nebula had condensed. At thermodynamic equilibrium the temperature interval over which this would have occurred was ~1525 to 1450 K (e.g., Ebel and Grossman, 2000). It is noteworthy that only about 5% or less of the Mg in the gas would have condensed through this temperature interval. Even if it condensed from a localized gas reservoir, this suggests that 3B3, a fine-grained CAI, actually represents a late or relatively late nebular condensation event and not condensation of a primordial solid. Future comparisons between additional measurements (i.e., Jordan et al., 2014; in prep.) and these self-consistent theoretical models for Mg, Si, Ca, and Ti isotope ratios will allows us to more fully understand the effects of condensation and the formation history of these objects.

1.5.5 Anomalous ^{50}Ti effects track reservoir mixing in the early Solar System

The existence and size of isotopic anomalies (e.g., Niederer and Papanastassiou, 1984) are typically thought to reflect a significant state of isotopic heterogeneity in the earliest Solar System, perhaps left over from molecular cloud heterogeneities on the grain scale (Young, 2016) or late stellar injection (e.g., Dauphas et al., 2010). The relative dilution of these isotopic anomalies has been used to track how less primitive solids and bulk planetary precursor materials were admixed and homogenized in the protoplanetary disk (Dauphas et al., 2014; Liu et al., 2009; Moynier et al., 2010; Simon et al., 2009; Trinquier et al., 2008).

A number of recent studies report ^{50}Ti isotope anomalies in early formed solids (e.g., Leya et al., 2009; Kööp et al., 2016a; Kööp et al., 2016b; Williams et al., 2016). The ^{50}Ti effects

measured in spinel-hibonite inclusions (i.e., SHIBs), platy hibonite crystals (PLACs), and related hibonite-rich inclusions are extreme, ranging from large excesses to large depletions relative to the ~1‰ level (i.e., 10 ε-units) effects typically reported for common Types A and B inclusions (e.g., Williams et al., 2016 and references therein), Figure 1.6. Positive ε^{50}Ti generally correlates with smaller Ni, Cr, and Zr isotopic anomalies as well as smaller Ca isotope anomalies. FUN inclusions are the exceptions as they usually exhibit strongly negative ε^{50}Ti values (Niederer et al., 1985; Papanastassiou and Brigham, 1989; Loss et al., 1994; Williams et al., 2012; 2016).

Given the consistency between measured and modeled Ca and Ti isotope effects, a relatively simple non-equilibrium condensation scenario could explain 461 B. It likely condensed by ~1-2 degrees of undercooling from a rather primitive gas reservoir with ε^{50}Ti excess. Its refractory isotopic signatures indicate that it did not later equilibrate in a planetary-like reservoir. In light of the textural and petrologic evidence that EK5-2-1R contains "exotic" refractory phases, it is interesting that the Ti laser spot analyses of EK5-2-1R that contain the greatest proportion of spinel-hibonite "mélange" on average exhibit the most "normal" ε^{50}Ti value and normal mass dependent δ^{49}Ti/^{47}Ti, whereas on average the spot analyses of EK5-2-1R dominated by major minerals exhibit a slightly higher ε^{50}Ti value and more negative δ^{49}Ti/^{47}Ti value, sharing a trend with 461 B (Figure 1.9). The "relict" refractory minerals could actually have positive δ^{49}Ti/^{47}Ti values, like 3B3, or possibly even higher, if one considers the fact that the range of spot analyses (see Figures 1.4 and 1.6) all contain variable amounts of their coarse-grained host that exhibits negative δ^{49}Ti/^{47}Ti. Nevertheless, they have mass dependent Ti isotope effects that appear decoupled from the Ca isotopic composition, whereas it appears that the melt that partially enveloped them recorded a signature of non-equilibrium condensation, as would be theoretically predicted by its corresponding Ca isotopic composition. In order for the apparent mass-dependent

Ti isotopic heterogeneity of the CAI to have persisted, its history must either reflect: (1) condensation on the precursor mélange of refractory phases that was later partial remelted, and evolved as an open system isotopically, or (2) that the mélange of refractory precursors was enveloped/partially consumed by a protoCAI droplet of remelted condensates. In either scenario, a second reservoir is required to impart the ε^{50}Ti excess observed in the host phase.

It is commonly assumed that the carriers of the neutron-rich anomalous isotope effects were added significantly before the now extinct ^{26}Al ($t_{1/2}$=0.7 Ma) was added to the protosolar disk (Sahijpal and Goswami, 1998). An alternative explanation is that the concentrations of the neutron-rich isotopes and the ^{26}Al in the early Solar System are averages inherited from the cloud material from which the Sun formed. In the latter scenario, canonical $^{26}Al/^{27}Al_0$ represents the homogenization of grains with much lower and much higher $^{26}Al/^{27}Al_0$ values that are averaged by processing in the solar protoplanetary disk (Young, 2016). EK-5-1R may represent a relatively primordial snapshot of this homogenization process in progress.

1.5.6 Implications of intra-CAI calcium isotopic zoning

The *in-situ* evidence for Ca isotopic zoning across the interior of AL4884 reported here is a novel discovery and only measurable because of the combined developments in our micromilling and mass spectrometry techniques. Systematic stable isotope measurements across CAI margins have been performed for various elements on an individual element basis, but multiple complementary isotope profiles, such as for Ca together with Mg, have rarely been made for the same object (cf. Bullock et al., 2013; Knight et al., 2009; Shahar and Young, 2007). A previous hint of intra-CAI mass-dependent Ca isotopic heterogeneity exists in the early work of Niederer and Papanastassiou (1984) who reported resolvable effects among Al-Ti-pyroxene separates from

a single inclusion. The intra-CAI Ca isotopic zoning in AL4884 confirms that a refractory element can be isotopically fractionated at the scale of an inclusion. The systematic zoning profile (Figure 1.7) implies that AL4884 condensed with isotopically light Ca compared to planetary materials and experienced later evaporation and/ or a changing environment that significantly affected the Ca isotopic composition of its melilite mantle. The zoning could be due to a compositional change of the surrounding gas or could be related to changing conditions (e.g., less undercooling) that govern formation of the melilite mantle. It is unclear why zoning was not also observed in Crucible, or for that matter, how pervasive intra-CAI Ca isotopic zoning is among different CAIs. Yet, the more refractory nature of Ca and relative superposition of core and edge, respectively, suggest that the events that led to Ca isotopic zoning in AL4884 occurred prior to the history inferred by the isotopic signatures recorded by moderately volatile elements Mg and Si in CAIs and their Wark-Lovering rims (e.g., Simon et al., 2005).

Theoretical and experimental studies imply that evaporative residues must have been heated at low pressures for appreciable mass-dependent isotopic fractionation to be preserved (Davis et al., 1990; Nagahara and Ozawa, 2000; Yamada et al., 2006; Zhang et al., 2014). As such, the *relatively* heavy Ca isotope enrichment measured in the melilite margin of AL4884 and the heavy Mg isotope enrichments of many CAIs imply that they experienced evaporation at low pressures ($<10^{-4}$ bar), conditions that are thought to be typical near the proto-Sun. It is noteworthy that little to no Mg could remain in the condensed phase at conditions hot enough to enrich heavy Ca by evaporation (Simon and DePaolo, 2010). Moreover, the normal Mg isotopic compositions reported in the margins and WL rims for several CAIs (Bullock et al., 2013; Simon et al., 2005) and for chondrules (Alexander et al., 2008; Galy et al., 2000) indicate that these materials formed

from high local partial pressures and/or dust-rich regions of the solar nebula distinct from the hot inner solar nebula.

The recent comparison of isotopic data for CAIs (Niederer and Papanastassiou, 1984) and numerical models of Simon and DePaolo (2010) quantified the discrepancy between Ca and Mg isotope effects. The difference is likely due to their significantly different volatilities. As such, the measured Ca isotopic zoning profile of AL4884 indicate that analogous Mg isotopic zoning profiles likely reflect a later process(es), i.e., Simon and Young (2011). In fact, the sense of Ca isotopic zoning in AL4884 reported in this study is opposite that of its Mg isotopic zoning profile that decreases from "heavy" in the interior to relatively "normal" planetary values at the edge (Bullock et al., 2013). Later coeval condensation from a reservoir with distinct planetary-like Ca and Mg, related to formation of the melilite mantle of AL4884, could potentially explain the apparently converging profiles. But in such a scenario an additional solid-state diffusive exchange event that produces the isotopic zoning, of the type reported by Simon et al. (2005); Young et al. (2005), would also be required. Additionally, not all CAIs exhibit normal Mg isotope compositions at the edge, e.g., Simon and Young (2011) and the only other inclusion for which comparable *in-situ* Ca isotopic measurements are available, i.e., Crucible, appears homogenous (this study). It follows that the sense of Ca zoning in AL4884 that is inconsistent with most reported Mg isotopic zoning profiles in CAIs that decrease from "heavy" in the interior to "normal" values at the edge implies that Mg isotopic signatures in CAIs in general may be susceptible to later modification in the solid-state, cf. MacPherson et al. (2012). Evidence for apparently conflicting Ca and Mg isotopic zoning profiles therefore opens up the possibility that similar Mg isotopic records measured in a number of other CAIs could also be related to a late isotopic exchange event. Although more corroborating evidence is required to confirm the interpretation for later isotopic

exchange, the new Ca data are difficult to reconcile with conventional interpretations for the canonical Al-Mg initial value of AL4884.

1.6. Conclusions

Here we report coordinated measurements of Ca and Ti isotopes in refractory inclusions. When compared to our latest condensation model calculations for isotopic fractionation it is clear that most, if not all, of the studied "normal" CAIs, and/or their precursor materials, record a multi-step/source condensation history. The extreme Ca and Ti isotope effects measured in the fine-grained CAI 3B3 exemplify the complicated condensation history of early formed solids. Such textures, that are often assumed to signify the primitive nature of nebular materials, may in fact reflect condensation from relatively evolved (i.e., fractionated) nebular gas rather than representing primordial condensates. The discovery of Ca isotopic zoning in Type B CAI AL4884 likely involves condensation from an evolving gaseous reservoir, presumably after ^{26}Al was added to the Solar System, but before its moderately volatile element isotopic signatures were preserved. Thus, the existence of Ca isotopic zoning in AL4884 implies that its Mg isotope record pertains to a later, likely subsolidus, nebular history.

Acknowledgements

The Department of Mineral Sciences, Smithsonian Institution is acknowledged for providing mineral standards. NASA Curation and CAPTEM are thanked for allocation of the lunar basalts used to evaluate the magnitude of stable Ca isotope effects among terrestrial bodies. Detailed and helpful comments of reviewers C. Williams and D. Papanasasstiou and Editor F. Moynier are greatly appreciated. K. Ross, E. Berger, and K. McCain are thanked for technical

assistance related to sample characterization by SEM. R. Mills and B. Ware are thanked for preparing a number of the reference materials for isotopic analysis, including the lunar basalts. NASA grants 11-COS11-0066 and 16-EW16_2-0163 to J.I.S. and grant 14-EW14_2-0060 to E.D.Y., and NSF grant EAR1530306 to E.A.S. supported this work.

461

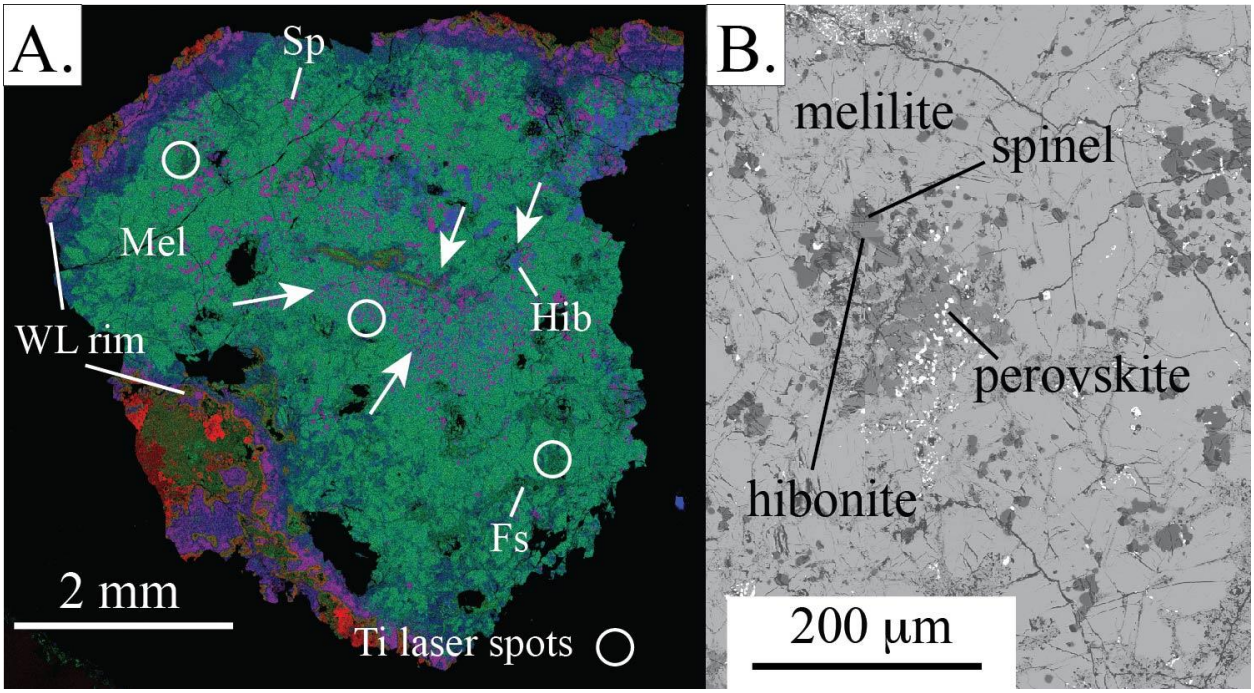

Figure 1.1. (A) False color (RGB=Mg-Ca-Al) X-ray scanning electron microscope image of nearly intact coarse-grain Type A inclusion EK5-2-1R. Primary melilite (Mel), fassiate (Fs), Spinel (Sp)± hibonite (Hib) are shown. Secondary sodalite and nepheline located at the outer margin of the melilite interior. Wark-Lovering (WL) rim surrounds interior. Some olivine-rich host material outside of rim seen. Arrows indicate "mélange" of accessory hibonite, perovskite, and spinel grains concentrated towards the inclusion core. (B) Back-scattered electron (BSE) image showing representative refractory mineral mélange within melilite interior.

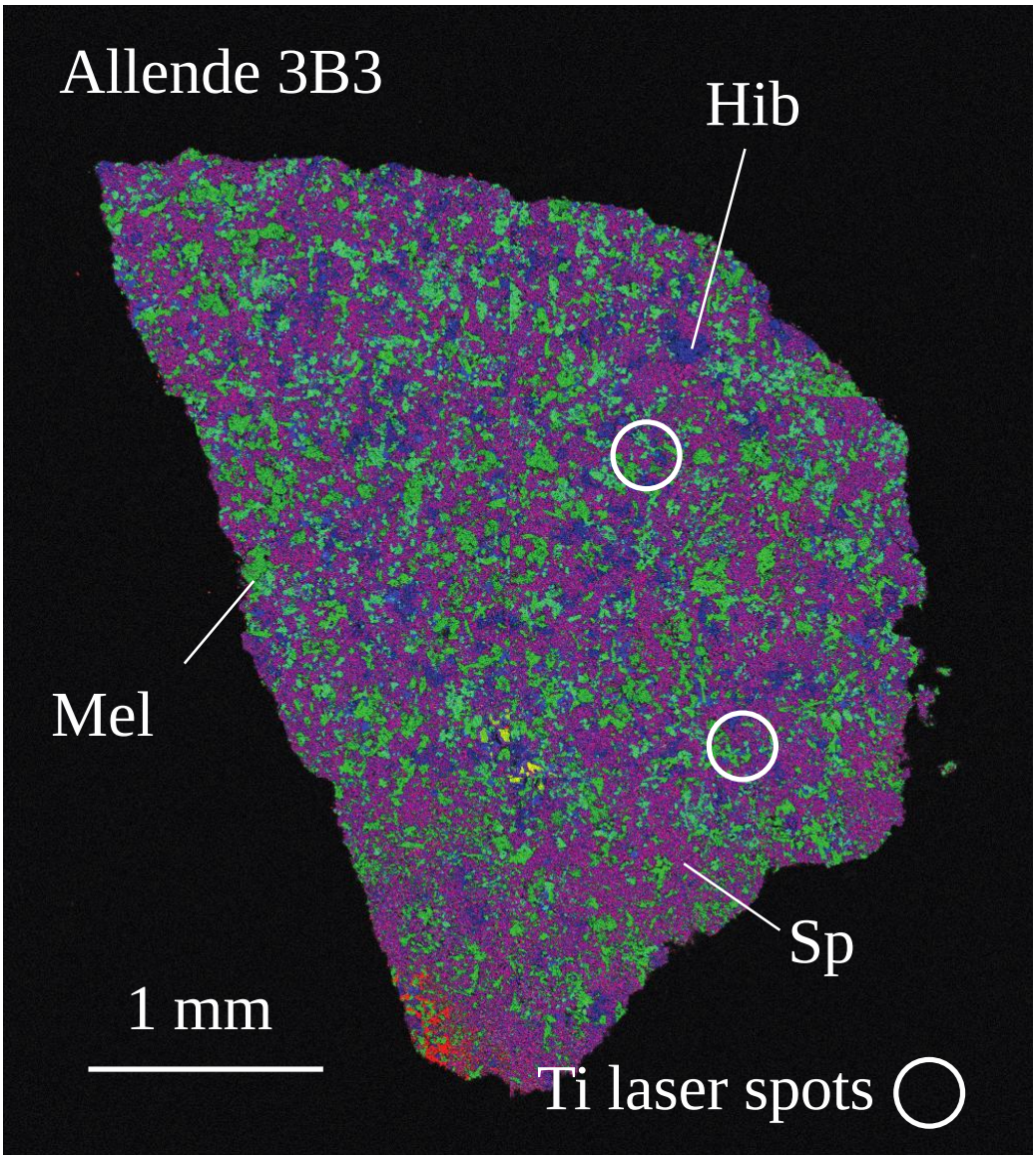

Figure 1.2. False color (RGB=Mg-Ca-Al) X-ray scanning electron microscope image of fragment of fine-grain alkali-rich Allende inclusion 3B3. Spinel (Sp, purple), hibonite (Hib, blue), melilite (Mel, green) dominate mineral assemblage. Red material at bottom indicative of olivine-rich host material. The image is of a fragment of a large inclusion (~10x10 mm).

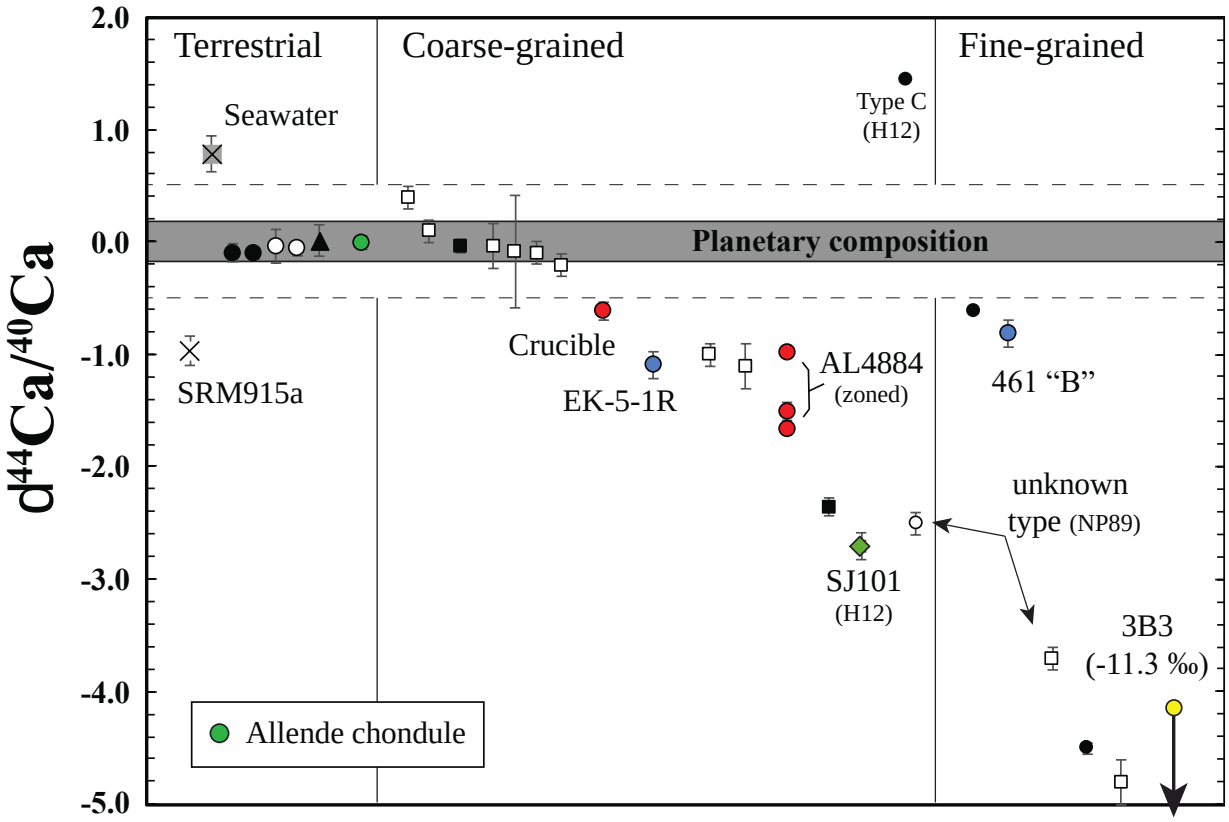

Figure 1.3. Plot shows double spike TIMS measurements of mass dependent calcium isotope compositions of CAIs and other planetary materials. Reported uncertainties are 2 SE and often less than the symbol size. Standard reference materials show 2 SD external reproducibility. Open symbol CAI data come from Niederer and Papanastassuiou, 1984 (NP84). Black CAI and SJ101 (green diamond) data come from Huang et al., 2012 (H12). Measured terrestrial minerals, lunar basalts, and chondrule (this study) lie within the range of planetary materials reported by Simon and DePaolo (2010). For reference, FUN inclusions range from -27 to +15‰ and the range (±0.5‰) delineated by the horizontal dashed lines reflects the stated confidence interval of individual measurements in NP84.

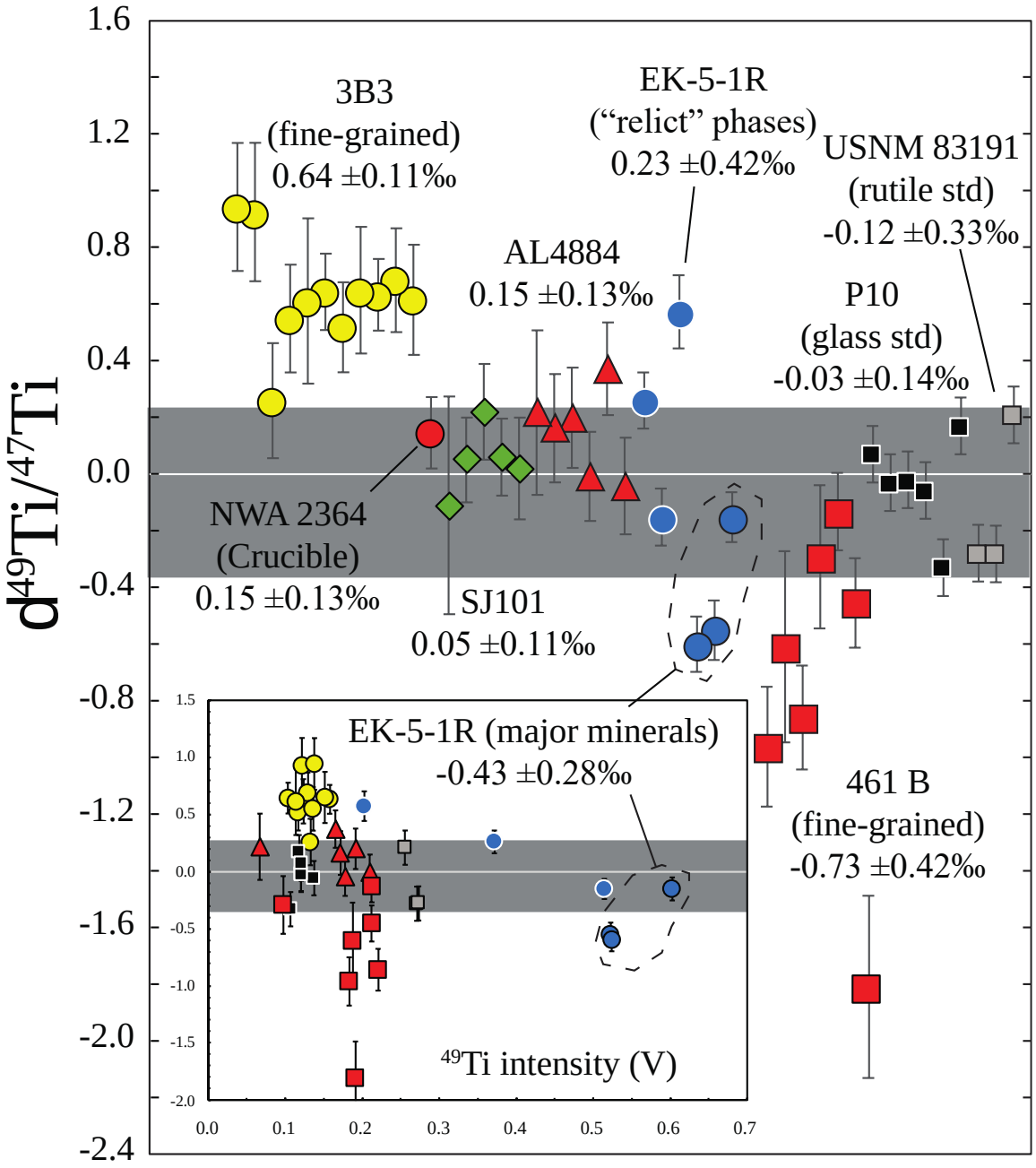

Figure 1.4. Plot of laser ablation MC-ICPMS spot analyses of mass dependent titanium isotope compositions for studied refractory inclusions. Symbols as in Fig. 3. IntraCAI heterogeneity in fine-grained CAIs (3B3 and 461 "B") and in EK-5-1R (relict phases are heavy and major minerals light) exist. Inset shows that isotope effects are independent of measured ^{49}Ti intensity. Uncertainty of individual measurements are 2 SE internal precision. Standard materials shown for comparison.

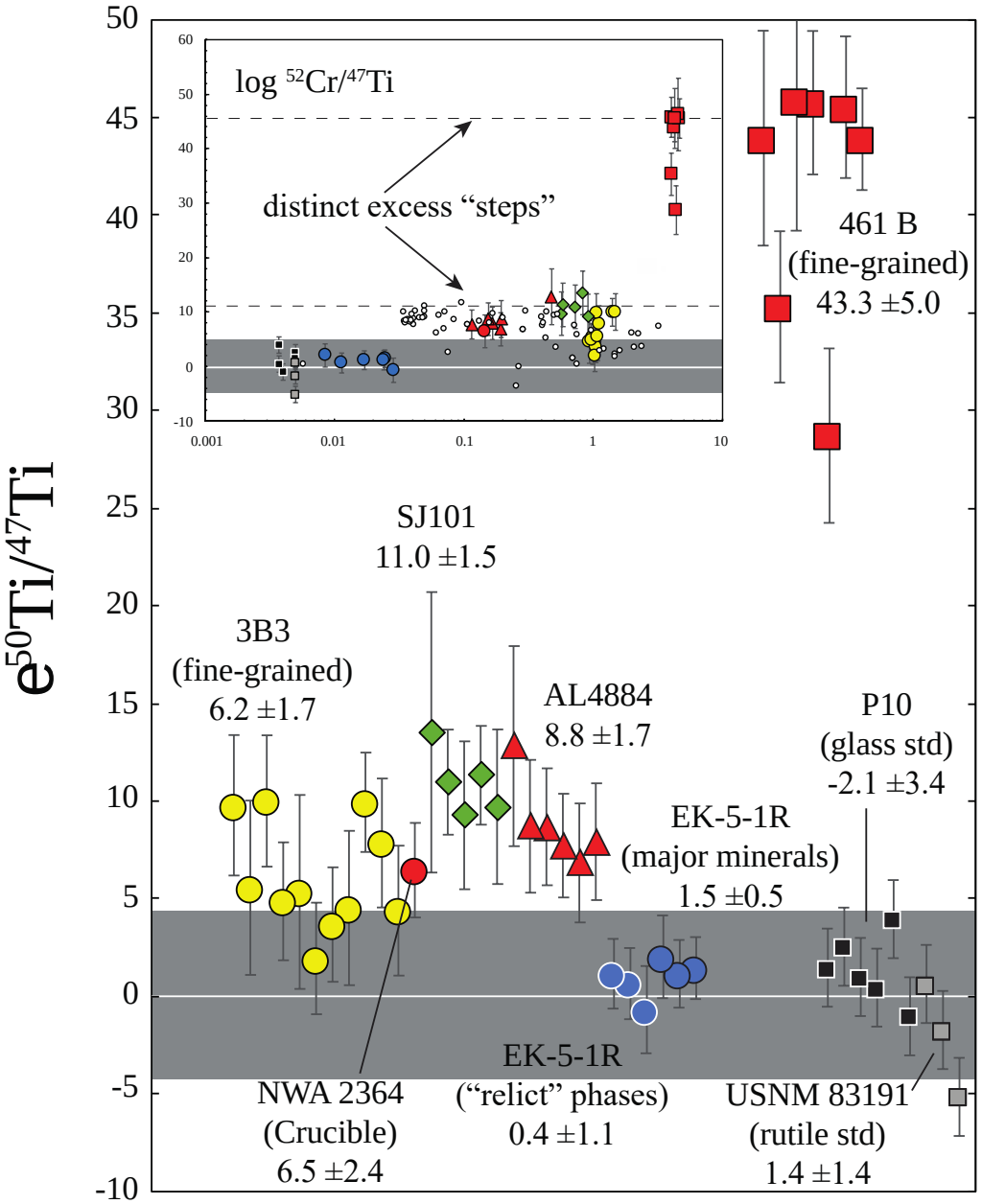

Figure 1.5. Plot of laser ablation MC-ICPMS spot analyses of $\varepsilon^{50}Ti/^{47}Ti$ titanium isotopic anomalies in studied refractory inclusions. Symbols as in Fig. 3. Inset shows that measured ^{50}Ti isotope anomalies define clear plateaus that are not easily related to Cr abundance (i.e., Cr/Ti ratio). Data report by Jordan et al. (2017) shown as small circles. Uncertainty of individual measurements are 2 SE internal precision. Standard materials shown for comparison.

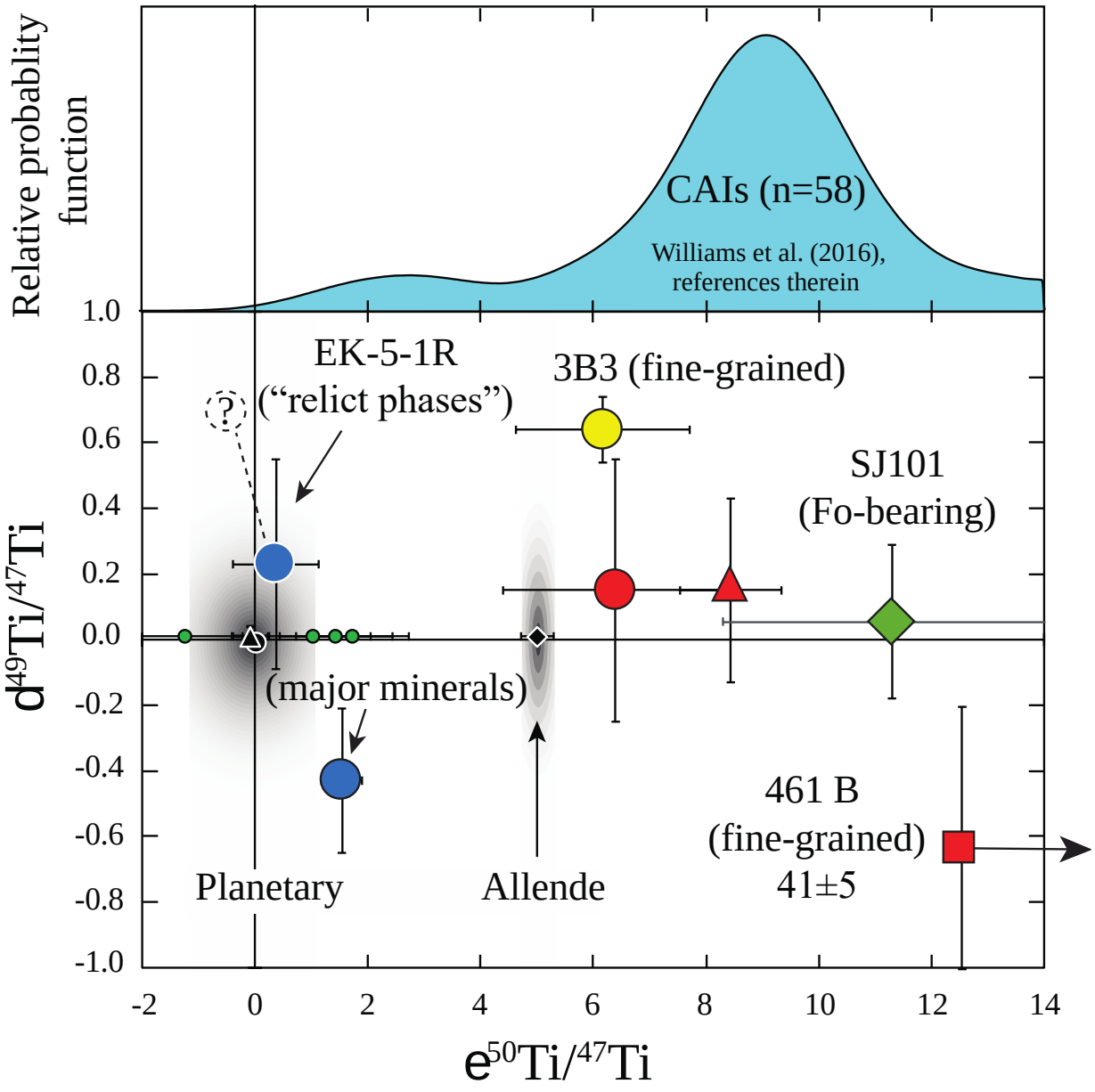

Figure 1.6. Plot of laser ablation MC-ICPMS measurements of mass fractionated titanium $\delta^{49}Ti/^{47}Ti$ compositions and $\varepsilon^{50}Ti/^{47}Ti$ titanium isotopic anomalies in the studied refractory inclusions. Uncertainty are 2 SE. Symbols for CAIs as in Fig. 3. Allende whole rock = black diamond, lunar basalt = black triangle, terrestrial basalt = black circle, Allende chondrules = green circles shown. Mass dependent isotope compositions of lunar and terrestrial rocks determined by double spike solution MC-ICPMS analysis (Millet et al., 2016). $\varepsilon^{50}Ti/^{47}Ti$ values for rocks and bulk Allende by MC-ICPMS from Connelly et al. (2007); Trinquier et al. (2007, 2009). The distribution of $\varepsilon^{50}Ti/^{47}Ti$ values for common Types A and B inclusions (top) reported by Niederer et al. (1980, 1981, 1985), Trinquier et al. (2009), Leya et al. (2009), Chen et al., (2009), Williams et al. (2016), and this study is shown.

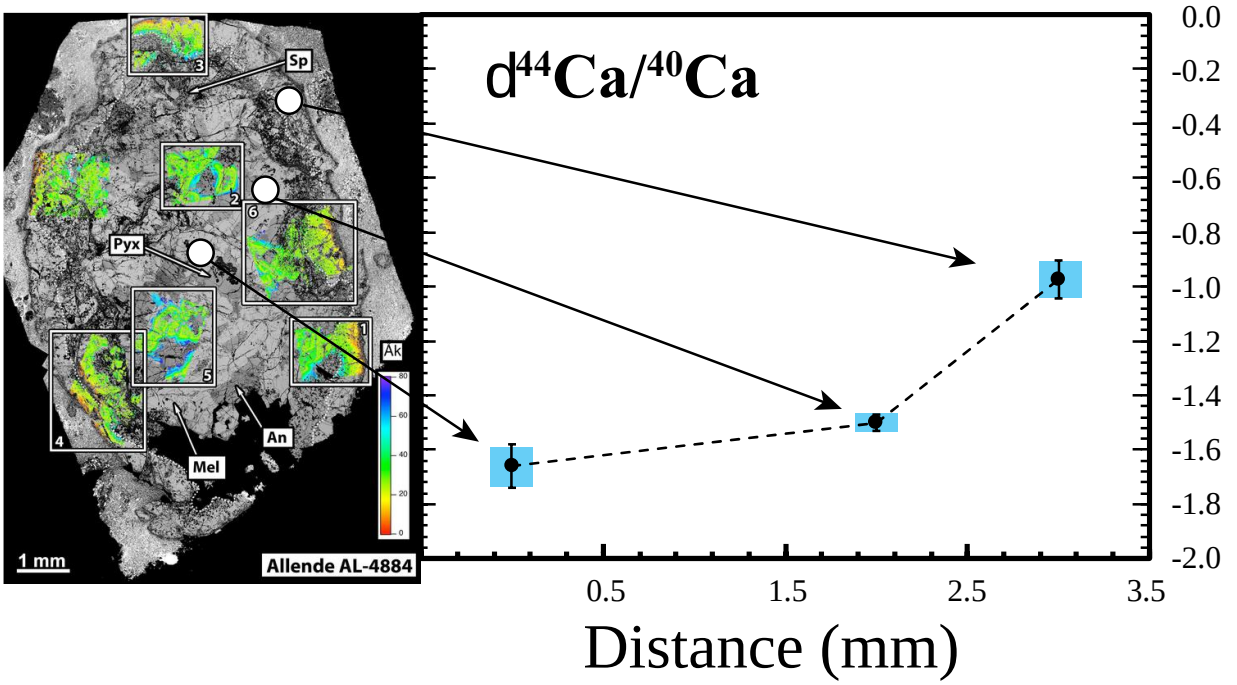

Figure 1.7. Calcium isotopic zoning across Type B CAI AL-4884. Analytical measurements across the entire inclusion exhibit negative $\delta^{44}Ca/^{40}Ca$ values, but these values get higher, i.e., heavier towards the edge of the inclusion. Data are shown relative to the planetary composition (e.g., bulk silicate Earth ~0‰). Image at left shows micromilling subsample locations and compositional zoning in melilite from Bullock et al. (2013).

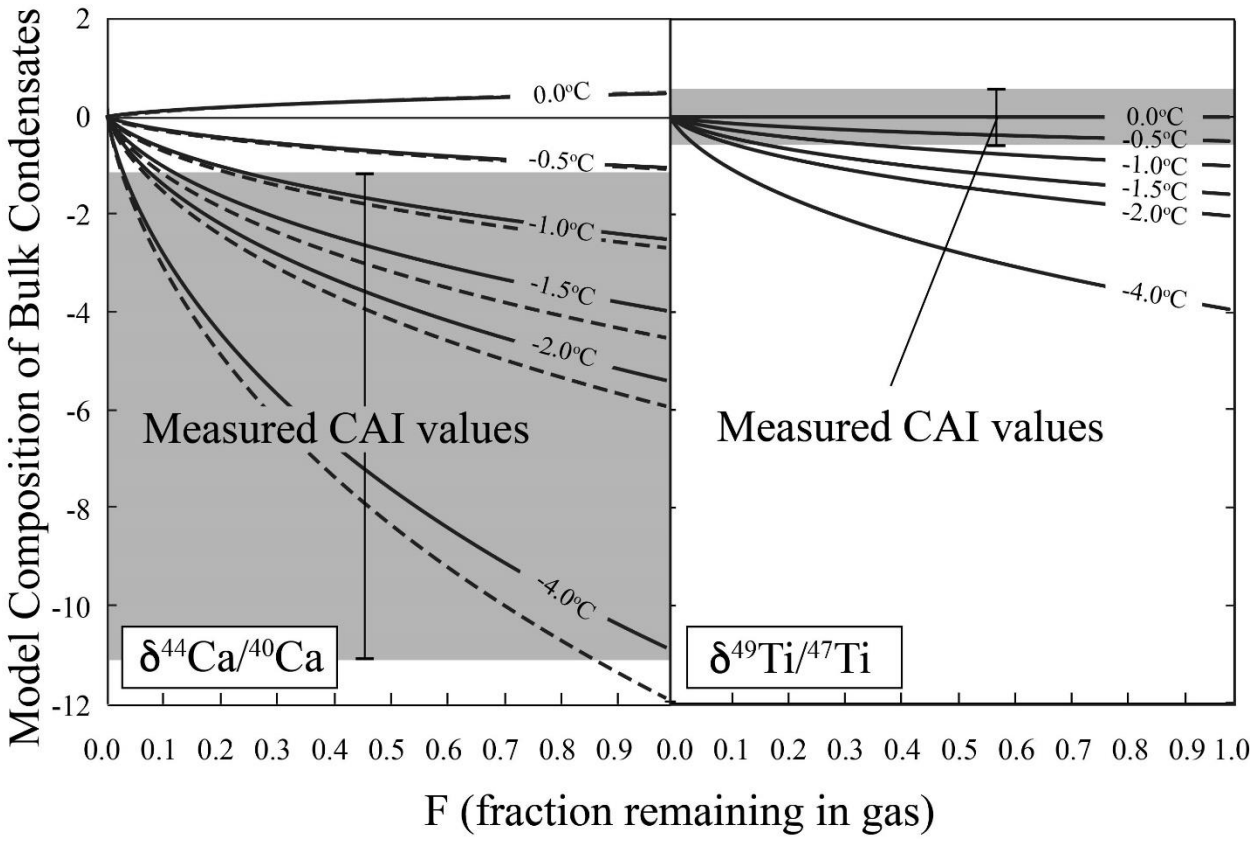

Figure 1.8. Modeled isotopic evolution of bulk condensate compositions during Raleigh distillation of nebular gas at 1600 K. Dashed Ca model curves represent condensation at 1525 K (see text). Ca and Ti isotopic signatures are typically depleted in heavy isotopes during non equilibrium condensation (undercooling). Small Ca isotopic enrichments can be achieved by equilibrium condensation (left).

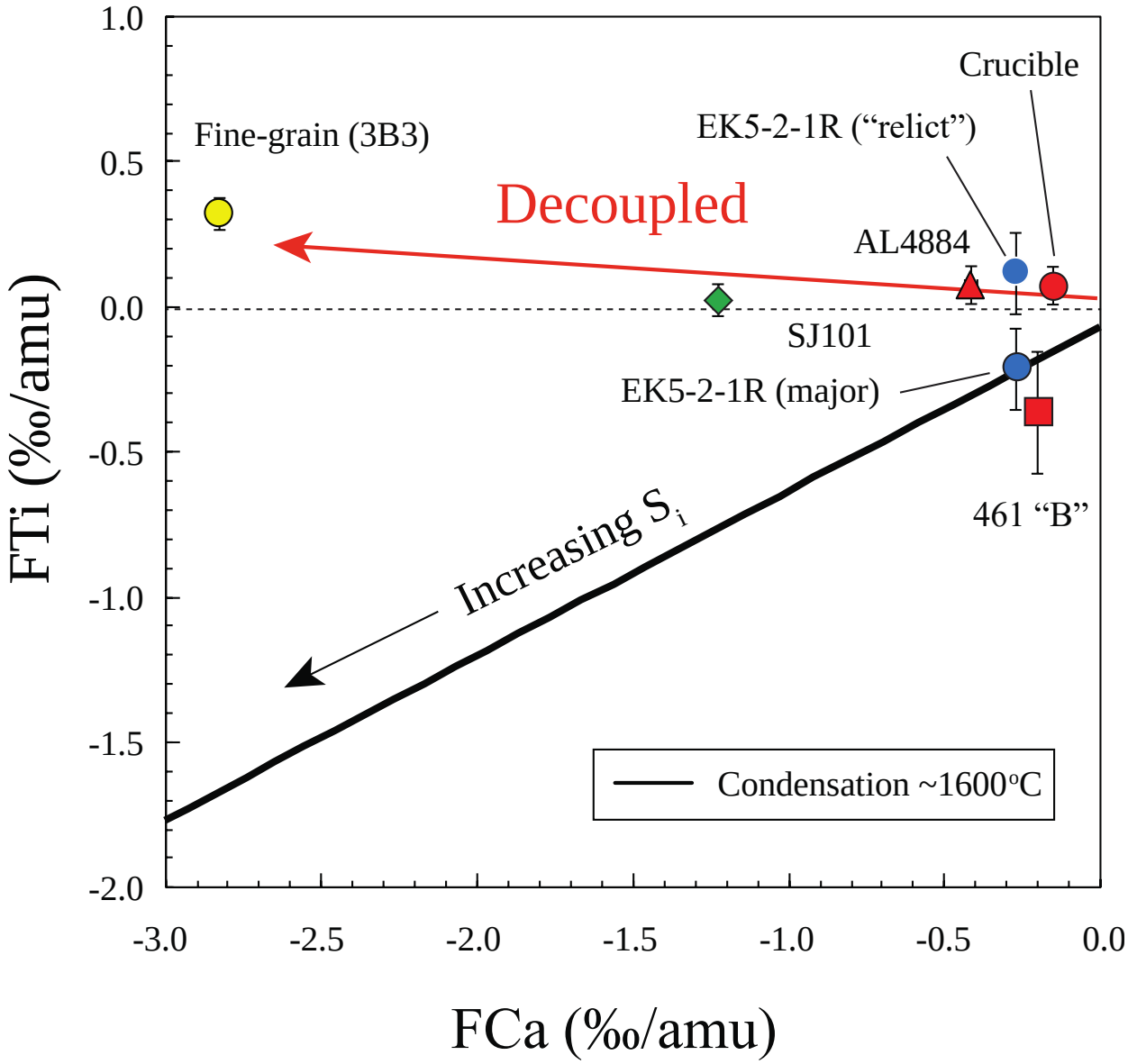

Figure 1.9. Ca and Ti isotope data for studied inclusions plotted with mass fractionation condensation modeling shown as a function of oversaturation (S_i) (thick solid line). All data and model results converted to a common scale for direct comparison. A general trend among Type B CAIs AL4884 (core), Crucible, SJ101, and fine-grained 3B3 (red line), can be seen but lies off the theoretical curve. CAIs EK5-2-1R (major minerals) and 461 "B" are consistent with theoretical fractionation.

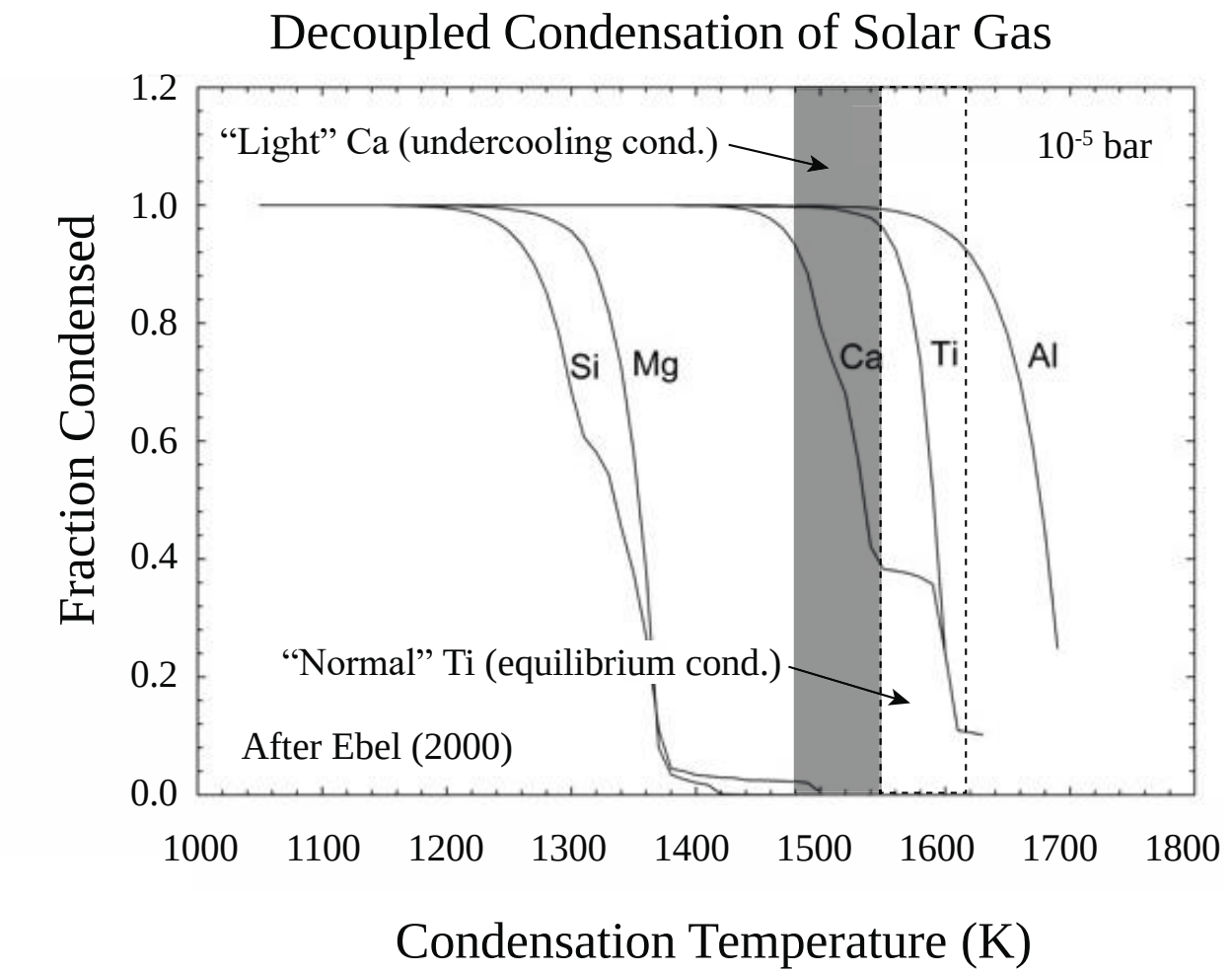

Figure 1.10. Predicted enrichments of major rock forming elements as a function of condensation temperature (thermodynamic condensation model curves from D. Ebel). Possible decoupled history of Ca and Ti condensation of Solar gas shown that can explain the normal Ti and "light" Ca isotope effects measured in the studied refractory inclusions (see text).

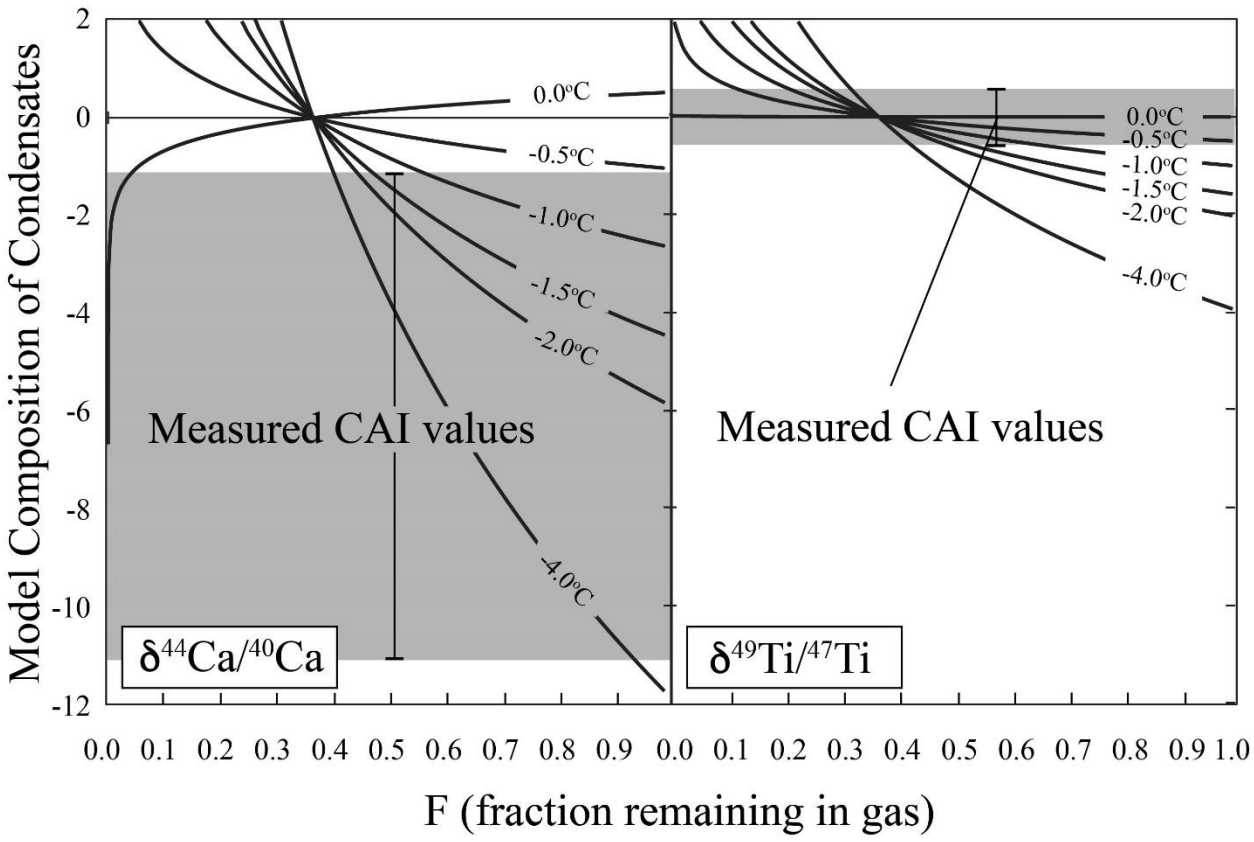

Figure 1.11. Evolution of instantaneous isotopic composition of Ca and Ti during Rayleigh distillation. Ca and Ti isotopic signatures are typically enriched in heavy isotopes during non equilibrium condensation (undercooling) until about F=0.35 and then become enriched in the light isotopes. At equilibrium significant heavy Ca isotopic depletions can be produced after significant fractionation (F<0.1) (left).

Table 1.1. Summary of Ca and Ti isotope data.

Sample	Description	Sample wt. (mg) [wt]	$\delta^{44}Ca/^{40}Ca$ (seawater scale)	$\delta^{44}Ca/^{40}Ca$ (chondritic scale)	$\delta^{44}Ca/^{40}Ca$ (SRM915a scale)	2 SD	2 SE*	$\delta^{49}Ti/^{47}Ti$ (laser)	2 SE	$\varepsilon^{(50}Ti/^{47}Ti)$ (laser)	2 SE	Spots (laser)	$\varepsilon^{(49}Ti/^{47}Ti)$ ($TIMS^{HN}$)	2 SE
461 3B3	fine-grained Type A	1.19	-12.11	-11.31	-10.34		0.03	0.64	0.11	6.2	1.7	n=10	13.2	1.2
EK5-2-1R	coarse-grained Type A	28.34	-1.89	-1.09	-0.12		0.12	-0.10	0.37	1.0	0.8	n=6	0.0	1.0
	fassiate							-0.43	0.28	1.5	0.5	n=3		
	hibonite/pervoskite/spinel							0.23	0.42	0.4	1.1	n=3		
461, 13, 2 slab_B	fine-grained Type A, hibonite-rich mantle	0.23	-1.61	-0.81	0.16		0.03	-0.73	0.42	41.6	5.2	n=7		
NWA 2364 "Crucible"	avg. reworked coarse-grained Type B	1.15	-1.41	-0.61	0.36	0.16	0.08	0.15	0.13	6.5	2.4	n=1		
	core	0.56	-1.37	-0.57	0.40		0.02							
	margin	0.41	-1.46	-0.66	0.31		0.14							
AL 4884	coarse-grained Type B1, core	0.58	-2.46	-1.66	-0.69		0.08	0.15	0.13	8.8	1.7	n=6		
	coarse-grained Type B1, outer core	0.19	-2.30	-1.50	-0.53		0.03							
	coarse-grained Type B1, mel mantle	0.27	-1.77	-0.97	0.00		0.07							
SJ101[H&J]	Fo-bearing	?	-3.50	-2.70	-1.73		0.05	0.05	0.11	11.0	1.5	n=5		
Other data														
461, 13, 2 slab_D	complex chondrule	0.4	-0.80	0.00	0.97		0.06							
BCR-2	basalt		-0.90	-0.10	0.87	0.08	0.06							0.09
BCR-1[S&D]	basalt		-0.89	-0.09	0.88	0.05	0.03							
Allende	carbonaceous chondrite, bulk		-1.22	-0.42	0.55		0.11							0.29
103140 (terrestrial)	akermanite mineral separate		-0.86	-0.06	0.91		0.15							
164905 (terrestrial)	augite mineral separate		-0.83	-0.03	0.94		0.06							
lunar (7 samples)	basalt, high and low Ti		-0.78	0.02	0.99	0.14	0.03							0.32
SRM915a (n=9**)	carbonate		-1.76	-0.96	0.01	0.13	0.04							
SRM915b (n=10)	carbonate		-0.96	-0.16	0.81	0.18	0.06							
Seawater (n=3)	IAPSO standard		-0.01	0.79	1.76		0.16							
USNM 83191	rutile							-0.12	0.33	-2.1	3.4	n=3		
P10	synthetic glass							-0.30	0.14	1.4	1.4	n=6		

[H&J]Ca isotope data for CAI SJ101 from Huang et al. (2012), Harvard.

[S&D]Ca isotope data for BCR-1 from Simon and DePaolo (2010), UC Berkeley .

[H&N]Ti isotope data for 3B3 and EK5-2-1 from Harper and Nyquist (1990), NASA JSC .

*All unknowns and terrestrial materials replicated.

**SRM915a internal standard run in 2015, 3 analyses during instrument use for this study.

[wt]Sample weights for 42-48 Ca isotope TIMS analyses; rock and mineral standard and reference materials were approximately 25 mg.

Appendix A: Contribution to Simon et al. (2017)

My contributions to the Simon et al. (2017) paper were significant and apply to several different aspects of the study. These contributions included procedural development, sample preparation, sample processing, data collection, data processing, and data interpretation.

Calcium Analyses. Calcium isotope data were collected at the Center for Isotope Cosmochemistry & Geochronology (CICG) at NASA Johnson Space Center (JSC). I prepared the Al4884 and NWA 2364 Crucible CAIs for analysis. This included microdrilling the CAIs to collect material for analysis, dissolution of the material in a HF-HNO_3 mixture aided by use of a Parr Bomb, and purifying the Ca by use of ion exchange chromatography. The ion exchange chromatography procedure is detailed in Simon and DePaolo (2010), with improvements outlined in Tappa et al. (2014). These tasks were performed under the supervision of Michael J. Tappa and Dr. Justin I. Simon.

Ti by solution. Titantium isotopes were measured by solution for several of the CAIs presented in Simon et al. (2017). These analyses were conducted at CICG at NASA JSC. Though I was not responsible for the analyses, I helped to set up the ion exchange chromatography procedure in the lab at JSC under the supervision of Michael J. Tappa and Dr. Justin I. Simon. This included multiple rounds of testing to determine if the columns were successfully isolating Ti. Adjustments were made accordingly and further tests carried out until the procedure successfully isolated Ti, with all matrix elements below detection limits. Tests included producing elution curves for the column procedure to determine where each element was stripped off the resin. These tests were performed using the standard, BCR-2. During the column procedure, each 2 mL of acid that was loaded onto the column (after sample loading) was collected in a separate beaker. Each beaker was left on a hot plate until all acid evaporated. The

solid material was then re-dissolved in 2% HNO_3 for analysis on a Thermo Fisher Element-XR magnetic sector inductively-coupled plasma source mass spectrometer (ICP-MS). Analyses on the ICP-MS were performed with the help of Dr. Zhan X. Peng. Using the ICP-MS we were able to measure the concentration of a suite of elements in each 2 mL segment of the column procedure. This allowed me to determine when Ti was being eluted from the column and whether or not the segments containing the Ti were isolated or contained problematic amounts of additional elements. Tests were repeated until we determined exactly what volumes of acid to collect to purify Ti. The procedure was adapted from Zhang et al. (2011).

Ti analyses by laser ablation. All contributions discussed in this section were performed in the Young Laboratory at University of California, Los Angeles. With the aid of Dr. Issaku E. Kohl, I prepared mounts for several of the CAIs analyzed in this study. Thick sections of the samples were cut from larger pieces of chondrite using a diamond blade saw. Samples were then mounted in epoxy within plastic rings that can be loaded in the sample chamber for the laser system. Mounts were polished using a series of diamond slurries of sequentially smaller grit size, with the smallest size being ¼ micron, to ensure a flat sample surface for analysis. Additionally, samples were repolished using ¼ micron grit diamond slurry after each day of data collection to remove any material on the surface that may have resulted from ablation.

With the exception of SJ101, Al4884, and Crucible, I was the lead scientist responsible for the Ti isotope data collection by laser ablation. Kaitlyn A. McCain, Dr. Issaku E. Kohl, and Prof. Edward. D. Young were also involved with data collection. Data collection involved multiple tests to ensure the robustness of the method as well as the collection of measurements for the unknowns.

In addition to collection, I was responsible for reducing the titanium isotope data. This includes application of the peak stripping procedure, calculation of the ^{50}Ti anomalies, and calculation of the analytical errors for the anomalous ^{50}Ti measurements. Details can be found in Simon et al. (2017) and Chapter 2 of this dissertation.

Finally, I was involved in data analysis, predominately with regard to the titanium data. I presented our findings and interpretation of the data at the 48th Lunar and Planetary Science Conference in Houston, TX.

Appendix References

Simon, J.I. and DePaolo, D.J., 2010. Stable calcium isotopic composition of meteorites and rocky planets. Earth and Planetary Sciences Letters **289**, 457-466.

Simon, J.I., Jordan, M.K., Tappa, M.J., Schauble, E.A., Kohl, I.E., and Young, E.D. 2017. Calcium and titanium isotope fractionation in refractory inclusions: Tracers of condensation and inheritance in the early solar protoplanetary disk. EPSL **472**, 277-288.

Tappa, M.J., Mills, R.D., Ware, B., and Simon J.I. A procedure to determine the coordinated chromium and calcium isotopic composition of astromaterials including the Chelyabinsk meteorite. LPS XLV, Abstract #1908

Tappa, M.J., Simon, J.I., Jordan, M.K., and Young, E.D. A procedure to simultaneously determine the calcium, chromium, and titanium isotopic compositions of astromaterials. LPS XLVI, Abstract #2083

Zhang, J., Dauphas, N., Davis, A.M., and Pourmand, A. A new method for MC-ICPMS measurement of Ti isotopic composition: Identification of correlated isotopic anomalies in meteorites. JAAS **26**, 2197.

References

Alexander, C.M.O., Grossman, J.N., Ebel, D.S., Ciesla, F.J., 2008. The formation conditions of chondrules and chondrites. Science 320, 1617-1619.

Bullock, E.S., Knight, K.B., Richter, F.M., Kita, N.T., Ushikubo, T., MacPherson, G.J., Davis, A.M., Mendybaev, R.A., 2013. Mg and Si isotopic fractionation patterns in types B1 and B2 CAIs: Implications for formation under different nebular conditions. Meteoritics and Planetary Sciences 48, 1440-1458.

Chen, H.-W., Lee, T., Lee, D.-C., Iizuka, Y., 2009. *In Situ* Ti Isotopic Measurements by Laser Ablation MC-ICP-MS. Terr. Atmos. Ocean. Sci. 20, 703-712.

Clayton, R.N., Mayeda, T.K., 1977. Correlated oxygen and magnesium isotope anomalies in Allende Inclusions, I: Oxygen. Geophysical Research Letters 4, 295-298.

Dauphas, N., Chen, J.H., Zhang, J., Papanastassiou, D.A., Davis, A.M., Travaglio, C., 2014. Calcium-48 isotopic anomalies in bulk chondrite and achondrites: evidence for a uniform isotopic reservoir in the inner protoplanetary disk. Earth and Planetary Science Letters 407, 96-108.

Dauphas, N., Remusat, L., Chen, J.H., Roskosz, M., Papanastassiou, D.A., Stodolna, J., Guan, Y., Ma, C., Eiler, J.M., 2010. Neutron-rich chromium isotope anomalies in supernova nanoparticles. The Astrophysical Journal 720, 1577-1591.

Davis, A.M., Hashimoto, A., Clayton, R.N., Mayeda, T.K., 1990. Isotope Mass Fractionation during Evaporation of Mg_2SiO_4. Nature 347, 655-658.

Ebel, D.S., Grossman, L., 2000. Condensation in dust-enriched systems. Geochimica et Cosmochimica Acta 64, 339-366.

Friedrich, J.M., Ebel, D.S., Weisberg, M.K., Birdsell, J., 2005. The Crucible: an unusual matrix-enclosing igneous CAI in NWA 2364 (CV3), Lunar and Planetary Science Conference, Abst. # 1756.

Galy, A., Young, E.D., Ash, R.D., O'Nions, R.K., 2000. The formation of chondrules at high gas pressures in the solar nebula. Science 290, 1751-1753.

Harper, C.L., Nyquist, L.E., Shih, C.Y., Wiesmann, H., 1990. Correlated ^{96}Zr-^{50,49,47}Ti anomalies in Allende CAI: A new constraint on the origin of the neutron-rich iron peak e-process anomaly suite, Meteoritical Society, p. 369.

Huang, S., Farkaš, J., Yu, G., Petaev, M., Jacobsen, S.B., 2012. Calcium isotopic ratios and rare earth element abundances in refractory inclusions from the Allende CV3 chondrite. Geochimica et Cosmochimica Acta 77, 252-265.

Ireland, T.R., 1988. Correlated morphological, chemical, and isotopic characteristics of hibonites from the Murchison carbonaceous chondrite. Geochimica et Cosmochimica Acta 52, 2827-2839.

Ireland, T.R., 1990. Presolar Isotopic and Chemical Signatures in Hibonite-Bearing Refractory Inclusions from the Murchison Carbonaceous Chondrite. Geochimica et Cosmochimica Acta 54, 3219-3237.

Jordan, M.K., Kohl, I.E., McCain, K.A., Simon, J.I., Young, E.D., 2017. Ti isotopes: echoes of grain-scale heterogenaity in the protoplanetary disk. 48th Lunar and Planetary Science Conference Abst. 3032.

Knight, K.B., Kita, N.T., Davis, A.M., Richter, F.M., Mendybaev, R.A., 2009. Mg and Si isotope fractionation within three Type b Ca-Al-rich inclusions, 40th Lunar and Planetary Science Conference Abst. 2360.

Kööp, L., Davis, A.M., Nakashima, D., Park, C., Krot, A.N., Nagashima, K., Tenner, T.J., Heck, P.R., Kita, N.T., 2016a. A link between oxygen, calcium and titanium isotopes in 26Al-poor hibonite-rich CAIs from Murchison and implications for the heterogeneity of dust reservoirs in the solar nebula. Geochimica et Cosmochimica Acta 189, 70-95.

Kööp, L., Nakashima, D., Heck, P.R., Kita, N.T., Tenner, T.J., Krot, A.N., Nagashima, K., Park, C., Davis, A.M., 2016b. New constraints on the relationship between 26Al and oxygen, calcium, and titanium isotopic variation in the early Solar System from a multielement isotopic study of spinel-bonite inclusions. Geochimica et Cosmochimica Acta 184, 151-172.

Leya, I., Schönbächler, M., Krähenbühl, U., Halliday, A.N., 2009. New titanium isotope data for Allende and Eremovka CAIs. The Astrophysical Journal 702, 1118-1126.

Liu, M.C., McKeegan, K.D., Goswami, J.N., Marhas, K.K., Sahijpal, S., Ireland, T.R., Davis, A.M., 2009. Isotopic records in CM hibonites: Implications for timescales of mixing of isotope reservoirs in the solar nebula. Geochimica et Cosmochimica Acta 73, 5051-5079.

Loss, R. D., Lugmair, G. W., Davis, A. M., MacPherson, G. J., 1994. Isotopically distinct reservoirs in the solar nebula: isotope anomalies in Vigarano meteorite inclusions, Astrophysical Journal, 436, L193-L196.

MacPherson, G.J., Kita, N.T., Ushikubo, T., Bullock, E.S., Davis, A.M., 2012. Well-resolved variations in the formation ages for Ca-Al-rich inclusions in the early Solar System. Earth and Planetary Science Letters 331-332, 43-45.

Moynier, F., Simon, J.I., Podosek, F.A., Meyer, B.S., Brannon, J., DePaolo, D.J., 2010. Ca isotope effects in Orgueil leachates and the implications for the carrier phases of 54Cr anomalies. Astrophysical Journal, L7-L13.

Moynier, F., Agranier, A., Hezel, D.C., Bouvier, A., 2010. Sr stable isotope composition of Earth, the Moon, Mars, Vesta and meteorites. Earth and Planetary Science Letters 300, 359-366.

Moynier, F., Bouvier, A., Blichert-Toft, J., Telouk, P., Gasperini, D., Albarede, F., 2006. Europium isotopic variations in Allende CAIs and the nature of mass-dependent fractionation in the solar nebula. Geochimica et Cosmochimica Acta 70, 4287-4294.

Moynier, F., Pringle, E.A., Bouvier, A., Moureau, J., 2015. Barium stable isotope composition of the Earth, meteorites, and calcium-aluminum-rich inclusions. Chemical Geology 413, 1-6.

Nagahara, H., Ozawa, K., 2000. Isotopic fractionation as a probe of heating processes in the solar nebula. Chemical Geology 169, 45-68.

Niederer, F.R., Papanastassiou, D.A., and Wasserburg, G.J., 1980. Endemic isotopic anomalies in titanium. The Astrophysical Journal, 240, L73-L77.

Niederer, F.R., Papanastassiou, Wasserburg, G.J., 1981. The isotopic composition of titanium in the Allende and Leoville meteorites. Geochimica et Cosmochimica Acta 45, 1017-1031.

Niederer, F.R., Papanastassiou, D.A., 1984. Ca Isotopes in Refractory Inclusions. Geochimica et Cosmochimica Acta 48, 1279-1293.

Niederer, F.R., Papanastassiou, D.A., Wasserburg, G.J., 1985. Absolute Isotopic Abundances of Ti in Meteorites. Geochimica et Cosmochimica Acta 49, 835-851.

Niemeyer, S., 1988. Titanium Isotopic Anomalies in Chondrules from Carbonaceous Chondrites. Geochimica et Cosmochimica Acta 52, 309-318.

Papanastassiou, D.A. and C. A. Brigham (1989) The identification of meteorite inclusions with isotope anomalies. Astrophysical Journal (Letters) 338, L37-L40.

Petaev, M., Jacobsen, B., 2009. Petrologic study of SJ101, a new forsterite-bearing CAI from the Allende CV3 chondrite. Geochimica et Cosmochimica Acta, 5100-5114.

Richter, F.M., Davis, A.M., Ebel, D.S., Hashimoto, A., 2002. Elemental and isotopic fractionation of Type B calcium-, aluminum-rich inclusions: Experiments, theoretical considerations, and constraints on their thermal evolution. Geochimica et Cosmochimica Acta 66, 521-540.

Russell, W.A., Papanastassiou, D.A., Tombrello, T.A., 1978. Ca Isotope Fractionation on Earth and Other Solar-System Materials. Geochimica et Cosmochimica Acta 42, 1075-1090.

Sahijpal, S., Goswami, J.N., 1998. Refractory phases in primitive meteorites devoid of 26Al and 41Ca: representative of samples of first solar system solids? The Astrophysical Journal 509, L137-L140.

Sahijpal, S., Goswami, J.N., Davis, A.M., 2000. K, Mg, Ti, and Ca isotopic compositions and refractory trace element abundances in hionites from CM and CV meteorites: implications for early solar system processes. Geochimica et Cosmochimica Acta, 1989-2005.

Schauble, E.A., 2011. First-principles estimates of equilibrium magnesium isotope fractionation in silicate, oxide, carbonate and hexaaquamagnesium(2^{+}) crystals. Geochimica et Cosmochimica Acta 75, 844-869.

Shiller, M., Paton, C., Bizzaroo, M., 2015. Evidence for nucleosynthetic enrichement of the protosolar molecular coloud core by multiple supernova events. Geochimica et Cosmochimica Acta 149, 88-102.

Shahar, A., Young, E.D., 2007. Astrophysics of CAI formation as revealed by silicon isotope LA-MC-ICPMS of an igneous CAI. Earth and Planetary Science Letters 257, 497-510.

Simon, J.I., DePaolo, D.J., 2010. Stable calcium isotopic composition of meteorites and rocky planets. Earth and Planetary Science Letters 289, 457-466.

Simon, J.I., DePaolo, D.J., Moynier, F., 2009. Calcium isotope composition of meteorites, Earth, and Mars. Astrophysical Journal 702, 707-715.

Simon, J.I., Young, E.D., 2011. Resetting, errorchrons and the meaning of canonical CAI initial $^{26}Al/^{27}Al$ values. Earth and Planetary Science Letters 304, 468-482.

Simon, J.I., Young, E.D., Russell, S.S., Tonui, E.K., Dyl, K.A., Manning, C.E., 2005. A short timescale for changing oxygen fugacity in the solar nebula revealed by high-resolution Al-26-Mg-26 dating of CAI rims. Earth and Planetary Science Letters 238, 272-283.

Trinquier, A., Bizzarro, M., Ulfbeck, D., Elliott, T., Coath, C.D., Mendybaev, R.A., Richter, F.M., Krot, A.N., 2008. Origin of Ti isotope heterogeneity in the protoplanetary disk. Geochimica et Cosmochimica Acta 72, A956-A956.

Trinquier, A., Elliott, T., Ulfbeck, D., Coath, C.D., Krot, A.N., Bizzarro, M., 2009. Origin of Nucleosynthetic Isotope Heterogeneity in the Solar Protoplanetary Disk. Science 324, 374-376.

Uyeda, C., Tsuchiyama, A., Okano, J., 1991. Magnesium isotopic fractionation of silicates produced in condensation experiments. Earth and Planetary Science Letters 107, 138-147.

Valdes, M.C., Moreira, M., Foriel, J., Moynier, F., 2014. The nature of Earth's building blocks as revealed by calcium isotopes. Earth and Planetary Science Letters 394, 135-145.

Wasserburg, G.J., Lee, T., Papanastassiou, D.A., 1977. Correlated O and Mg isotopic anomalies in Allende inclusions: II Magnesium. Geophysical Research Letters 4, 299-302.

Wark, D.A., Lovering, J.F., 1977. Marker events in the early evolution of the solar system: Evidence from rims on Ca-Al-rich inclusions in carbonaceous chondrites. Proceedings of Lunar Science Conference 8th, 95-112.

Williams, C.D., Janney, P.E., Hines, R.R., Wadhwa, M., 2016. Precise titanium isotope compositions of refractory inclusions in the Allende CV3 chondrite by LA-MC-ICPMS. Chemical Geology 436, 1-10.

Williams, C.D., Wadhwa, M., Janney, P.E., Hines, R.R., Bullock, E.S., MacPherson, G.J., 2012. Ti, Si and Mg Isotope Systematics of FUN CAI CMS-1, 75th Annual Meeting of the Meteoritical Society, Abst. # 5102.

Yamada, M., Tachibana, S., Nagahara, H., Ozawa, K., 2006. Anisotropy of Mg isotopic fractionation during evaporation and Mg self-diffusion of forsterite in vacuum. Planetary and Space Science 54, 1096-1106.

Young, E.D., 2016. Bayes' theorem and early solar short-lived radionuclides: the case for an unexceptional origin for the solar system. The Astrophysical Journal 826:129, 6pp.

Young, E.D., Galy, A., Nagahara, H., 2002. Kinetic and equilibrium mass-dependent isotope fractionation laws in nature and their geochemical and cosmochemical significance. Geochimica et Cosmochimica Acta 66, 1095-1104.

Young, E.D., Nagahara, H., Mysen, B.O., Audet, D.M., 1998. Non-Rayleigh oxygen isotope fractionation by mineral evaporation: Theory and experiments in the system SiO_2. Geochimica et Cosmochimica Acta 62, 3109-3116.

Young, E.D., Simon, J.I., Galy, A., Russell, S.S., Tonui, E., Lovera, O., 2005. Supra-canonical Al-26/Al-27 and the residence time of CAIs in the solar protoplanetary disk. Science 308, 223-227.

Zhang, J., Dauphas, N., Davis, A.M., Leya, I., Fedkin, A., 2012. The proto-Earth as a significant source of lunar material. Nature Geoscience 5, 251-255.

Zhang, J., Dauphas, N., Davis, A.M., Pourmand, A., 2011. A new method of MC-ICPMS measurement of titanium isotopic composition: Identification of correlated isotope anomalies in meteorites. Journal of Analytical Atomic Spectrometry 26, 2197-2205.

Zhang, J., Huang, S., Davis, A.M., Dauphas, N., Hashimoto, A., Jacobsen, S.B., 2014. Calcium and titanium isotopic fractionations during evaporation. Geochimica et Cosmochimica Acta 140, 365-380.

Zhu, X.K., Makishima, A., Guo, Y., Belshaw, N.S., O'Nions, R.K., 2002. High precision measurement of titanium isotope ratios by plasma source mass spectrometry. International Journal of Mass Spectrometry 220, 21-29.

Chapter 2: Isotopic Compositions of Refractory Inclusions as Echoes of Molecular Cloud Isotope Heterogeneity

Michelle K. Jordan[1], Issaku E. Kohl[1], Kaitlyn A. McCain[1], Justin I. Simon[2], Edwin A. Schauble[1], and Edward D. Young[1]

[1] Department of Earth, Planetary, and Space Sciences, UCLA, Los Angeles, CA, USA

[2] Center for Isotope Cosmochemistry & Geochronology, Astromaterials Research and Exploration Science Division, NASA-Johnson Space Center, Houston, TX, USA

2.1. Introduction

The protoplanetary disk was the rotating circumstellar disk of gas and dust that surrounded our newly formed Sun early in the Solar System's early history. The formation of rocky materials in the protoplanetary disk is a necessary process advancing the growth of terrestrial planets. Refractory inclusions, otherwise referred to as calcium-aluminum-rich inclusions (CAIs), are the oldest surviving solids that formed in the Solar System and were present during the earliest stages of the Solar System. These objects provide a record of the conditions present in the region of the protoplanetary disk where they accreted. CAIs let us probe the distant past and offer insight about the origin of the Solar System and planets. We can learn about the conditions present in the nascent Solar System, the processes by which they formed, and the precursor material from which CAIs, and eventually, planets formed.

In particular, the isotopic compositions of CAIs are good monitors of volatility as they are primarily controlled by it. The isotopic effects of evaporation are well understood through both theory and experimental work (e.g., Davis et al. 1990; Young et al. 1998; Grossman et al. 2000; Alexander 2001; Richter et al. 2002; Richter 2004; Richter et al. 2007; Shahar and Young

2007; Grossman et al. 2008; Knight et al 2009). Evaporation expresses itself as an enrichment in the heavy isotopes of a given species in the more condensed phase, due the loss of the lighter, more volatile isotopes.

Condensation, like evaporation, may also be exhibited by the isotopic compositions of objects, though the isotopic effects of condensation are less well-understood. Potentially, mass-dependent fractionation can provide a record of nebular condensation. Mineralogically, the compositions of CAIs are similar to equilibrium thermodynamic predictions for condensation from a solar gas (Grossman, 1972). In this study, we present a model for condensation and explore its isotopic consequences. There exist suggestions that CAIs may not have condensed from a solar nebula gas. Instead, it is postulated that CAIs are the evaporative residues of chondritic material, which were never heated enough to fully vaporize. Furthermore, these objects may have experienced multiple cycles of reheating, partial evaporation, and recondensation, rendering interpretation of isotopic compositions problematic (McPherson, 2014; reference therein). Our ability to assess whether CAIs are primary condensates from solar gas or evaporative residues of chondritic material will place important constraints on the formation and histories of these primitive solids.

Previous work has shown a light isotope enrichment of Ca and Sr in igneous CAIs (Niederer and Papanastassiou 1984; Huang et al. 2012; Patchett 1980, Moynier et al. 2010; Charlier et al. 2012). When assessing the light isotope enrichments observed in CAIs, we assume that these elements are condensing from a nebular gas with a chondritic composition. However, we do not definitively know the composition of the gas. Relying on self-consistency between different isotopic systems allows us to better assess if these isotopic signatures are indeed the expression of condensation, without relying on the assumption of the initial composition.

We measured the isotopic compositions of several major rock-forming elements in CAIs and developed self-consistent models that explain the relative enrichments and depletions of nuclides. Mg, Si, Ca, and Ti isotope compositions were measured for a suite of CAIs representing both type A and type B varieties in CV chondrites. Ca and Ti are particularly useful due to their refractory nature. Aside from aluminum, Ti and Ca are the first major elements to condense (i.e. that have the highest condensation temperatures) and are less susceptible to evaporation. This allows us to account for the effects of condensation in objects that have likely been subjected to multiple cycles of reheating and partial evaporation. Furthermore, these elements give us the opportunity for a better assessment of the initial isotopic ratios of the more volatile Mg and Si, prior to evaporation. By measuring several elements with different volatilities in a single object, we can better understand the objects formation history, location in the protoplanetary disk, and source material. Performing this study for a collection of CAIs helps us to form a more complete picture of CAI formation and the early Solar System.

In addition to our measurement and analysis of mass-fractioned isotopes in CAIs, we measured anomalous ^{50}Ti for of all CAIs in this study. Our data provide a means to the evaluate heterogeneity of the source material from which CAIs formed. We also measured the excess ^{26}Mg (^{26}Mg*) of the CAIs, which results from the decay of ^{26}Al. Analyzing the excess ^{26}Mg and the range of inferred initial ^{26}Al/^{27}Al in primitive solar system materials can also provide clues about the heterogeneity of precursor materials. We believe that the CAI isotopic compositions that we measure and observe represent the averaging of grains in star forming regions (SFRs), which displayed more widely distributed compositions. Thus, the information provided by these small objects potentially have remarkably large-scale implications.

2.2 Condensation Theory

If CAIs are direct nebular condensates, isotopic fractionation can be produced by non-equilibrium condensation, which occurs when a gas is undercooled. We consider the isotopic consequences of condensation from a nebular gas in terms of the kinetics of condensation, the degree of undercooling, and potential reservoir effects. The isotopic effects of condensation are difficult to describe from theory relative to those resulting from evaporation. This is due to uncertainties in the energetics associated with the nuclide sticking to and inserting itself into the condensed phase. We must not only consider transport to the surface, but also this insertion, which has been absent from previous models.

Unlike evaporation fractionation factors (α_{evap}) we are unable to measure condensation fractionation factors in the laboratory. Thus, a model is needed to indirectly elicit the fractionation associated with the insertion of a molecule into the condensate. We invoke the law of mass action, which asserts that equilibrium fractionation is a combination of the rate of insertion into the solid phase and the rate of evaporation.

$$\alpha_{\mathrm{eq}} = \frac{\alpha_{\mathrm{insert}}}{\alpha_{\mathrm{evap}}}. \tag{2.1}$$

In this equation, the equilibrium fractionation factors (α_{eq}) can be calculated from theory and evaporation fractionation factors can be measured in the laboratory. This allows us to solve for α_{insert},

$$\alpha_{\mathrm{insert}} = \alpha_{\mathrm{eq}} \cdot \alpha_{\mathrm{evap}}, \tag{2.2}$$

which is the fractionation occurring at the surface of the condensate. The overall kinetic fractionation includes the ability of a molecule to incorporate itself in the solid phase as well as the transport to the surface, collisional frequency. The fractionation due to collisional frequency is described as follows:

$$\alpha_{coll} = \sqrt{\frac{\mu_i}{\mu_i'}}, \tag{2.3}$$

where, μ_i and μ_i' are the reduced masses for the lighter and heavier isotopes of species i, respectively. This equation indicates that the heavier mass collides with the condensate less frequently. As a result, we expect the lighter mass to stick to the surface more often based on its higher collisional frequency. Taking into account both collisional frequency and insertion, provides an equation for the kinetic fractionation of condensation:

$$\alpha_{kin} = \alpha_{evap}\alpha_{eq}\sqrt{\frac{\mu_i}{\mu_i'}} \tag{2.4}$$

When examining CAI formation in the Solar Nebula, we are concerned with the condensation of a liquid/solid from vapor. For equilibrium partitioning between a gas and a liquid/solid at near equilibrium conditions, the condensed phase typically favors the heavier nuclide due to the presence of more and/or stiffer bonds and thus, a greater sensitivity to frequencies of vibration of isotope substitution. The competing kinetic and equilibrium fractionation mechanisms render the isotopic effects of condensation convoluted.

The degree of saturation controls the relative contributions from equilibrium and kinetic isotope fractionation. To quantify the degree of saturation, we define a saturation index, $S_i = P_i/P_{eq,i,}$ In this equation, P_i is the partial pressure of the element of interest in the vapor and $P_{eq,i}$ is the partial pressure of that element at equilibrium. It follows that at equilibrium, the saturation index is equal to 1, while $S_i > 1$ implies condensation as this describes the case where P_i is greater than $P_{eq,i}$ and we have an overstepping of equilibrium.

The incorporation of kinetic fractionation for condensation of snow via vapor deposition was modeled by Jouzel and Merlivat (1984). Simple Rayleigh fractionation could not explain the observed isotopic compositions of snow at the poles as it only incorporates equilibrium fractionation, not accounting for the kinetic effect that occurs as a result of the fact that

deposition happens in an environment supersaturated over ice. Simon and DePaolo (2010) followed the method of Jouzel and Merlivat and adapted the model for condensation in meteorites:

$$\alpha_{cond} = \frac{\alpha_{eq}(P_i/P_{i,eq})}{(\alpha_{eq}/\alpha_{coll})\left(\frac{P_i}{P_{i,eq}}-1\right)+1} \tag{2.5}$$

We modify their equation by including the equation for α_{kin} (Young and Schauble, 2012) and substituting the saturation index. Thus, the complete model for fractionation associated with condensation is:

$$\alpha_{cond} = \frac{\alpha_{eq}\alpha_{kin}S_i}{\alpha_{eq}(S_i-1)+\alpha_{kin}} \tag{2.6}$$

When $S_i = 1$ (i.e. equilibrium),

$$\alpha_{cond} = \frac{\alpha_{eq}\alpha_{kin}}{\alpha_{eq}(0)+\alpha_{kin}} = \alpha_{eq}. \tag{2.7}$$

When $S_i >> 1$,

$$\alpha_{cond} \sim \frac{\alpha_{eq}\alpha_{kin}S_i}{\alpha_{eq}S_i} = \alpha_{kin}. \tag{2.8}$$

Figure 2.1 shows how isotopic composition varies with respect to the initial composition, which we assume to be chondritic, at different values of S_i. At higher values of S_i, increasingly lighter isotopic compositions are produced for the condensed phase.

If the reaction pathway is known, S_i can be equated with a temperature difference departing from the equilibrium condensation temperature. Therefore, S_i corresponds to the degree of undercooling, which occurs when the gas is cooled below the equilibrium condensation temperature. The situation is analogous to the production of snow in clouds. Saturation is converted to a degree of undercooling using the van't Hoff equation and the enthalpy for the condensation reaction (Jouzel and Merlivat, 1984). Figure 2.2 shows the degree of undercooling as a function of the saturation index.

In addition to the kinetic isotope effects, there are also reservoir effects that must be considered. For condensation, the remaining gas becomes progressively enriched in the heavy isotopes relative to the light isotopes as the condensate is extracted. Because the gas is likely to be well-mixed, we can apply the concept of Rayleigh fractionation to this scenario. Using Rayleigh fractionation, one can calculate the isotopic composition of the condensed phase (liquid or solid) in terms of the fraction of the element of interest remaining in the gas phase:

$$\delta_{cond} = \left(\delta^0_{gas} + 10^3\right)\alpha^{c/g} f^{\alpha-1} - 1000. \quad (2.9)$$

We are left with two competing effects, the reservoir effect that progressively enriches the condensate in heavier isotopes relative to light isotopes, and the kinetic effects of condensation that favor light isotopes in the condensed phase. Figure 2.2 shows the complete model for Ca and Ti including reservoir effects. The figure indicates the expected fractionation at different degrees of undercooling for varying values of *f*.

2.3. Samples

This study includes isotopic measurements of 15 CAIs. Our intent is to measure Mg, Si, Ca, and Ti isotopic compositions in each CAI. These measurements are still in progress. The data collected thus far is presented in this paper. The suit of CAIs includes several refractory inclusions from Allende: SJ101, AMNH 4947 Bocce Ball, Al4884, EK5-2-1R, 461_3b3, 461_13 B, MKJ1, MKJ2, KAM J1, KAM L1, KAM L2 B, and KAM L2-F. Other CAIs in this study include L144A from Leoville, E44 from Efremovka, and the Crucible from NWA 2364.
The CAIs in this study are all from CV3 chondrites, which contain both various sizes and types of CAIs. Although possessing a range of sizes, including relatively small CAIs, the CV3 meteorites group contains the largest CAIs of any chondrite group. The large sizes allow us to obtain spatial information for the CAI analyses and determine if there is any isotopic variance

associated with phase or distance from the rim. The diversity of CAI types present in the CV3 chondrites allows us to sample various types of CAIs.

SJ101 is a large (6.34 g, ~25 x 15 mm) forsterite-bearing CAI (FoB) from Allende (CV3). The CAI predominantly consists of large areas of Al-rich spinel-clinopyroxene (Sp-Cpx) lithology. Sinuous bands of Al-rich pyroxene with enclosed euhedral forsterite crystals throughout. The two major lithologies are separated by a transition zone of clinopyroxene enclosing both forsterite and spinel. The whole inclusion is surrounded by a Cpx-Sp-anorthite rim. Differing from other FoBs, SJ101 has no Wark-Lovering rim or Al-enriched mantle (Jacobsen et al. 2008).

Al4884 is an approximately 0.6 x 1.0 cm type B1, oval-shaped CAI from Allende with a microfaulted surface (Bullock et al., 2013). The core contains abundant melilite, fassaite, spinel and some anorthite. It has a ~250-500 μm melilite mantle with minor spinel. Like many Allende CAIs, it contains areas of secondary alteration. Al4884 contains Ti-rich pyroxene with the phase containing ~5-17 wt. % TiO_2, allowing for robust Ti analyses (Bullock et al., 2013).

AMNH AL4947 is a type B2 CAI from Allende. Nicknamed and hereafter referred to as Bocce Ball due to its spherical shape, the inclusion is ~6 mm in diameter (Connolly et al., 2006; Connolly et al, 2011). Petrographically, it has course grained crystals of melilite, fassaite, anorthite, and spinel in a fine grained matrix. There are also porous regions of alteration minerals that appear to be replacing melilite (Connolly et al. 2006). Outside the course-grained region of the CAI, there is a mixture of fassaite and melilite of varying size and angularity. A thin Wark-Lovering rim (up to 20 μm) surrounds the object. Mg, Al, Si, and Ti zonation is observed in fassaite with concentrations of MgO and SiO_2 increasing towards the rim and Al_2O_3 and TiO_2

decreasing towards the rim. Ca is consistent throughout. Akermanite content of the melilite increases from interior to rim (Connolly et al., 2006).

EK5-2-1R from Allende is a course-grained, type A CAI. The inclusion is approximately 3 x 3 mm, though it should be noted that the sample is a slice of a larger object. The object contains hibonite, perovskite, and, in some case, spinel within the melilite core. Secondary sodalite and nepheline are located at the outer edge of the melilite interior (Simon et al., 2017). 461 3B3 is a fine-grained inclusion from Allende that is a fragment of a larger CAI measuring ~10 x 10 mm in size. The object contains spinel, hibonite, and alkali-rich melilite and lacks a Wark-Lovering rim as is common for fine-grained CAIs (Simon et al., 2017).

Allende CAI 461 B is an irregularly shaped, fine-grained type A CAI (Simon et al., 2017). Subsequent to microdilling for the Ca analysis, the object was repolished to remove the pits from microdrilling and measured ~1 x 2 mm in size for the remaining analyses. There is a hibonite mantle surrounding an aggregate interior containing spinel and hibonite grains. The object displays a Group II REE pattern, indicating that it is not igneous.

L144A is a type A, compact, oval-shaped CAI from Leoville and measures about 10 x 6 mm. It has fine grained intergrown melilite and rare Ti-Al-rich pyroxene that micron-sized perovskite grains. Spinel is present throughout the CAI. The Wark-Lovering rim composed of an inner layer of spinel, hibonite, melilite, and calcic pyroxene. The outer layer is composed predominately of Al-rich pyroxene. The TiO_2 content of the pyroxenes varies from 2-7 wt. % for interior grains up to 17-19 wt % for those grains near the rim (Simon et al., 2005).

The Crucible is a large type B CAI from the chondrite, NWA 2364 (CV3) with its largest diameter being ~18 mm. The object is deformed, enveloping the surrounding chondrite in a cup shape that gives the CAI its name. It has coarsely crystalline fassaite regions, often surrounded

by melilite and primary anorthite. Euhedral spinel is heterogeneously distributed throughout the primary phases (Friedrich et al., 2005; Burkhardt et al., 2008). Melilite compositions decrease in akermanite content from core to rim. Some melilite has been altered to secondary anorthite. Two rims with similar mineralogies surround the object; the rims are comprised of melilite, Fe-rich spinel, Al-diopside. The interior fassaitic pyroxene contains up to 19.1% TiO_2 and can be up to 500 μm in diameter; the Ti concentration and size of this phase makes Ti analysis by laser ablation very attainable (Burkhardt et al., 2008).

MKJ1 from Allende is a fluffy type A CAI that is ~2.5 x 5 mm. The object has abundant Al-rich melilite which is anhedral to subhedral in shape. Fassaite and spinel are associated with seemingly independently rimmed objects that result from the intertwining of matrix and CAI material.

MKJ 2 is ~2.5 x 4 mm and forms a pseudo rectangular shape, which is in part due to how the piece was broken off from a larger slab. This CAI is fine grained and its mantle is somewhat diffuse. The core consists mainly of spinel with a predominately melilite mantle. It appears that this CAI experienced significant alteration.

KAM J1 is an oval-shaped type B1 CAI from Allende. The mantle is predominately melilite. The core contains fassaite, spinel, and some hibonite. It measures ~4 x 3 mm in size. KAM L1 is an irregularly-shaped Type B CAI containing a large mantle of melilite, perovskite, and fassiaite, with a core rich in spinel and hibonite. The objects meaures ~4.5 x 2 mm. KAM L2 B is an elongated Type B CAI, ~ 4 x 1 mm in size. The object contains melilite, fassaite, anorthite, and pervoskite. Spinel is concentrated on one side of the object, perhaps, suggesting deformation. KAM L2 F is a fluffy type A CAI. It measures ~3 x 1.5 mm

Type A CAIs, especially fluffy type A, are of particular interest as these objects are believed to have never been molten and have the most refractory compositions (lower MgO and SiO_2). If any CAIs display compositions consistent with condensation, we would expect it to manifest in type A CAIs.

For the samples prepared at UCLA, segments of chondrite containing individual CAIs were cut from larger slabs or rock fragments using a diamond blade saw. Thick sections of all samples were mounted in epoxy. To ensure that the sample surfaces were flat and adequate for analyses, the mounts were first polished using sandpaper and then a series of diamond slurries, decreasing in grit size with each subsequent step. The final step of the polishing regimen uses a ¼ micron grit size. After each day of analyses, samples were repolished with the ¼ micron grit diamond slurry to remove any material remaining on the surface due to laser ablation and ensure that the surface is flat for future analyses.

2.4. Analytical Methods

In-situ analyses for Mg, Si, and Ti were conducted using laser ablation multiple-collector inductively coupled plasma-source mass spectrometry (LA-MC-ICPMS, ThermoFinnegan Neptune^{TM}). The 193 nm excimer laser (Photon-Machines, Analyte 193) was operated at a UV fluence of 20-28 J/cm^2. For all analyses, sample-standard bracketing was used to correct for instrumental mass bias and isotope analyses were corrected by subtracting a preceding on-peak background measurement. All measurements were made using Faraday cups with 10^{11} Ω resistors. Each measurement encompasses 10 cycles of 4s integrations. Ca and Ti (solution) analyses were measured on a thermal ionization mass spectrometer (TIMS, ThermoFinnegan

Triton^{TM}) at NASA's Johnson Space Center. Sample preparation and analytical methods for Ca and Ti by solution are outlined in Simon et al. (2017).

Mg Analyses. Material was ablated at a pulse repetition rate of 2 Hz, forming pits of 86 µm for the CAIs. Helium (0.17 l/min) carried ablated material from the sample chamber to a mixing chamber where it combines with Ar (0.69 l/min) and N_2 (8 l/min) before being introduced into the ICP torch. N_2 is used to increase sensitivity. Faraday collectors were spaced to collect $^{24}Mg^+$, $^{25}Mg^+$, $^{26}Mg^+$, and $^{27}Al^+$. Analyses were run with a mass resolving power (m/Δm) of ~4000 for Mg, removing the effect of mass interferences. Typical $^{25}Mg^+$ intensities are ~ 1 V. Results are reported as per mil deviations from a standard:

$$\delta^{25}Mg = \left(\frac{\left(^{25}Mg/^{24}Mg\right)_{unknown}}{\left(^{25}Mg/^{24}Mg\right)_{std}} - 1 \right) x\ 10^3. \qquad (2.10)$$

The standard for the Mg analyses was a polished slice of USNM forsterite #136718, San Carlos olivine, which is understood to be chondritic. Prior to sample analyses, the standard is measured against itself to ensure that isotopic fractionation does not occur during the measurement, this requires a measured value of 0‰ within error equal to our level of analytical precision (zero enrichment). The olivine standard is measured using a smaller spot size (34 µm for Mg analyses, 52 µm for Si analyses) than that used for the other standards and CAIs, due to the high concentration of Mg in the olivine relative to the other materials. Test were conducted to ensure that differences in spot size (or repetition rate, in some cases) did not affect the resulting data. For the range of parameters used in this study, differences in spot size and repetition rate did not alter the measured isotopic compositions.

Al/Mg ratios were calibrated by measuring San Carlos olivine against Burma spinel and an Al-Ti diopside glass (P10, fassaite composition). Made at UCLA, P10 is a synthetic Ti and Al-rich glass with the composition $Ca_{0.97}Mg_{0.54}Si_{1.53}Al_{0.77}O_6$ (electron microprobe analysis). The use of this Ca-rich material is important for the Mg analyses due to interferences. Measured values for $^{27}Al/^{24}Mg$ in both the spinel and glass were collected and then normalized to accepted values. The average $^{27}Al/^{24}Mg$ correction determined from these measurements is used to correct the $^{27}Al/^{24}Al$ of the unknowns.

To correct for mass interferences from $^{48}Ca^{++}$, which interferes with $^{24}Mg^{+}$, we measured terrestrial vesuvianite. Vesuvianite is a Ca-Mg-Al silicate with the chemical formula $Ca_{10}(Mg, Fe)_2Al_4(OH)_4(SiO_4)_5(Si2O7)_2$. We use this mineral to calibrate the $^{48}Ca^{++}$ interference effect on measured Mg-isotope ratios, which can be expressed in terms of the ratio of the per mil $^{26}Mg/^{24}Mg$ error to the bulk Ca/Mg. We can calculate the Ca/Mg from our measurements of Al/Mg since Ca/Al is fixed due to the stoichiometry of the mineral formula (Ca/Al = 5/2) and Ca/Al x Al/Mg = Ca/Mg. Al/Mg is determined from our measurement of $^{27}Al/^{24}Mg$ and the ratio of $^{24}Mg/Mg$ (0.7899), ($^{24}Mg/Mg$) x ($^{27}Al/^{24}Mg$) give us the Al/Mg ratio. Thus, the complete equation for determining Ca/Mg of the mineral is $(5/2)(0.7899)(^{27}Al/^{24}Mg)_{measured}$. We use this in conjunction with our measured ^{26}Mg excess (the terrestrial vesuvianite should have no excess, but one is measured due to this interference) to correct for the 44/24 mass bias of the instrument. To do this, we find the deviation of our $\delta^{26}Mg$ measurement from the mass fractionation line ($\Delta^{26}Mg$') and divide this by the determined Ca/Mg ration, to find that we require a correction of ~0.14‰ per unit Ca/Mg.

To calculate radiogenic ^{26}Mg values, we use the measured values for $^{25}Mg/^{24}Mg$ and $^{26}Mg/^{24}Mg$ and express them in linear delta notation (δ') relative to the accepted standard for Mg isotopes, DSM3. Mathematically, these linear delta forms are determined as follows:

$$\delta\,^{i}Mg = \ln\left(\frac{\left(\,^{i}Mg/^{24}Mg\right)_{sample}}{\left(\,^{i}Mg/^{24}Mg\right)_{DSM3}}\right) \cdot 10^{3}, \tag{2.11}$$

where i refers to either 25 or 26. Using these delta values we calculated excess ^{26}Mg according to the following formula:

$$\delta^{26}Mg^{*} = \delta^{26}Mg' - \delta^{25}Mg' /(0.514). \tag{2.12}$$

In this equation, 0.514 is the slope of the mass-dependent fractionation line between $\delta^{25}Mg$' and $\delta^{26}Mg$'.

Si analyses. Faraday collectors were spaced to collect $^{28}Si^{+}$, $^{29}Si^{+}$, and $^{30}Si^{+}$ simultaneously. Molecular interferences were resolved by running at a mass resolving power of approximately 7800 or higher. Samples were measured against an in-house standard, USNM forsterite, San Carlos olivine. Following successful zero enrichment measurements, the olivine standard was then measured against the P10, diopside glass standard. The synthetic glass ($Di_{0.59}An_{0.41}$) has a 1% ^{28}Si spike (Oak Ridge silicon batch no. 143292: 99.94% ^{28}Si, 0.04% ^{29}Si, 0.02% ^{30}Si). The gravimetric $\delta^{28}Si$ and $\delta^{30}Si$ values are -10.70 and -10.72‰, respectively, relative to NBS-28. LA-MC-ICPMS analyses of the glass reproduce these gravimetric values. Typical $^{29}Si^{+}$ signal intensities were on the order of ~600 mV. Ar, He, and N_2 flows were 0.69 l/min, 0.6 l/min, and 4.5 l/min, respectively. Spot sizes for CAI analyses ranges from 52-138 μm depending on Si concentration. Analyses were conducted at a repetition rate of 2 Hz, ablating mainly melilite and fassaite, with varying amounts of spinel included.

Analyses are reported as per mil deviations from the international standard for Si isotope ratio measurements, NBS-28 quartz:

$$\delta^{29}Si = \left(\frac{\left({}^{29}Si/{}^{28}Si\right)_{unknown}}{\left({}^{29}Si/{}^{28}Si\right)_{std}} - 1 \right) x\ 10^3. \quad (2.13)$$

Samples are measured against San Carlos olivine and a factor of ~-0.2‰ is used to adjust our data to the NBS-28 scale

Ti Analyses. Ti measurements were predominately made in Ti-rich pyroxene with perovskite and hibonite sometimes present in the analyzed area. Spot sizes for Ti analyses ranged from 86-172 µm depending upon the concentration of Ti. Samples were run using a repetition rate of 3-6 Hz. Tests were conducted in order to ensure the difference in repetition rate between sample and standard did not affect isotopic composition. Gas flows were set at He = 0.29 l/min, Ar =0.69 l/m, and N_2 = 8 l/min. Faraday cups were spaced to collect $^{47}Ti^+$, $^{49}Ti^+$, $^{50}Ti^+$, $^{51}V^+$, and $^{52}Cr^+$. The mass resolving power for the Ti analyses was ~7000 or greater. Data are reported as per mil deviations from the standard, such that

$$\delta^{49}Ti = \left(\frac{\left({}^{49}Ti/{}^{47}Ti\right)_{unknown}}{\left({}^{49}Ti/{}^{47}Ti\right)_{std}} - 1 \right) x\ 10^3. \quad (2.14)$$

Our standard for Ti is a terrestrial rutile (USNM 83191). The $^{49}Ti/^{47}Ti$ ratio is reported as it is the least sensitive to interferences and is essentially free from nuclear anomalies at the 0.1‰ level or greater (Zhang et al. 2011, Williams et al. 2014). We have demonstrated our ability to measure $^{49}Ti/^{47}Ti$ free from matrix effects within our current analytical precision of ~0.15-0.2‰ (1 SE) (Simon et al., 2017). A second standard, UCLA Glass #5 (P10), was used to demonstrate the lack of matrix effects. UCLA Glass #5 has a fassaite chemical composition and is known to have a chondritic Ti isotopic composition, having previously been measured for Ti isotopes (Chen et al., 2009). Comparing the standard, UCLA Glass #5 against pure TiO_2 (the rutile standard) allows us

to demonstrate the lack of matrix effects as we observe no fractionation between the two. There is generally limited fractionation between terrestrial materials (Zhang et al., 2011).

Due to interferences on $^{50}Ti^{+}$ from $^{50}V^{+}$ and $^{50}Cr^{+}$, another instrumental mass fractionation correction had to be made beyond the correction from sample-standard bracketing. This fractionation factor, α_{inst}, was obtained by comparing measured $^{49}Ti/^{47}Ti$ to a nominal ratio of 0.74500 ($\alpha_{inst} = (^{49}Ti/^{47}Ti)_{meas}/0.74500$) (Niemeyer and Lugmair, 1981). This instrumental fractionation allows us to derive an exponent, β, for the general fractionation law ($\alpha_{inst} = (m_2/m_1)^{\beta}$). Given our calculated α_{inst}, $\beta = \ln(\alpha_{inst})/\ln(m^{49}/m^{47})$. Typical values for α_{inst} and β are 1.083 and 1.91, respectively. This fractionation law derived for Ti on our instrument at UCLA is used for both V and Cr to determine the portion of the measured ^{50}Ti intensity that is due to ^{50}V and ^{50}Cr. For example, $\alpha_{inst,V} = (m_{51}/m_{50})^{\beta}$, where β is determined in the manner described above. Given this fractionation factor, the intensity of ^{50}V is equal to the intensity of ^{51}V divided by the product of $\alpha_{inst,V}$ and the nominal ratio of $^{51}V/^{50}V$. The identical calculation is performed for Cr, monitoring ^{52}Cr and using this in conjunction with the determined instrumental fractionation to establish the intensity of ^{50}Cr. The resulting intensities of ^{50}V and ^{50}Cr are subtracted from the measured ^{50}Ti, to get the corrected ^{50}Ti intensity, which can then be used to calculate ^{50}Ti anomalies, $\varepsilon^{50}Ti$, where

$$\varepsilon^{50}Ti = \left(\delta^{50}Ti_{sample,corr} - \delta^{49}Ti/0.6805\right) x\ 10. \quad (2.15)$$

2.5. Data

Mass Fractionated Isotopes. The average $\delta^{25}Mg$, $\delta^{29}Si$, $\delta^{44}Ca$, and $\delta^{49}Ti$ values for each CAI are listed in Table 2.1. Individual spot analyses for Mg, Si, and Ti by laser ablation are located in Appendix B. Of those CAIs for which Mg isotope compositions were measured, two

CAIs show negative values for δ^{25}Mg (Figure 2.3). One of these is SJ101 from Allende, which has a δ^{25}Mg value of -1.6 ± 0.09‰ (2 SE). Although many FoB CAIs show isotopic evidence of melt evaporation, the negative δ^{25}Mg, negative δ^{44}Ca previously measured by Huang et al. (2012), Group II REE (Petaev and Jacobsen, 2009), and petrology provide no evidence for evaporation. Instead, these observations may indicate formation by non-equilibrium condensation. KAM L2-F also displays a negative δ^{25}Mg = -0.28‰ ± 0.06 (2 SE). KAM L2-F is a fluffy type A CAI. Petrologically, fluffy type A CAIs are more primitive than type B and compact type A CAIs as their texture show no evidence of being melted. Their lighter Mg isotopic signature may be the result of the process by which they formed and lack of later disturbance. The majority of the CAIs have positive δ^{25}Mg values, ranging from ~2.8 to 6‰. These positive values are higher than the range predicted for equilibrium condensation by our model and may be evidence of evaporation of the moderately refractory Mg. Alternatively, the compositions could reflect real variations in source material.

The data for δ^{29}Si is less variable and falls within ~3.5‰ of zero, negative values tend to lie closer to zero than positive δ^{29}Si (Figure 2.4). SJ101 is one of the CAIs possessing a negative δ^{29}Si with an average Si isotopic composition of δ^{29}Si = -0.2 ± 0.1‰. The negative δ^{29}Si is further evidence that SJ101 did not experience evaporation. There does not appear to be a correlation between CAI type and silicon isotopic composition.

δ^{49}Ti is the least variable and is typically clustered around zero, displaying relatively normal compositions that show only small mass dependent Ti fractionation (Figure 2.5). Values range from -0.7 to 0.65‰, with the majority of CAIs possessing values between -0.2 and 0.4‰. This may be explained by the fact that Ti is the most refractory of the elements being measured in this study. CAI 461_13 B displays the largest Ti mass-fractionation of this dataset with δ^{49}Ti =

-0.73 ± 0.42‰ (2 SE). Though the values in this dataset exhibit a small range, larger fractionations have been reported previously (Niederer et al., 1985, Zhang et al., 2011).

For all measured CAIs, δ^{44}Ca is negative and ranges from -11 to -0.6‰. This is below the value for typical planetary compositions (~0‰). The δ^{44}Ca data is included in our discussion, but a fuller analysis of the Ca data can be found in Simon et al. (2017).

Anomalous ^{50}Ti. Anomalous ^{50}Ti/^{47}Ti isotope effects (ε^{50}Ti) were measured for all samples. The averages for each CAI are listed in Table 1. Individual spot analyses can be found in Appendix B and are plotted in Figure 2.6. The majority of ε^{50}Ti values are between 6-13 epsilon unit, which are typical values for CAIs (Leya et al, 2009; Williams et al., 2010). For a given igneous CAI, ε^{50}Ti values are typically tightly clustered. The average values of this suite of CAIs demonstrates a bimodal distribution with values tending to fall around 0 or 8 epsilon units. The widest variability, both within a given CAI and among CAIs, is seen within those CAIs considered condensates. 461 3B3, a fine-grained condensate, stands out the most with an ε^{50}Ti value of ~41. This object displays a REE pattern that is consistent with condensation from a refractory depleted gas (Figure 2.7). MKJ1, a fluffy type A, is the only CAI in the set to exhibit clearly negative values and have a low average ε^{50}Ti of ~-0.12. L144A, another type A CAI, displays some variability between its core and "mantle". The spot analyses for the core are tightly clustered around 9 epsilon units, while the mantle of the object displays a larger variance among data points and has a lower average value of ~6 epsilon units. Thus, we see heterogeneity both within and among CAIs with regards to ^{50}Ti anomalies.

Radiogenic Mg. Radiogenic Mg and ^{27}Al/^{24}Al for individual spot analyses can be found in Appendix B. Isochrons for the CAIs measured in this study can be found in Appendix C. Mg data and plots for E44 and L144A were originally published in Young et al. (2005).

2.6. Discussion

Using our condensation model, published evaporative fluxes, gas-solid equilibrium factors, and experimentally determined evaporation fractionation factor, we calculate the expected shifts in isotopic ratios as a function of oversaturation, S_i. One would expect the degrees of undercooling to be similar for those elements with similar condensation temperatures. Thus, Mg and Si should experience similar degrees of undercooling and Ca and Ti should also experience similar degrees of undercooling, though potentially different from that of Mg and Si. Figure 2.8 shows the correlation between δ^{25}Mg and δ^{29}Si as a function of S_i at ~1400 K. Figure 2.9 shows the same relationship for δ^{44}Ca and δ^{49}Ti at ~1600 K, as these elements have higher condensation temperatures.

The data show that there is a lack of correlation between ^{44}Ca and ^{49}Ti. Similarly, there is a lack correlation between δ^{25}Mg and δ^{29}Si, which are more volatile than Ca and Ti, but have similar volatilities to each other. The lack of correlation between Ca and Ti implies that these elements did not experience the same condensation history and were inherited from different reservoirs. The lack of correlation between Mg and Si further supports this conclusion since these two elements are also expected to have experienced similar degrees of undercooling. For many of these objects the elevated δ^{26}Mg and δ^{29}Si values indicate that the CAI experienced evaporation subsequent to condensing. In this case, would not expect to observe correlation between the two systems as the curve represents condensation. However, SJ101 consistently displays signatures of condensation, yet we still observe a lack of correlation between Mg and Si, as well as the more refractory Ca and Ti. The presence of distinct reservoirs implies that CAIs are aggregates of pre-existing material and not primary condensates.

The idea that CAIs are aggregates of pre-existing materials is further perpetuated by the ε^{50}Ti data. Figure 2.6 shows that the majority of the CAIs have values between ~6-10 epsilon units, with another cluster around 2 epsilon units. Still other CAIs that have values above or below the typical values, including 461_13 B, which has a significantly different ε^{50}Ti value. This indicates that there was likely heterogeneity in the disk in the precursor material from which the CAIs formed. The anomalously high ε^{50}Ti and low mass fractionation, δ^{49}Ti, for 461_13 B suggests that formation mechanism and isotope heterogeneity might be linked. We also see heterogeneity within CAIs as evidenced by L144A which displays a lower ε^{50}Ti in the mantle of the inclusion relative to the core. The varying compositions within and among CAIs represents echoes of larger scale heterogeneities in the precursor materials that has been dampened due to averaging. Although these heterogeneities are typically dampened due to averaging, with CAI 461 13 B we can see the echo of this heterogeneity reflecting isotopic heterogeneity in the molecular cloud.

Figure 2.10 (top) shows a probability density plot for the 106 spot analyses included in this study. The plot clearly shows some bimodality with the large peak around 8 epsilon units and a smaller peak closer to 2 epsilon. Below the plot of data from this study is a probability density plot of CAI data from the literature (Leya et al., 2009; Williams et al., 2017). In both cases, we see some bimodality and a concentration of values with higher or lower values around this concentration. Visually, there appears to be some averaging occurring.

We explore the idea of averaging in more depth by looking at hibonite grains. After corundum (which is rare in meteorites), hibonite is the second phase predicted to condense out of the solar nebula as the gas cools. The mineral has an ultrarefractory composition and substantial amounts of Ti. Occurrences of anomalous ^{50}Ti are frequently found in the hibonite phase.

Hibonite grains can be subdivided into two main types: Spinel-HIBonite spherules (SHIBs) or PLAty-hibonite Crystals (PLACs). The PLACs are considered condensates and the SHIBs are intergrowths. Figure 2.11 shows a binned histogram of ^{50}Ti anomalies in parts per thousand (per mil) for a collection of hibonite grains, including both SHIBs and PLACs. This data is from Liu et al. (2009). Again, we see that although the overall range of measured values is large, there is a Gaussian-like distribution.

Using this data, we create a probability density plot based on the analytical uncertainties for the hibonite grains (shown in gray). The measured values for ε^{50}Ti in hibonite grains extends beyond the axis of this plot, but is truncated here for visual clarity of the peaks. The plot shows that the peaks in the data are real. The probability plot for CAIs from Figure 2.12 is plotted overlying the hibonite data. The peaks for the CAI data mimic those of the hibonite grains, but are much more tightly clustered around the mean value. This can be explained if the CAIs are averages of their precursors (hibonites) in the solar disk.

To quantify this averaging effect, we look to the central limit theorem, which states

$$\sigma' = \sigma(N)^{-1/2}. \tag{2.16}$$

In this equation, σ is the standard deviation of the original data set. In the scenario evaluated here, this would be the standard deviation of the ε^{50}Ti values for the hibonite grains. The standard deviation of the newly grown grains, or CAIs, is represented by σ'. And N refers to the number of hibonite grains averaged to create the new grain or CAI. The central limit theorem has the effect of effacing any preexisting structure. Even if the initial population has a multimodal distribution, the averaging of this initial population will result in a distribution that is unimodal.

If we consider a CAI with a typical diameter of ~300 μm, it would require ~8000 hibonite grains, which are ~30 μm in size, to form the larger and later-forming CAI. As shown in

Figure 2.12, the ε^{50}Ti values in hibonite grains range from approximately -700 to ~1030 epsilon. The standard deviation of the hibonite data ~500 epsilon units is our σ in equation 2.16. We insert 500 in the equation: $\sigma_{CAIs} = 500\ (8000)^{-1/2}$. The central limit theorem predicts a standard deviation of 5.6 epsilon units for CAI ε^{50}Ti values. The standard deviation for the CAI data in this study is 9.6 epsilon units, which given the large spread in the initial data is quite comparable.

We can also consider what implications this data has at an even broader scale. What does it tell us about the molecular cloud precursors from which solar system solids eventually formed? Using the central limit theorem, we can back calculate the variability in presolar grains. A typical grain in the interstellar medium (ISM) is ~0.1 μm and it would take ~27 million presolar ISM grains to form one hibonite grain. We solve the central limit theorem for the precursor population in this case: $\sigma_{presolar} = 500\ (2.7 \times 10^7)^{1/2}$. The predicted standard deviation for presolar grains is 2.6×10^6 epsilon. To explore the effect that grain size has on our results, we can consider a larger presolar grain with a diameter of 0.3 μm. In this case, our resulting standard deviation for the presolar grain population is 5×10^5 epsilon. We can compare this predicted value to measured data. There have been a couple examples of presolar grains with extreme values. Jadhav et al. (2008) found a high density graphite grain with a value of ~3.3×10^5 epsilon units. A presolar oxide grain was found to have a value of ~10^6 epsilon units, though it is currently uncertain whether the measured anomaly is due to ^{50}Cr or ^{50}Ti (Nittler et al., 2017). Thus, there is evidence for large variability in presolar grains as predicted by the central limit theorem.

We also make similar observations by looking at ^{26}Al and excess ^{26}Mg (^{26}Mg*). ^{26}Al is a short-lived radionuclide which decays to ^{26}Mg with a half-life of ~0.73 million years. Importantly, it is believed to be a major heat source in the earlier solar system. Here, we will

explore the implications that the Al-Mg isotopic compositions have for the formation histories of early forming solids in the solar system.

In terms of the initial $^{26}Al/^{27}Al$ ratio, hibonite grains in CAIs display a bimodality with peaks around the canonical value and zero. SHIBs exhibiting a higher initial ratio close to the canonical value (5×10^{-5}) indicative of in-situ decay of ^{26}Al. Meanwhile, PLACs exhibiting ratios close to zero indicating an absence of in situ decay in the grains.

In order to remove the element of interpretation used to calculate the initial $^{26}Al/^{27}Al$ ratios, we assess the $^{26}Mg/^{24}Mg$ ratio of the hibonite grains. Figure 2.14 shows the $^{26}Mg/^{24}Mg$ ratios for the hibonite grains, in which there is still a clearly bimodal feature in the data. The central limit theorem designates that random sampling cannot preserve bimodality. As a result of this stipulation, the bimodal feature of the data must post-date sampling. The bump to the right of the main peak (entirely SHIBs) must be the result of post ^{26}Al homogenization decay.

Positive values for $^{26}Mg/^{24}Mg$ above the terrestrial value (reference material) implies ingrowth of ^{26}Al. Thus, from looking at Figure 2.13, we know that the PLACs have low radiogenic ^{26}Mg, displaying a lack of excess Mg and even in some cases, showing negative $^{26}Mg^*$ values (relative to terrestrial). The SHIBs carry the excess ^{26}Mg among hibonite grains. Furthermore, the SHIBs display a larger range of values for $^{26}Mg^*$. The SHIBs had live ^{26}Al, while the PLACs did not. It is believed that ^{26}Al was homogenously dispersed in the solar system and that this discrepancy is understood as PLACs forming subsequently to SHIBs, after ^{26}Al had already decayed. We argue against this requirement that PLACs never experienced live ^{26}Al and propose that it is due to differences in the initial Mg isotope heterogeneity.

The pattern displayed by PLACs and SHIBs is reminiscent of that exhibited by presolar grains (Figure 2.15). The presolar grain data also show a bimodality with a tightly clustered

group of data displaying low $^{27}Al/^{24}Mg$ and no radiogenic ^{26}Mg and a more dispersed group of data with higher and more variable $^{27}Al/^{24}Mg$ as well as a range of values for excess ^{26}Mg. If there were large variations in the initial Mg isotope compositions of the presolar material that formed hibonite grains, the decay product of ^{26}Al could potentially be obscured by this initial variability. In the case of post-grain formation homogenization of Mg, then decay that post-dates this homogenization would produce recognizable ^{26}Mg excesses.

Returning to the central limit theory and recalling that it takes ~27 million 0.1 μm presolar grain to make a single 30 μm hibonite grain, we calculate the expected dispersion in initial $\delta^{26}Mg$. The data for $\delta^{26}Mg$ in hibonite grains (Figure 2.14) have a standard deviation of ~5‰. Thus, $\sigma_{presolar} = 5(2.7 \times 10^7)^{1/2} = 2.6 \times 10^4$‰, which is a rather large spread in the expected values of precursor material. In terms of initial $^{26}Al/^{27}Al$, this is ~0.1‰. Is there evidence of this variability in an astrophysical setting? A model of star forming regions predicts variability of at least this magnitude (Young, 2016).

2.7 Conclusions

Many of the CAIs measured in this study exhibit isotopic compositions consistent with evaporation, this is particularly apparent with regards to the isotope compositions of Mg and Si, which are less refractory that Ca and Ti. Model-predicted correlations among stable isotope ratios for elements with similar condensation temperatures are rarely exhibited in CAIs, even for those CAIs that are considered condensates. Instead, these elements probably experienced different condensation histories and may have been inherited from different reservoirs. The isotopic compositions of CAIs and comparison of these compositions to our condensation model, suggest that CAIs are aggregates of pre-existing materials, rather than primary condensates.

We observe heterogeneity both within and among CAIs, these refractory inclusion compositions are echoes of larger heterogeneity in precursor material, which can be traced back to molecular cloud heterogeneity. This heterogeneity is not due to differences in timing and local source region. The magnitude of this heterogeneity is dampened due to the effect of averaging as grain growth progresses in the solar protoplanetary disk, this effect is quantified by the central limit theorem. We observe evidence of these larger, predicted variances in hibonite grains, presolar grains, and molecular clouds.

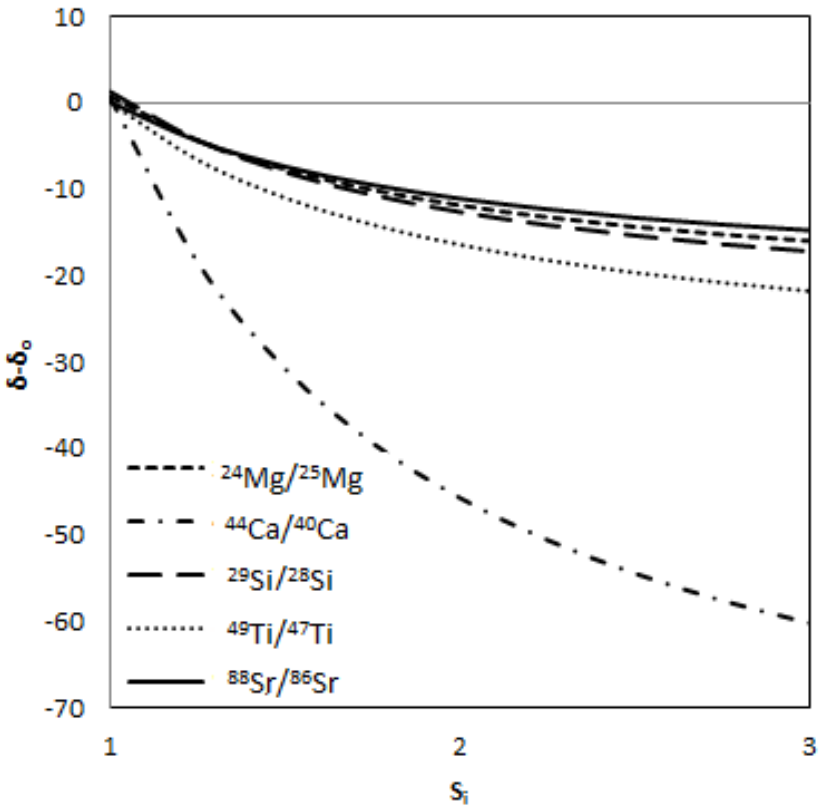

Figure 2.1. Calculated shifts in $\delta^{25}Mg$, $\delta^{44}Ca$, $\delta^{29}Si$, $\delta^{49}Ti$, and $\delta^{88}Sr$ from the initial composition with varying degrees of saturation.

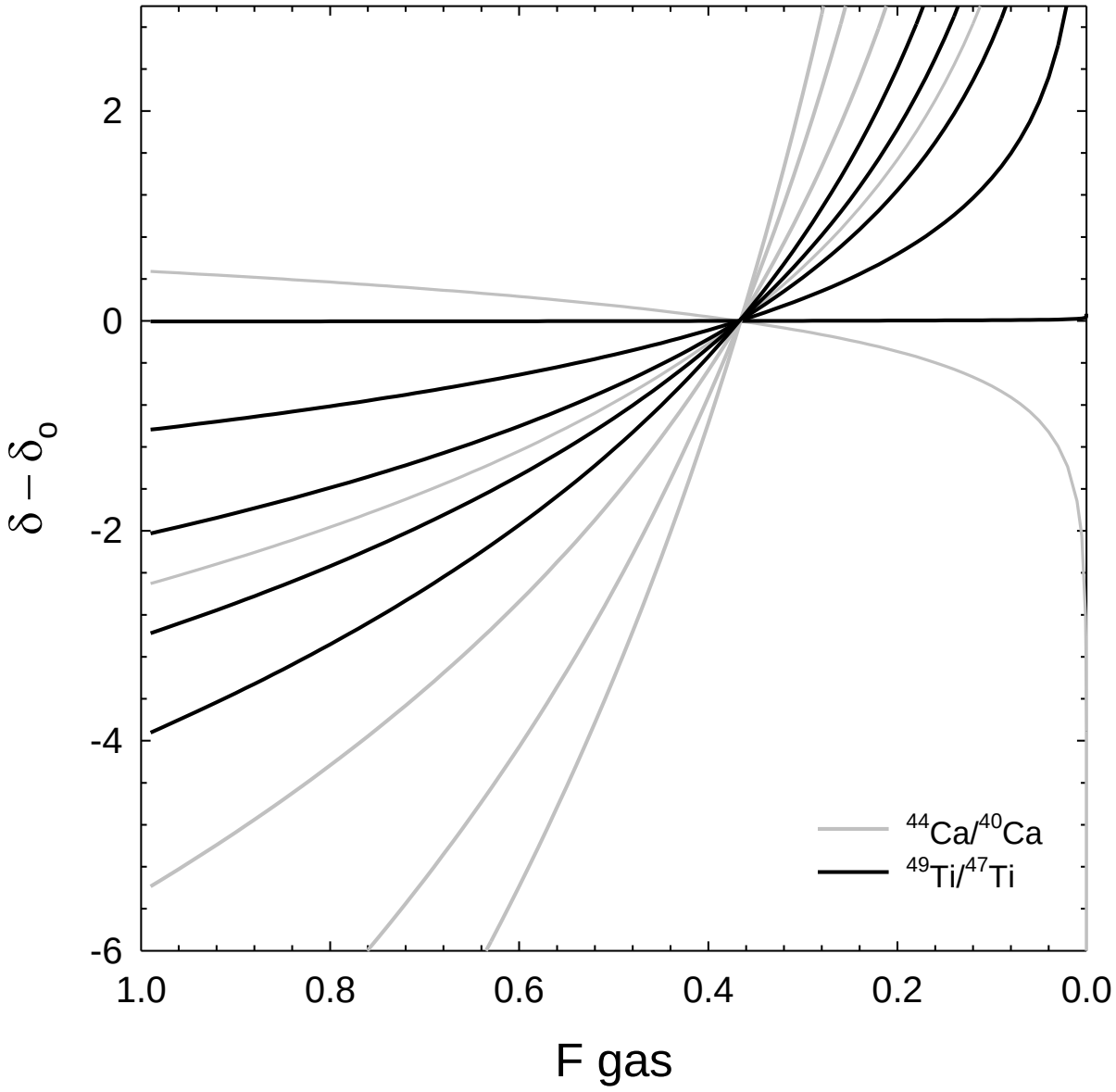

Figure 2.2 The complete model for condensation of Ca and Ti from a nebular gas. Calculated shifts in $\delta^{44}Ca$ and $\delta^{49}Ti$ with condensation as a function of saturation index S_i and fraction of Ca and Ti remaining in the gas phase. Each subsequent black and gray line represents an additional degree of undercooling, starting at equilibrium.

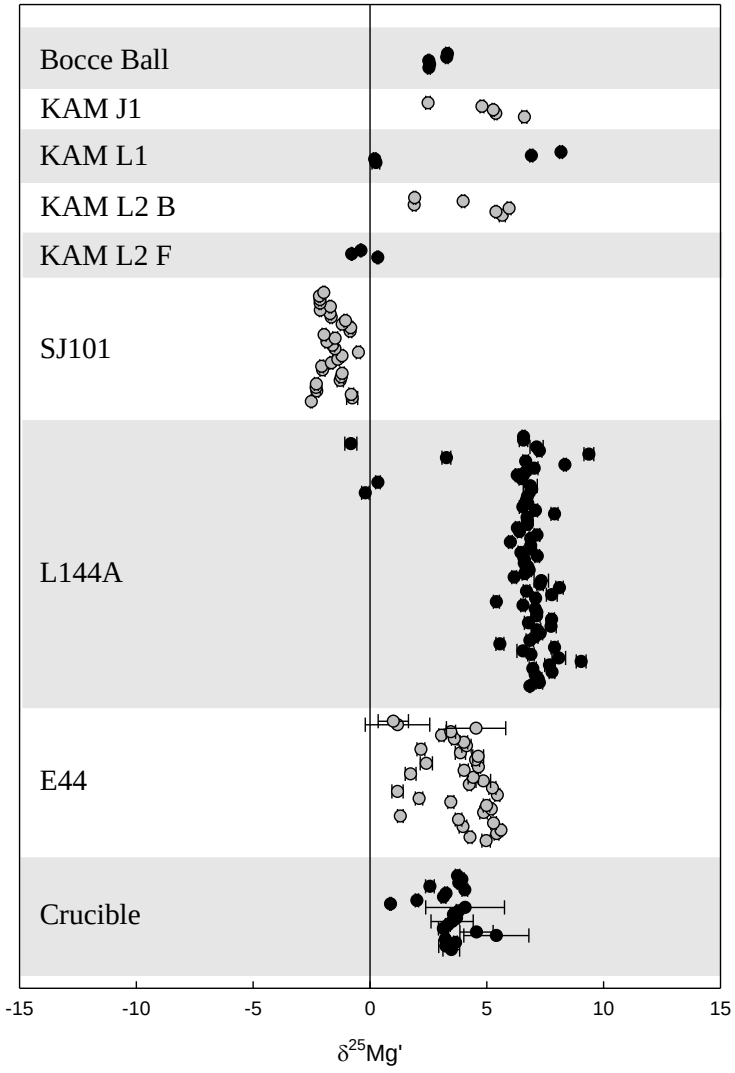

Figure 2.3. CAI δ^{25}Mg data. Each point represents an individual analysis. Values reported relative the Mg isotope standard DSM3. Error bars are 1 sigma.

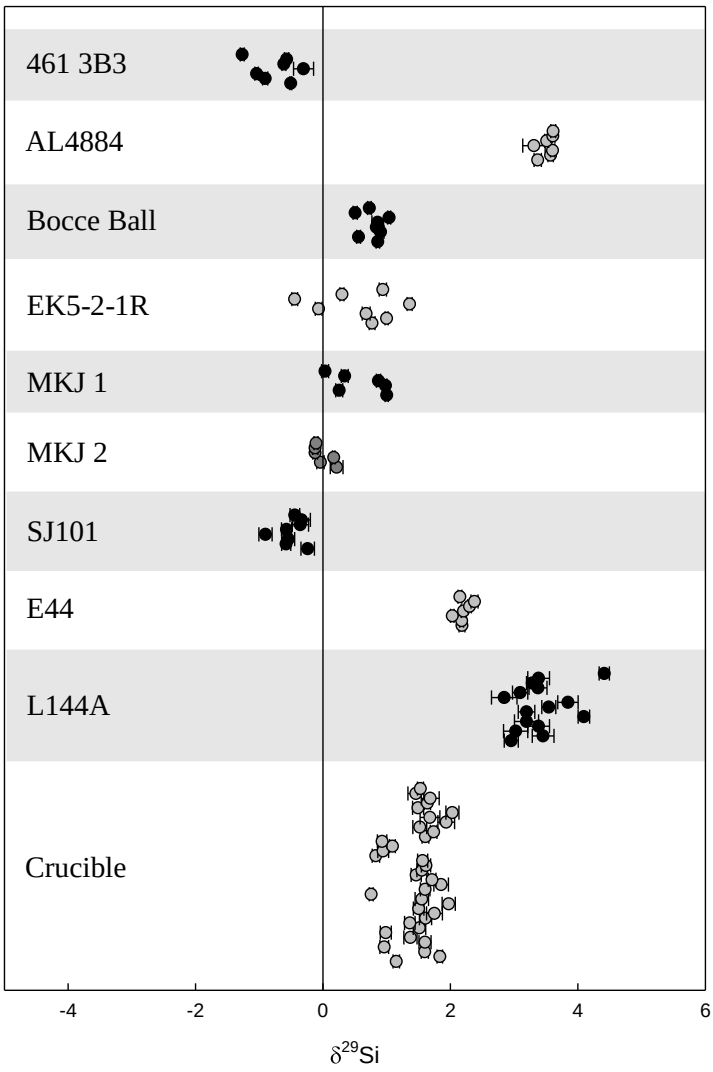

Figure 2.4. CAI δ^{28}Si data. Each point represents an individual analysis. Values reported relative the Si isotope standard NBS-28. Error bars are 1 sigma.

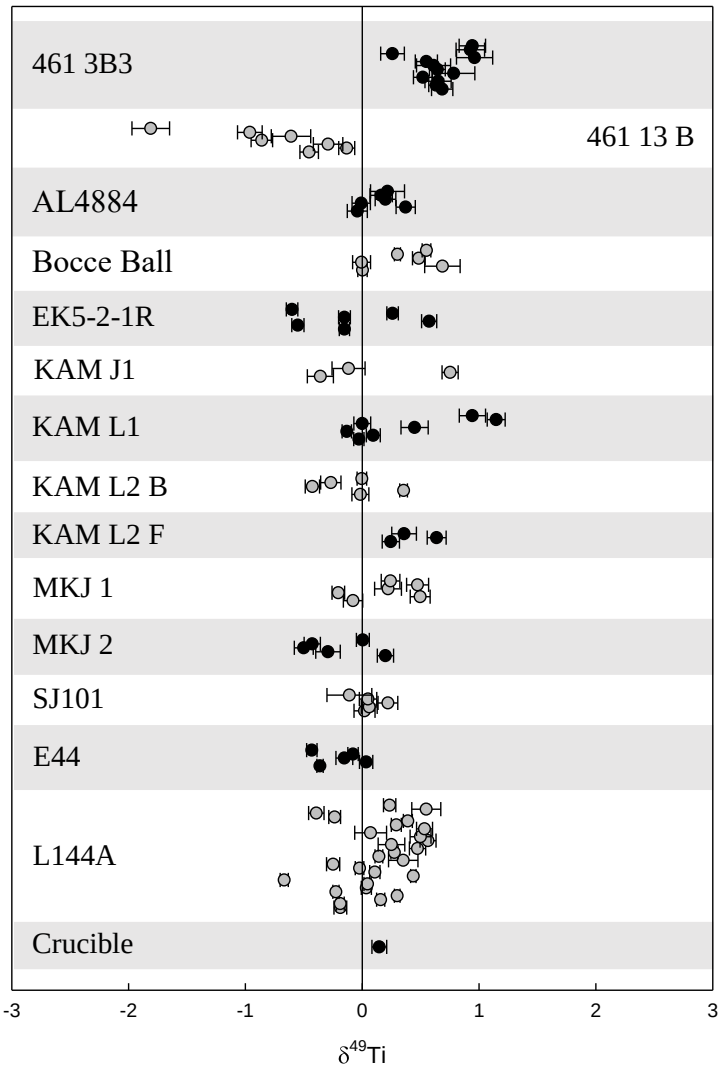

Figure 2.5. CAI δ^{49}Ti data. Each point represents an individual analysis. Values reported relative to our Ti standard USNM 83191 rutile. Error bars are 1 sigma.

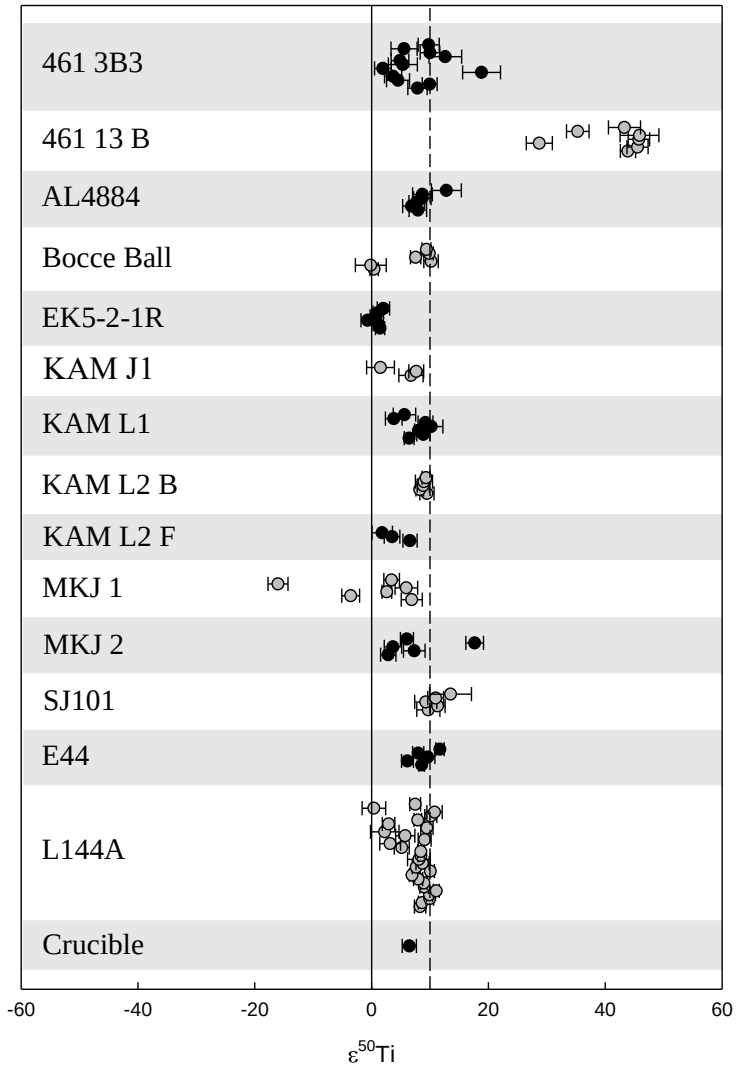

Figure 2.6. CAI ε^{50}Ti data. Each point represents an individual analysis. Values are relative to the terrestrial mass fractionation line. Error bars are 1 sigma.

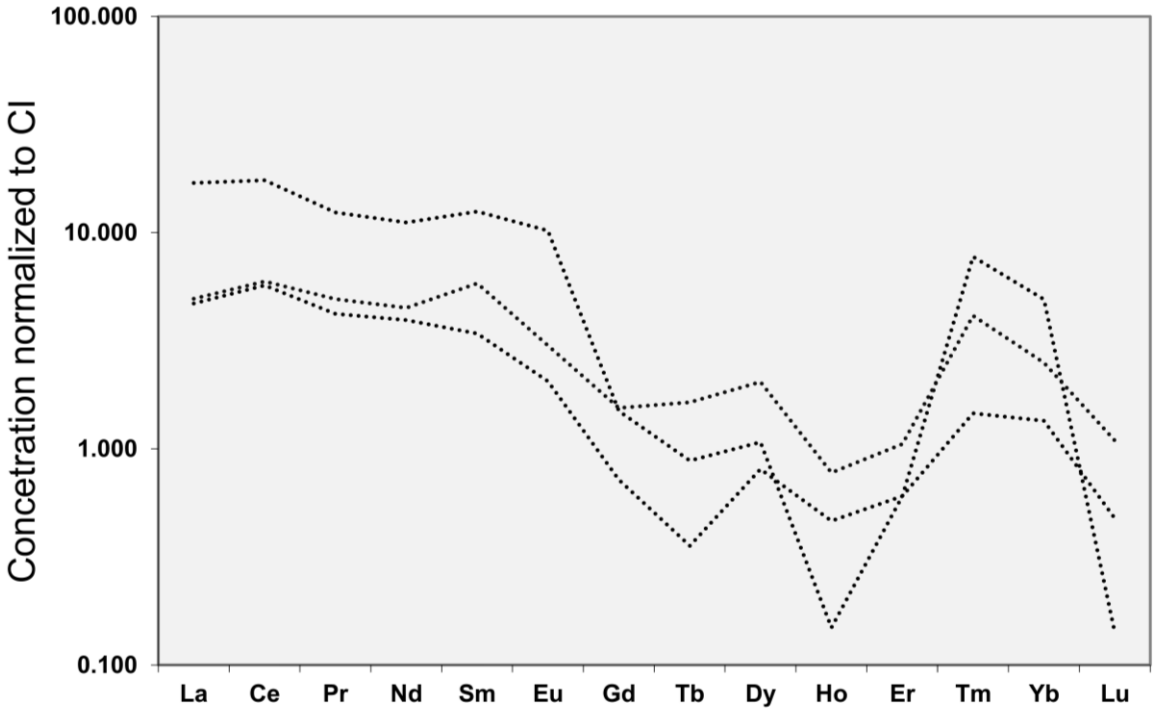

Figure 2.7. Group II REE pattern for Allende CAI 461 13 B.

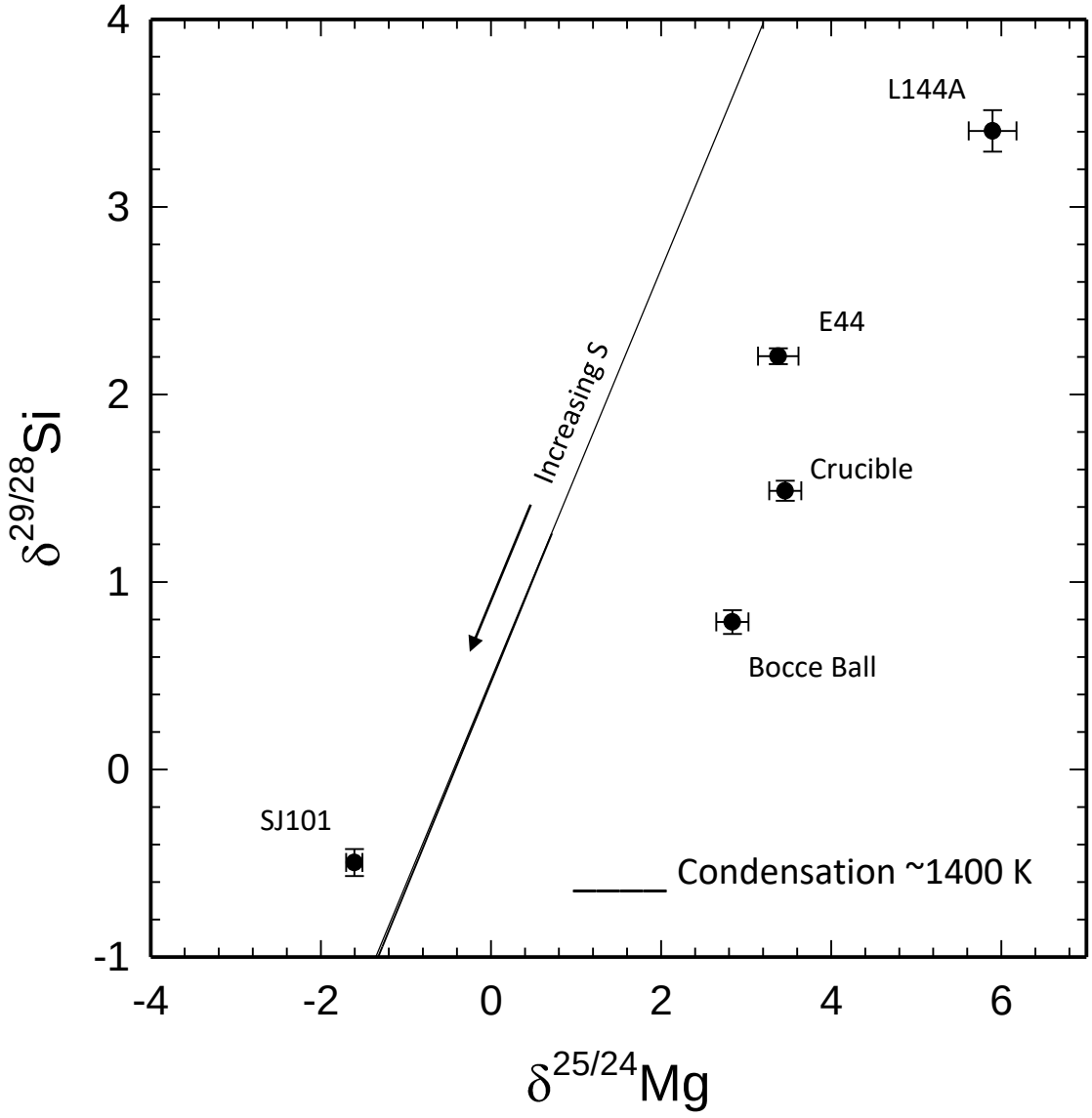

Figure 2.8. Condensation model for Si and Mg at 1400 K with average CAI values plotted.

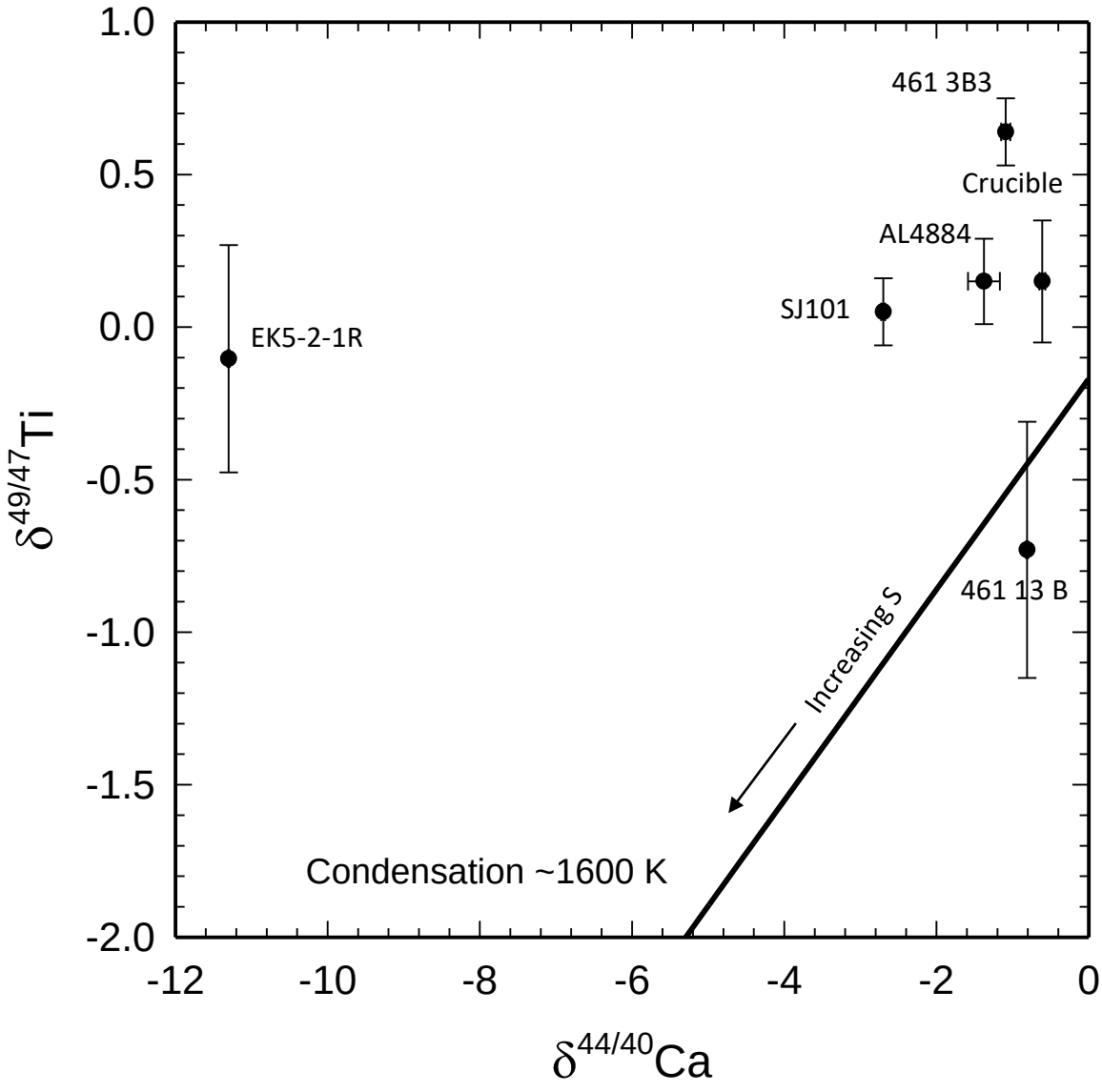

Figure 2.9. Condensation model for Ti and Ca at 1600 K with average CAI values plotted.

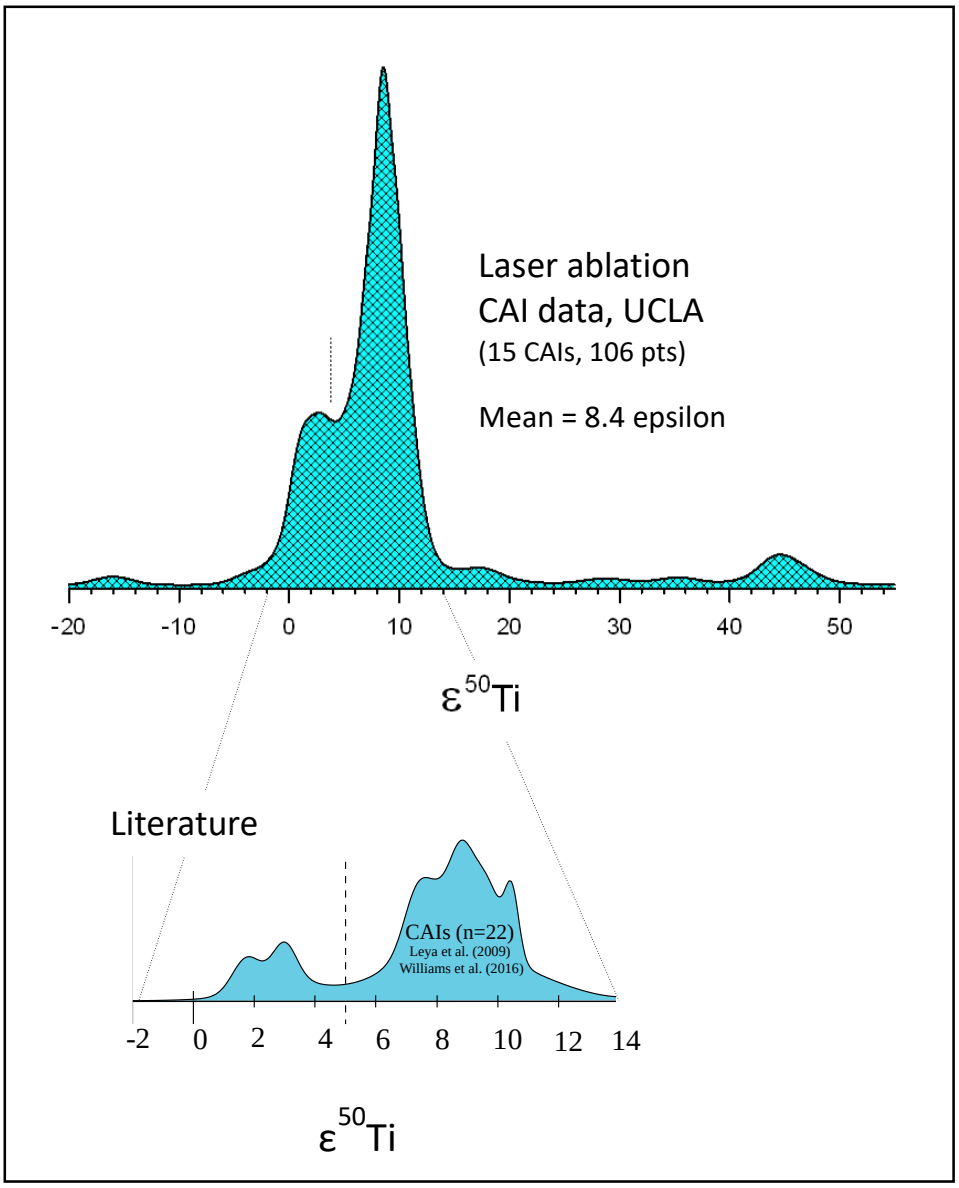

Figure 2.10. Probability density plots for ε^{50}Ti CAI data from this study (top) and from the literature (bottom). Both data sets display bimodal structure.

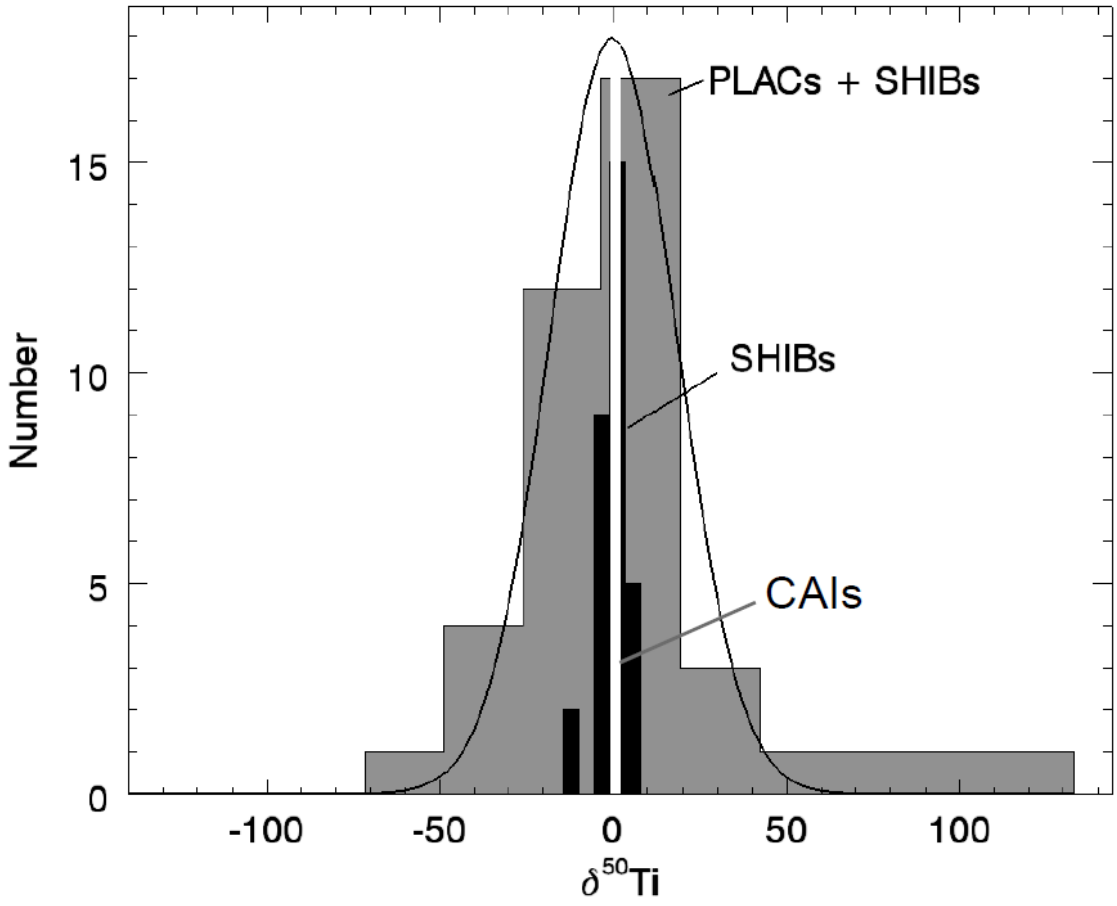

Figure 2.11. Histogram of δ^{50}Ti values for hibonite grains. The white line represents the average CAI value for δ^{50}Ti. The more tightly restrained values for CAIs relative to the variability seen in hibonite grains suggest the CAI composition reflects averaging. Hibonite data from Liu et al. (2009).

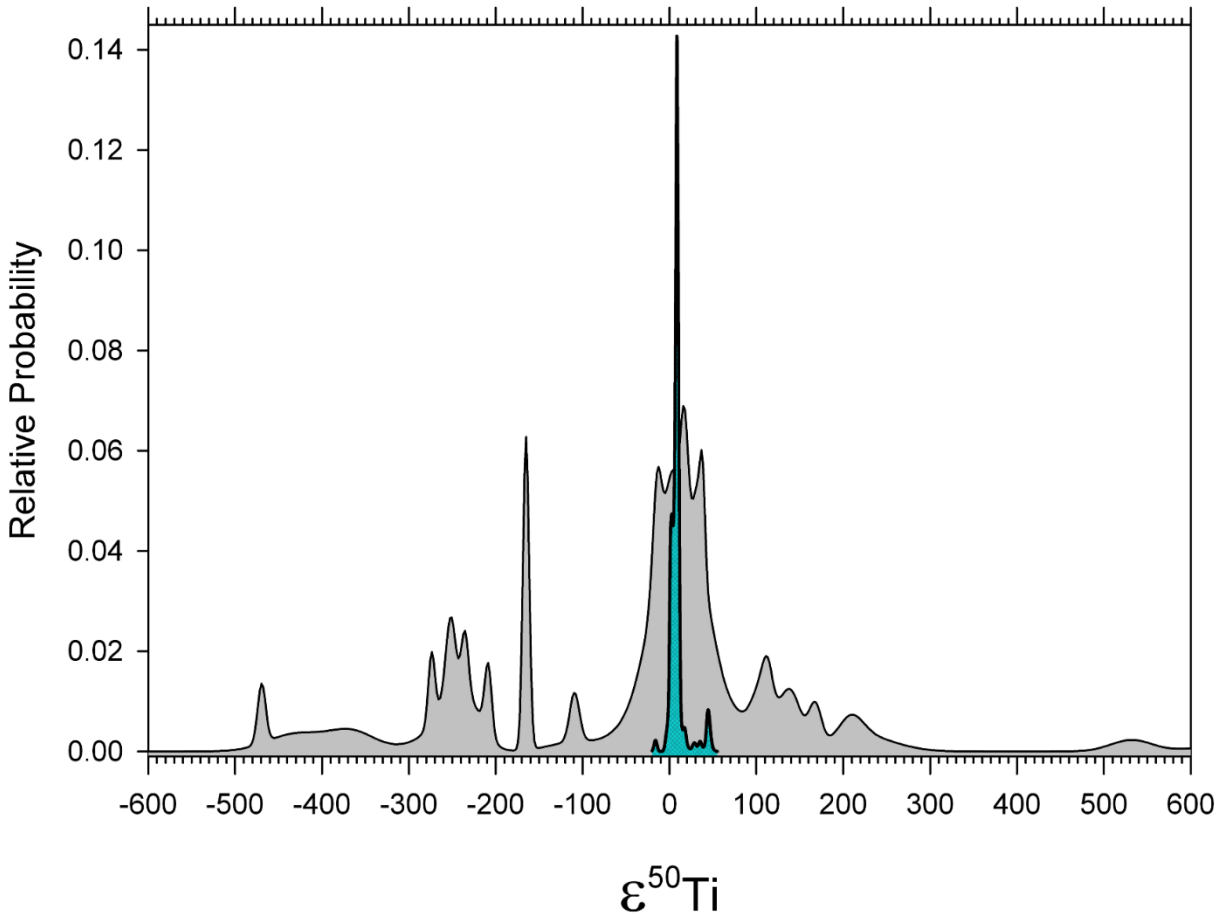

Figure 2.12. Probability density plots for hibonite grains (gray) and CAIs (teal). The CAI data echoes the peaks that are apparent in the hibonite data, which implies averaging.

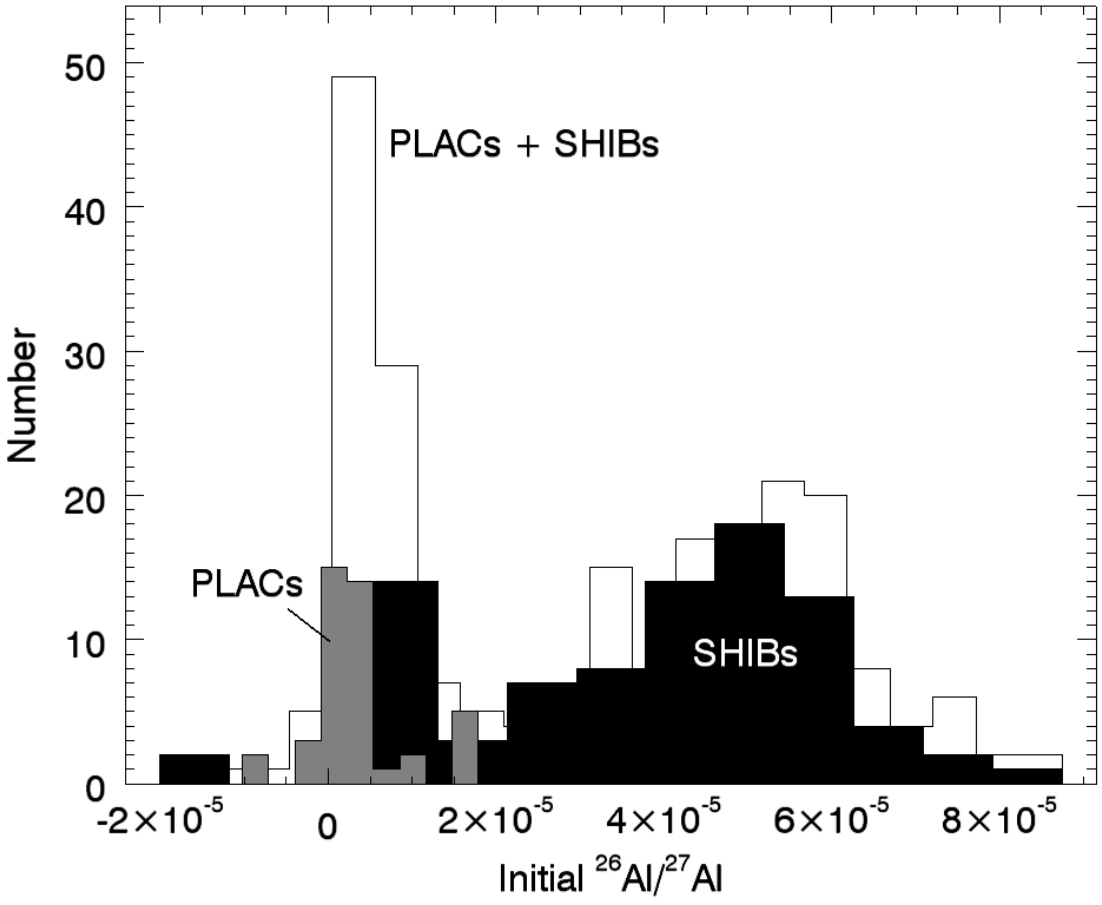

Figure 2.13. Histogram of inferred initial $^{26}Al/^{27}Al$ for hibonite grains. The diagram shows the bimodality of the data associated with the mineraology of the hibonite types. Values for PLACs have a smaller spread relative to SHIBs and display lower values, close to zero. Literature compilation.

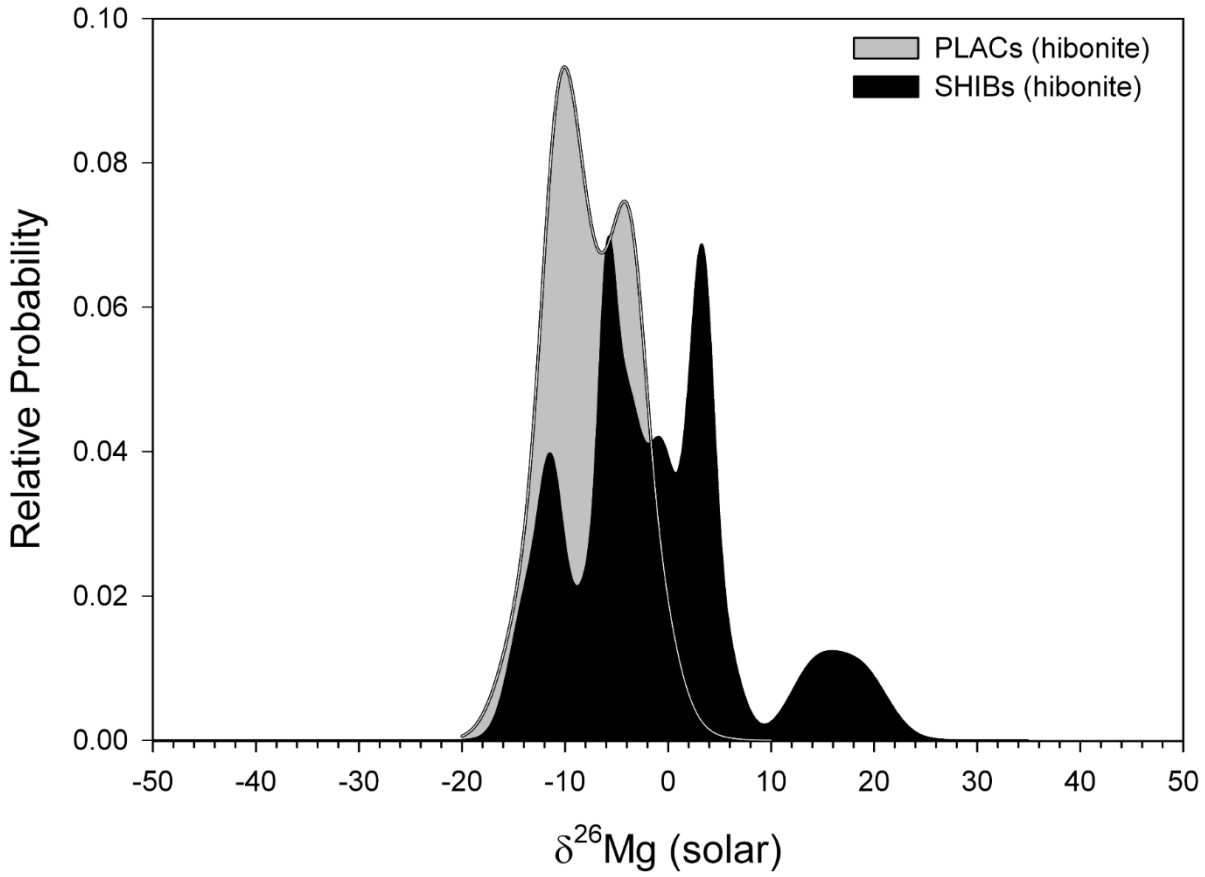

Figure 2.14. Probability density plot for the Mg isotopic composition of hibonite grains.

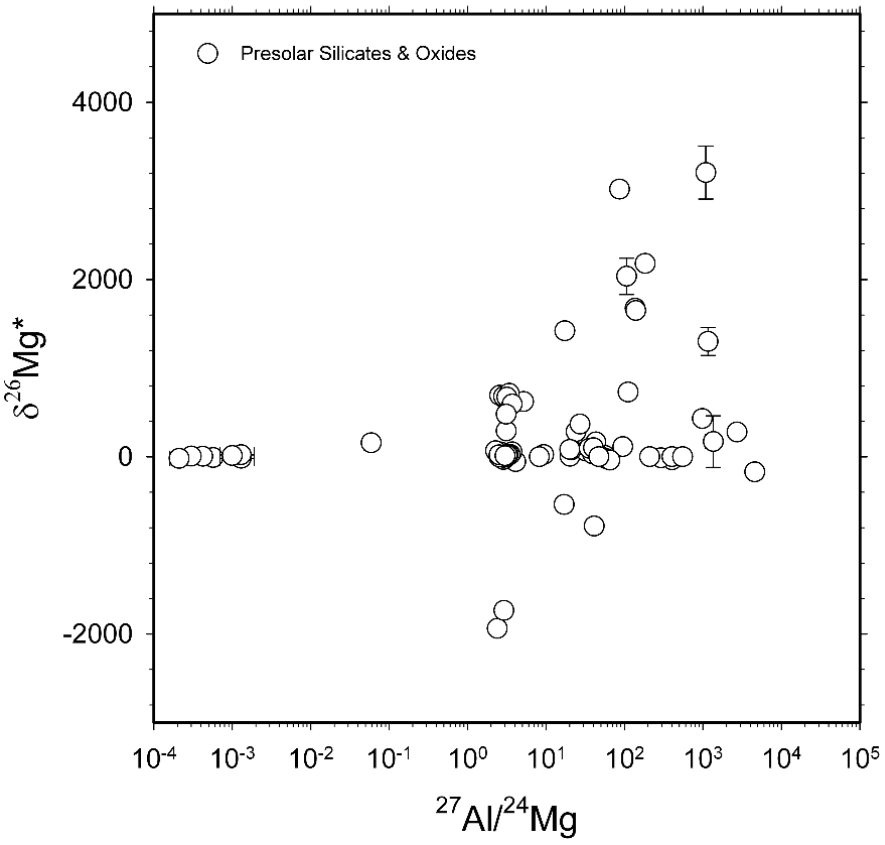

Figure 2.15. Presolar grain data from the Washington University database.

Table 2.1 Multi-element averages for isotopic compositions of CAIs

Object	$\delta^{25}Mg'$	1 SE	$\delta^{26}Mg'$	1 SE	$^{27}Al/^{24}Mg$	1 SE	$\delta^{26}Mg^*$	1 SE	$\delta^{28}Si$	1 SE	$\delta^{29}Si$	1 SE	$\delta^{44}Ca$	1 SE	$\delta^{49}TI$	1 SE	$\varepsilon^{50}Ti$	1 SE
461 3B3									-0.74	0.12	-1.43	0.26	-1.09	0.06	0.64	0.11	1.00	0.08
461 13 B													-0.81	0.02	-0.73	0.42	43.30	5.00
AL4884									3.51	0.04	6.80	0.13	-1.38	0.21	0.15	0.14	8.80	1.70
Bocce Ball	2.84	0.19	6.29	0.55	3.21	0.49	0.76	0.19	0.79	0.06	1.52	0.12			0.34	0.24	6.22	0.39
EK5-2-1R									0.57	0.21	0.99	0.43	-11.30	0.02	-0.10	0.37	6.20	1.70
KAM J1	5.08	0.40	11.76	0.65	6.09	0.73	1.92	0.17							0.09	0.67	5.30	0.40
KAM L1	3.88	2.13	10.21	4.10	8.24	0.73	2.71	0.44							0.25	0.39	6.97	0.18
KAM L2 B	4.13	0.76	9.91	1.48	5.62	0.76	2.00	0.29							-0.07	0.27	8.97	0.04
KAM L1 F	-0.28	0.33	-0.33	0.63	2.02	0.53	0.21	0.07							0.41	0.23	3.97	0.28
MKJ 1									0.58	0.17	0.90	0.35			0.19	0.23	-0.12	0.35
MKJ 2									0.00	0.06	-0.12	0.12			-0.15	0.24	7.50	0.22
SJ101	-1.61	0.10	-2.95	0.20	2.18	0.17	0.14	0.05	-0.50	0.07	-1.34	0.10	-2.70	0.03	0.05	0.11	11.00	1.50
E44	3.38	0.24	13.38	2.49	19.77	8.42	6.39	2.53	2.20	0.04	4.02	0.08			-0.20	0.17	8.81	0.09
L144A	5.90	0.28	13.18	0.60	4.80	0.28	1.92	0.12	3.40	0.11					0.14	0.12	7.51	1.30
Crucible	3.46	0.19	9.21	1.12	9.38	4.06	2.48	1.00	1.49	0.05	2.81	0.11	-0.61	0.04	0.15	0.20	6.50	2.40

Mg values relative to DSM3, Mg analyses for E44 and L144A from Young et al. (2005)

Si Values relative to NBS-28, Si analysis for L144A from Shahar and Young (2007)

Ca values relative to chondrite, Ca analysis for SJ101 from Huang et al. (2012), remaining Ca analyses from Simon et al. (2017)

Appendix B: CAI Data Tables

Table B1. Magnesium isotope measurements of CAIs
Values relative to DSM3

Allende Bocce Ball

$\delta^{25}Mg'$	1 SE	$\delta^{26}Mg'$	1 SE	$^{27}Al/^{24}Mg$	1 SE	$\delta^{26}Mg^*$	1 SE
2.52	0.06	5.40	0.06	2.46	0.00	0.49	0.09
2.55	0.12	5.67	0.05	2.43	0.01	0.71	0.24
2.51	0.03	5.13	0.05	2.40	0.00	0.24	0.08
3.29	0.06	7.62	0.05	3.95	0.02	1.23	0.12
3.31	0.08	7.61	0.07	4.80	0.03	1.16	0.15

Allende KAM J1

$\delta^{25}Mg'$	1 SE	$\delta^{26}Mg'$	1 SE	$^{27}Al/^{24}Mg$	1 SE	$\delta^{26}Mg^*$	1 SE
6.61	0.11	14.85	0.10	7.31	0.16	2.00	0.23
5.38	0.06	12.09	0.05	4.69	0.02	1.62	0.08
5.28	0.05	11.97	0.05	5.51	0.01	1.71	0.11
4.79	0.08	10.78	0.14	3.88	0.02	1.46	0.10
2.49	0.10	7.36	0.15	8.32	0.06	2.52	0.13
5.80	0.17	13.09	0.15	4.40	0.02	1.81	0.44
5.93	0.05	12.90	0.04	3.97	0.02	1.36	0.11
3.48	0.08	10.06	0.05	10.35	0.30	3.30	0.13
4.90	0.09	11.47	0.07	8.33	0.06	1.93	0.20
6.10	0.05	13.07	0.06	4.18	0.02	1.20	0.09

Allende KAM L1

$\delta^{25}Mg'$	1 SE	$\delta^{26}Mg'$	1 SE	$^{27}Al/^{24}Mg$	1 SE	$\delta^{26}Mg^*$	1 SE
0.25	0.16	4.25	0.27	9.66	0.14	3.75	0.54
0.20	0.05	2.12	0.13	6.31	0.07	1.73	0.10
6.91	0.06	16.31	0.08	9.03	0.07	2.86	0.11
8.17	0.07	18.17	0.07	7.97	0.09	2.27	0.11

Allende KAM L2 B

$\delta^{25}Mg'$	1 SE	$\delta^{26}Mg'$	1 SE	$^{27}Al/^{24}Mg$	1 SE	$\delta^{26}Mg^*$	1 SE
5.66	0.13	13.52	0.12	5.20	0.01	2.51	0.35
5.39	0.05	12.31	0.06	5.57	0.03	1.82	0.10
5.95	0.08	12.58	0.04	4.08	0.01	1.50	0.14
1.89	0.08	6.52	0.18	9.25	0.20	2.84	0.12

3.99	0.07	9.98	0.05	5.19	0.03	2.23	0.12
1.91	0.05	4.57	0.05	4.43	0.09	0.86	0.07

Allende KAM L2 F

$\delta^{25}Mg'$	1 SE	$\delta^{26}Mg'$	1 SE	$^{27}Al/^{24}Mg$	1 SE	$\delta^{26}Mg^*$	1 SE
0.34	0.04	0.79	0.02	2.26	0.10	0.14	0.08
-0.78	0.02	-1.39	0.03	1.01	0.04	0.14	0.04
-0.39	0.03	-0.39	0.04	2.80	0.03	0.36	0.05

Allende SJ101

$\delta^{25}Mg'$	1 SE	$\delta^{26}Mg'$	1 SE	$^{27}Al/^{24}Mg$	1 SE	$\delta^{26}Mg^*$	1 SE
-2.51	0.04	-4.15	0.03	0.41	0.00	-0.14	0.07
-0.76	0.24	-0.69	0.21	3.55	0.05	0.79	0.45
-0.80	0.10	-1.46	0.06	1.97	0.03	0.09	0.18
-2.28	0.08	-3.60	0.18	2.95	0.03	0.83	0.20
-2.31	0.18	-4.29	0.10	2.23	0.01	0.20	0.36
-2.30	0.08	-4.36	0.09	1.68	0.01	0.11	0.15
-1.27	0.14	-2.50	0.13	3.19	0.04	-0.02	0.19
-1.22	0.10	-1.80	0.08	3.49	0.05	0.58	0.20
-1.19	0.09	-1.89	0.06	2.66	0.01	0.43	0.15
-2.03	0.11	-3.48	0.09	2.30	0.02	0.47	0.15
-2.07	0.08	-3.92	0.08	2.16	0.01	0.10	0.14
-1.65	0.07	-3.43	0.14	1.81	0.04	-0.22	0.13
-1.38	0.07	-2.86	0.11	2.90	0.03	-0.17	0.18
-1.20	0.07	-2.51	0.10	2.23	0.01	-0.17	0.07
-0.50	0.09	-0.87	0.07	3.71	0.07	0.09	0.20
-1.50	0.10	-2.58	0.09	3.06	0.03	0.33	0.15
-1.61	0.10	-2.76	0.09	2.50	0.05	0.37	0.20
-1.84	0.08	-3.66	0.14	1.86	0.01	-0.08	0.12
-1.49	0.11	-2.89	0.11	2.88	0.16	0.01	0.19
-1.96	0.09	-3.74	0.13	1.65	0.03	0.08	0.09
-0.85	0.07	-1.81	0.10	2.29	0.09	-0.16	0.07
-0.83	0.09	-0.85	0.07	4.08	0.08	0.76	0.19
-1.19	0.08	-2.36	0.11	2.01	0.01	-0.03	0.12
-1.04	0.07	-1.54	0.11	3.20	0.03	0.49	0.06
-1.66	0.06	-3.13	0.06	1.16	0.04	0.10	0.14
-1.71	0.06	-3.28	0.12	1.47	0.04	0.04	0.11
-2.12	0.05	-4.03	0.03	0.80	0.03	0.10	0.09
-1.70	0.05	-3.51	0.10	1.16	0.02	-0.21	0.09
-2.13	0.05	-4.15	0.12	1.26	0.02	0.00	0.16

-2.14	0.06	-4.13	0.07	1.76	0.04	0.04	0.05
-2.16	0.04	-4.31	0.07	0.38	0.01	-0.11	0.04
-1.97	0.04	-3.99	0.04	0.98	0.02	-0.15	0.08

North West Africa 2364 Crucible

$\delta^{25}Mg'$	1 SE	$\delta^{26}Mg'$	1 SE	$^{27}Al/^{24}Mg$	1 SE	$\delta^{26}Mg^*$	1 SE
3.48	0.36	8.09	0.14	3.88	0.04	1.32	0.71
3.25	0.31	6.51	0.21	4.36	0.04	0.19	0.65
3.66	0.07	8.29	0.09	2.43	0.02	1.16	0.16
3.22	0.14	6.28	0.26	2.08	0.01	0.01	0.16
5.41	1.39	12.33	1.58	3.90	0.07	1.81	1.43
4.56	0.71	10.96	1.06	3.98	0.07	2.09	1.66
3.14	0.21	8.14	0.28	4.40	0.06	2.02	0.54
3.33	0.10	8.01	0.07	4.33	0.02	1.52	0.17
3.52	0.90	24.74	1.30	71.45	7.75	17.89	2.64
3.70	0.11	8.20	0.26	4.18	0.06	0.99	0.18
3.57	0.14	8.13	0.22	3.46	0.04	1.19	0.16
3.80	0.11	7.56	0.17	2.19	0.05	0.16	0.15
4.07	1.69	23.57	2.55	64.59	6.93	15.65	5.14
0.88	0.04	1.78	0.05	1.95	0.02	0.07	0.09
2.01	0.07	4.25	0.12	2.16	0.03	0.34	0.14
3.15	0.10	7.09	0.14	3.67	0.02	0.96	0.19
3.26	0.06	7.25	0.06	3.62	0.02	0.92	0.10
4.06	0.12	9.39	0.07	4.00	0.03	1.50	0.26
2.57	0.19	6.76	0.19	4.52	0.05	1.77	0.22
3.80	0.07	8.34	0.16	3.89	0.05	0.95	0.16
3.93	0.10	8.09	0.10	2.84	0.01	0.44	0.21
3.75	0.10	8.81	0.23	4.40	0.06	1.51	0.20

$\delta^{i}Mg' = 1000 \ln((^{i}Mg/^{24}Mg)_{sample}/(^{i}Mg/^{24}Mg)_{standard})$; radiogenic $^{26}Mg = \delta^{26}Mg^*$;
$\delta^{26}Mg^* = \delta^{26}Mg' - \delta^{25}Mg'/0.514$.

Table B2. Silicon isotope measurements in CAIs

Values relative to NBS28

Allende 461 3B3			
$\delta^{28}Si$	1 SE	$\delta^{29}Si$	1 SE
-0.51	0.01	-1.05	0.02
-0.91	0.04	-1.79	0.03
-1.04	0.03	-2.23	0.04
-0.31	0.16	-0.19	0.24
-0.61	0.03	-1.13	0.02
-0.57	0.03	-1.30	0.05
-1.27	0.03	-2.32	0.03

Allende Al4884			
$\delta^{28}Si$	1 SE	$\delta^{29}Si$	1 SE
3.37	0.06	6.46	0.11
3.57	0.04	7.06	0.05
3.60	0.03	7.02	0.03
3.31	0.18	6.09	0.20
3.51	0.03	6.78	0.04
3.61	0.03	6.88	0.03
3.61	0.04	7.31	0.05

Allende Bocce Ball			
$\delta^{28}Si$	1 SE	$\delta^{29}Si$	1 SE
0.86	0.03	1.55	0.04
0.56	0.03	1.22	0.05
0.90	0.05	1.93	0.07
0.84	0.03	1.58	0.05
0.86	0.09	1.75	0.07
1.04	0.02	1.90	0.04
0.51	0.03	0.96	0.07
0.73	0.03	1.30	0.08

Allende EK5-2-1R			
$\delta^{28}Si$	1 SE	$\delta^{29}Si$	1 SE
0.77	0.05	1.31	0.06
1.00	0.02	1.91	0.06
0.68	0.06	1.08	0.13
-0.07	0.05	-0.42	0.06
1.36	0.04	2.50	0.03
-0.44	0.04	-0.90	0.04
0.30	0.03	0.39	0.06

0.94	0.06	2.03	0.10

Allende MKJ 1

$\delta^{28}Si$	1 SE	$\delta^{29}Si$	1 SE
1.00	0.02	1.64	0.05
0.25	0.06	0.44	0.03
0.98	0.02	1.79	0.05
0.87	0.03	1.45	0.04
0.34	0.05	0.51	0.05
0.03	0.05	-0.42	0.06

Allende MKJ 2

$\delta^{28}Si$	1 SE	$\delta^{29}Si$	1 SE
0.21	0.10	0.39	0.10
-0.04	0.06	-0.20	0.04
0.17	0.02	0.07	0.02
-0.12	0.04	-0.38	0.02
-0.12	0.04	-0.30	0.04
-0.11	0.03	-0.33	0.02

Allende SJ101

$\delta^{28}Si$	1 SE	$\delta^{29}Si$	1 SE
-0.24	0.11	-0.83	0.14
-0.58	0.07	-1.55	0.06
-0.54	0.10	-1.67	0.12
-0.90	0.10	-1.49	0.09
-0.57	0.08	-1.24	0.08
-0.36	0.13	-1.09	0.07
-0.34	0.14	-1.59	0.14
-0.44	0.07	-1.22	0.09

Efremovka E44

$\delta^{28}Si$	1 SE	$\delta^{29}Si$	1 SE
2.18	0.05	4.18	0.06
2.18	0.03	4.00	0.06
2.03	0.03	3.63	0.06
2.21	0.04	3.92	0.04
2.30	0.03	4.21	0.04
2.38	0.06	4.26	0.05
2.15	0.03	3.96	0.03

NWA 2364 Crucible			
$\delta^{28}Si$	1 SE	$\delta^{29}Si$	1 SE
1.15	0.05	1.88	0.13
1.83	0.04	3.09	0.09
1.60	0.06	3.00	0.11
0.96	0.07	1.82	0.08
1.60	0.10	3.14	0.10
1.37	0.10	2.43	0.09
0.99	0.09	1.78	0.06
1.51	0.10	2.95	0.10
1.36	0.08	2.79	0.07
1.61	0.10	2.87	0.09
1.75	0.12	3.14	0.09
1.50	0.08	2.98	0.15
1.97	0.10	3.54	0.07
1.55	0.11	2.94	0.12
0.76	0.03	1.77	0.08
1.60	0.08	3.04	0.08
1.85	0.11	2.82	0.11
1.71	0.06	3.63	0.03
1.46	0.08	3.06	0.10
1.55	0.08	3.00	0.14
1.62	0.07	3.56	0.19
1.56	0.08	3.12	0.09
0.83	0.06	1.65	0.08
0.94	0.08	1.82	0.06
1.09	0.05	1.99	0.11
0.93	0.07	1.38	0.06
1.61	0.05	3.11	0.09
1.74	0.05	3.40	0.14
1.52	0.11	2.37	0.08
1.93	0.13	3.88	0.14
1.68	0.15	3.20	0.11
2.03	0.10	4.40	0.18
1.49	0.09	2.74	0.09
1.64	0.05	3.01	0.11
1.68	0.14	3.01	0.14
1.46	0.13	2.35	0.11
1.53	0.05	3.35	0.08

Table B3. Titanium isotope data for CAIs

Values reported relative to USNM 83191 Rutile (terrestrial)

Allende 461 3B3			
δ^{49}Ti	**1 SE**	**ε^{50}Ti**	**1 SE**
0.62	0.10	4.39	1.66
0.68	0.09	7.85	1.65
0.63	0.06	9.94	1.27
0.65	0.11	4.52	1.97
0.52	0.08	3.68	1.47
0.78	0.18	18.83	3.24
0.64	0.07	1.94	1.43
0.61	0.15	5.34	2.48
0.55	0.10	4.86	1.51
0.96	0.15	12.61	2.80
0.26	0.10	10.00	1.68
0.93	0.12	5.56	2.23
0.94	0.11	9.78	1.80

Allende 461 13 B			
δ^{49}Ti	**1 SE**	**ε^{50}Ti**	**1 SE**
-0.45	0.08	43.89	1.30
-0.13	0.07	45.53	1.81
-0.29	0.13	28.71	2.23
-0.86	0.09	45.76	1.84
-0.61	0.17	45.87	3.33
-0.96	0.11	35.30	1.94
-1.81	0.16	43.29	2.75

Allende AL4884			
δ^{49}Ti	**1 SE**	**ε^{50}Ti**	**1 SE**
-0.04	0.09	7.92	1.49
0.37	0.08	6.83	1.52
-0.01	0.08	7.72	1.33
0.20	0.09	8.68	1.50
0.16	0.10	8.71	1.70
0.22	0.15	12.81	2.56

Allende Bocce Ball			
δ^{49}Ti	**1 SE**	**ε^{50}Ti**	**1 SE**
0.00	0.04	0.45	0.72

0.69	0.15	-0.14	2.64
-0.01	0.08	10.18	1.24
0.48	0.05	7.54	0.87
0.30	0.03	9.91	0.64
0.55	0.04	9.40	0.78

Allende EK5-2-1R

δ^{49}Ti	1 SE	ε^{50}Ti	1 SE
-0.15	0.04	1.45	0.79
-0.55	0.05	1.15	0.87
0.57	0.06	-0.69	1.12
-0.15	0.05	0.65	0.91
0.26	0.05	1.16	0.89
-0.60	0.05	2.02	1.06

Allende KAM J1

δ^{49}Ti	1 SE	ε^{50}Ti	1 SE
-0.36	0.11	6.75	2.07
0.75	0.07	7.64	1.27
-0.12	0.14	1.52	2.39

Allende KAM L1

δ^{49}Ti	1 SE	ε^{50}Ti	1 SE
-0.03	0.04	6.42	0.83
0.09	0.06	8.87	1.12
-0.13	0.04	8.02	0.68
0.45	0.12	10.22	1.99
0.00	0.07	9.23	1.27
1.15	0.08	3.79	1.42
0.94	0.11	5.63	1.91

Allende KAM L2 B

δ^{49}Ti	1 SE	ε^{50}Ti	1 SE
-0.02	0.07	9.48	1.21
0.35	0.03	8.25	0.65
-0.43	0.06	8.84	1.02
-0.27	0.09	8.97	1.46
0.00	0.04	9.32	0.66

Allende KAM L2 F

δ^{49}Ti	1 SE	ε^{50}Ti	1 SE
0.24	0.07	6.57	1.21

0.64	0.08	3.51	1.34
0.36	0.11	1.82	1.75

Allende MKJ 1

δ^{49}Ti	1 SE	ε^{50}Ti	1 SE
-0.08	0.08	6.88	1.80
0.50	0.08	-3.57	1.52
-0.20	0.05	2.62	0.82
0.22	0.11	5.95	1.93
0.47	0.09	-16.02	1.70
0.24	0.08	3.43	1.34

Allende MKJ 2

δ^{49}Ti	1 SE	ε^{50}Ti	1 SE
0.20	0.07	2.85	1.31
-0.29	0.10	7.30	1.85
-0.50	0.08	3.66	1.49
-0.43	0.07	17.65	1.51
0.01	0.06	6.05	1.11

Allende SJ101

δ^{49}Ti	1 SE	ε^{50}Ti	1 SE
0.02	0.09	9.71	1.98
0.06	0.07	11.32	1.26
0.22	0.08	9.27	1.89
0.05	0.07	10.97	1.35
-0.11	0.19	13.52	3.59

Efremovka E44

δ^{49}Ti	1 SE	ε^{50}Ti	1 SE
-0.36	0.03	8.57	0.47
0.03	0.06	6.14	1.01
-0.15	0.07	9.64	1.20
-0.08	0.04	7.98	0.96
-0.43	0.04	11.71	0.71

Leoville L144A

δ^{49}Ti	1 SE	ε^{50}Ti	1 SE
-0.19	0.05	8.31	0.97
-0.19	0.03	8.65	0.66
0.16	0.04	9.97	0.65
0.30	0.02	9.92	0.51

-0.22	0.03	11.07	0.50
0.04	0.04	9.01	0.74
0.05	0.03	8.96	0.54
-0.67	0.03	7.97	0.78
0.44	0.02	6.93	0.46
0.11	0.04	10.06	0.70
-0.02	0.04	7.65	0.69
-0.25	0.06	8.73	1.13
0.35	0.13	8.10	1.95
0.14	0.03	8.47	0.51
0.28	0.03	8.44	0.56
0.47	0.07	5.16	1.28
0.25	0.11	3.18	1.77
0.56	0.07	9.08	1.12
0.50	0.09	5.76	1.64
0.07	0.14	2.26	2.43
0.53	0.07	9.46	1.06
0.29	0.04	2.91	1.07
0.39	0.04	7.91	0.65
-0.24	0.05	10.15	1.03
-0.39	0.07	10.78	1.30
0.55	0.12	0.40	2.02
0.23	0.05	7.47	0.93

NWA 2364 Crucible

δ^{49}Ti	1 SE	ε^{50}Ti	1 SE
0.15	0.06	6.46	1.21

Appendix C: Additional Figures

C1: $^{27}Al/^{24}Mg$ vs. $\delta^{26}Mg^*$ for CAI data collected as part of this thesis. The dashed line represents a supraconical $(^{27}Al/^{24}Mg)_o$ of 7 x 10^{-5}, while the solid line directly below the dashed line represent the canonical value of $(^{27}Al/^{24}Mg)_o$ = 4.5 x 10^{-5}.

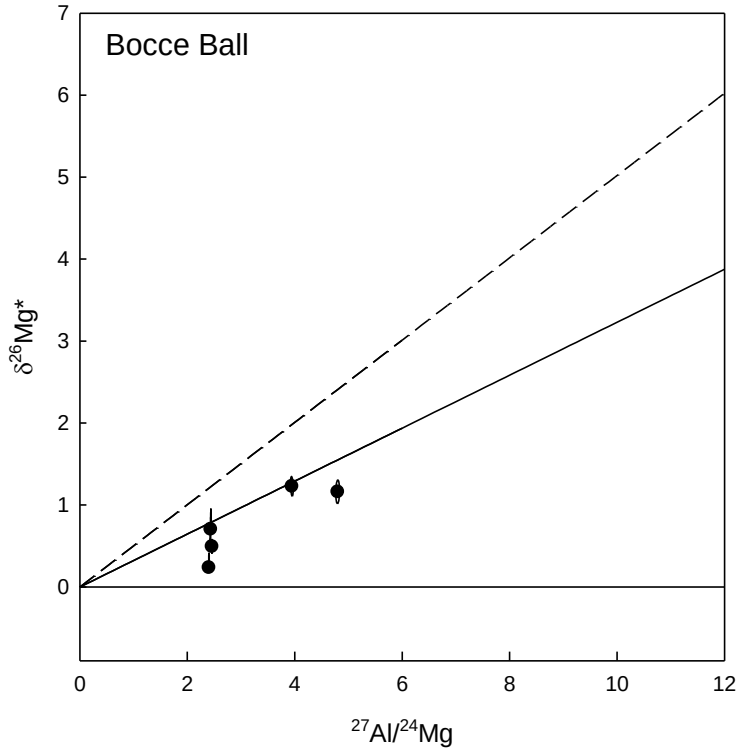

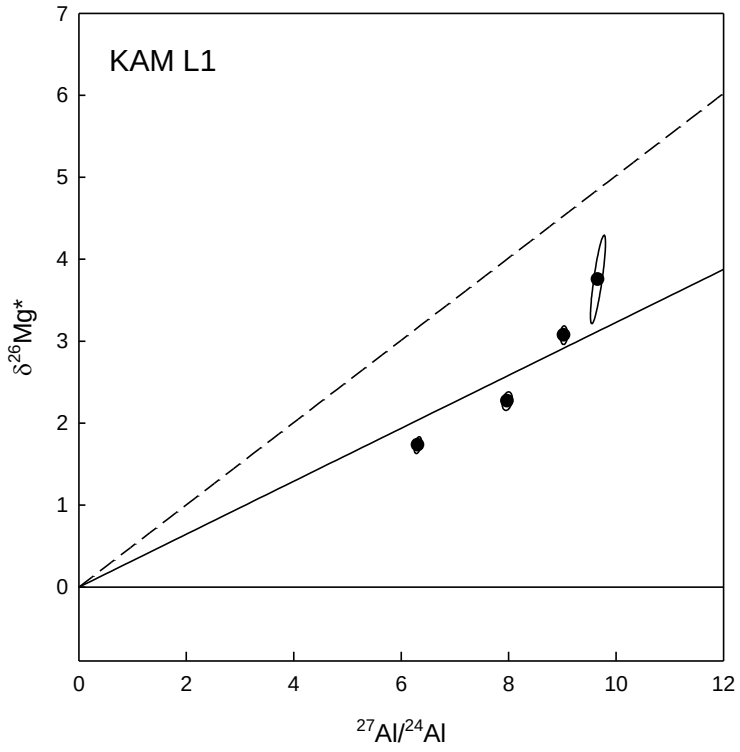
KAM L1
δ26Mg*
27Al/24Al
0
1
2
3
4
5
6
7
0
2
4
6
8
10
12

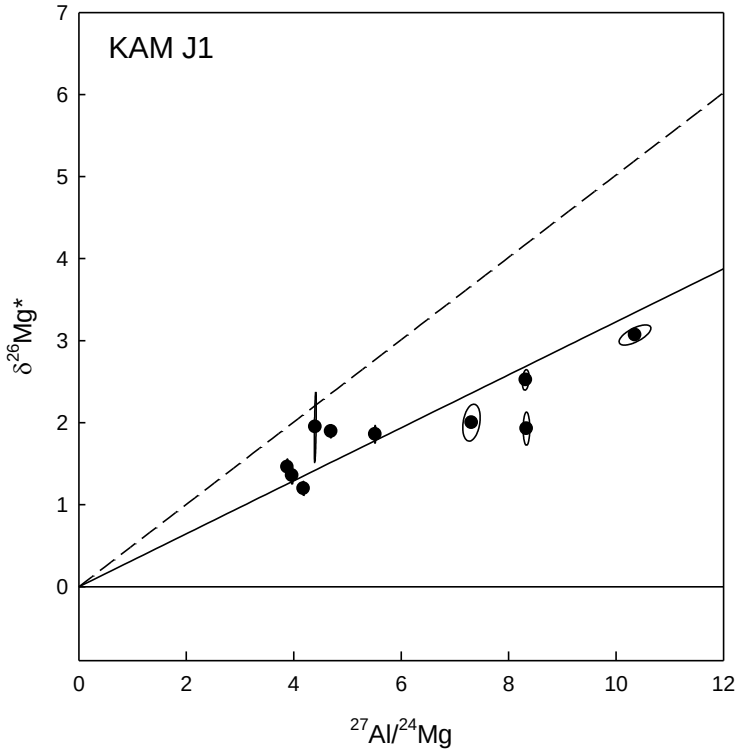
KAM J1
δ26Mg*
27Al/24Mg
0
1
2
3
4
5
6
7
0
2
4
6
8
10
12

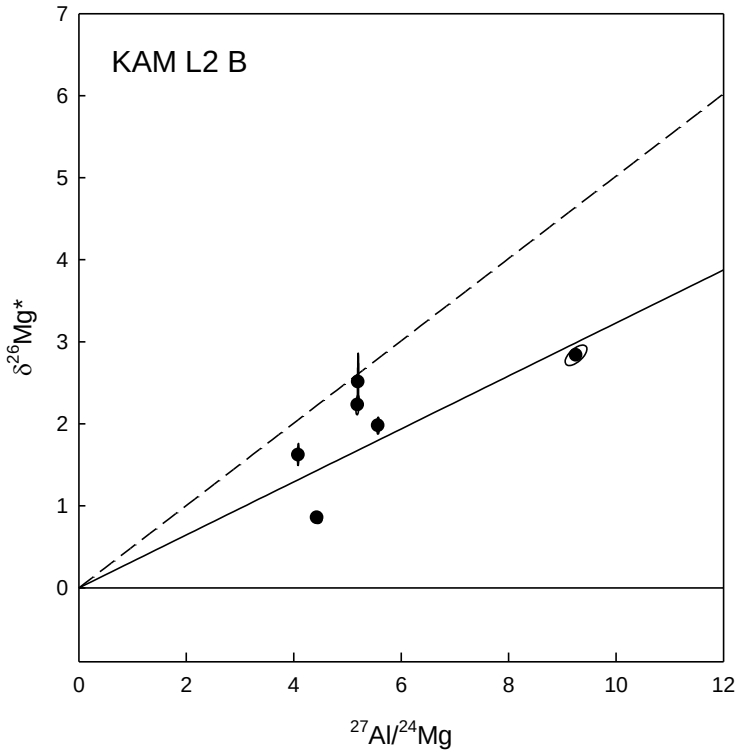
KAM L2 B
δ26Mg*
27Al/24Mg
0
1
2
3
4
5
6
7
0
2
4
6
8
10
12

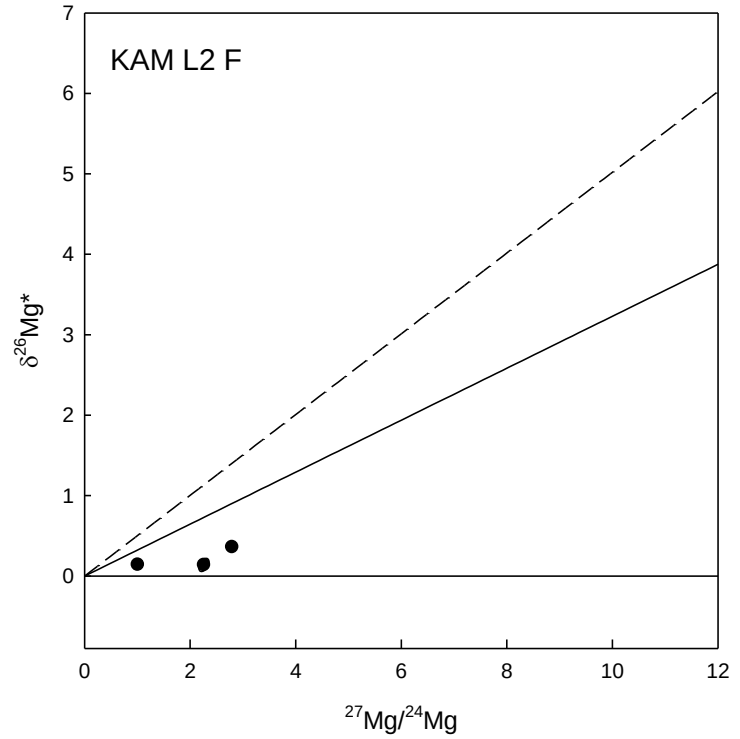
KAM L2 F
δ26Mg*
27Mg/24Mg
0
1
2
3
4
5
6
7
0
2
4
6
8
10
12

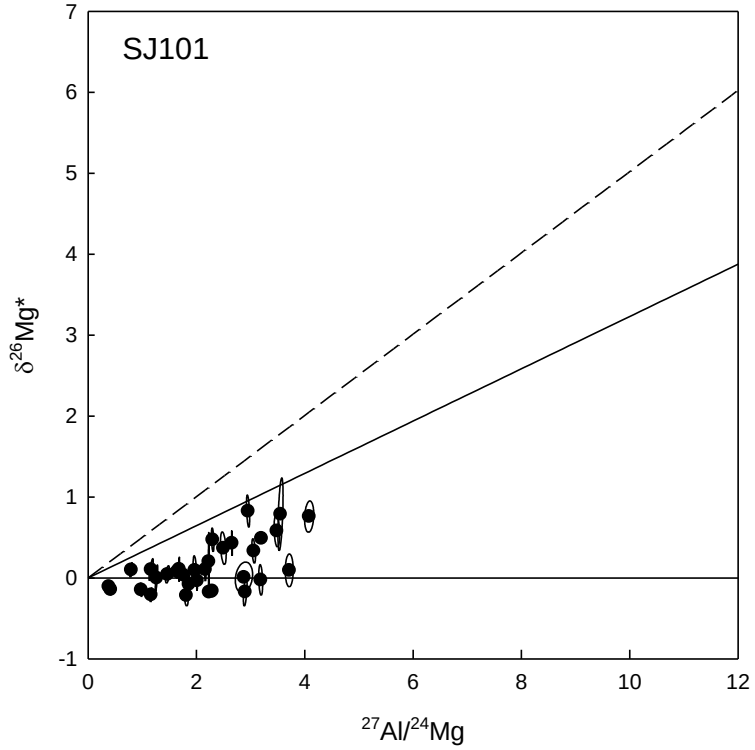
SJ101
7
6
5
4
3
2
1
0
-1
0
2
4
6
8
10
12
δ26Mg*
27Al/24Mg

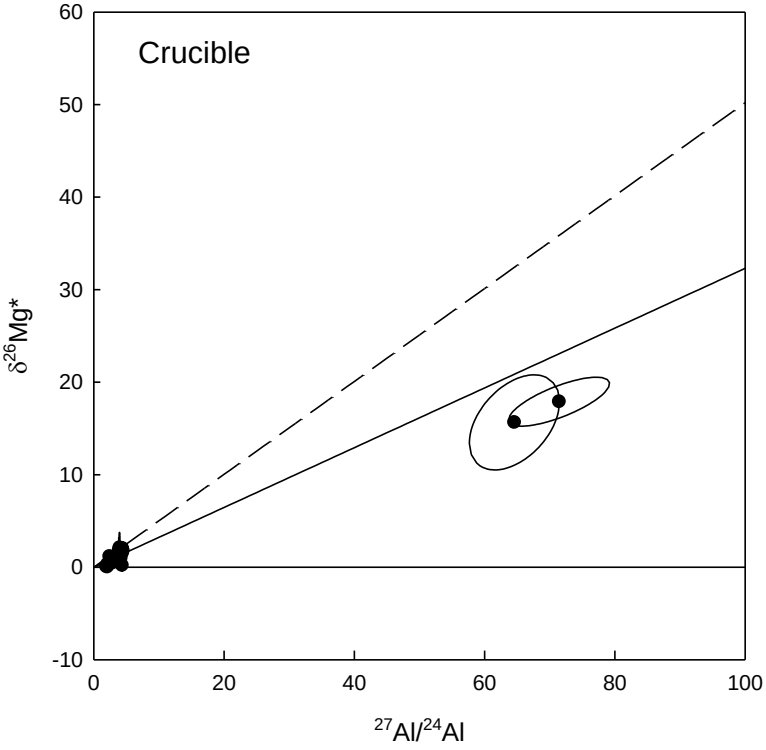
Crucible
60
50
40
30
20
10
0
-10
0
20
40
60
80
100
δ26Mg*
27Al/24Al

C2. Comparisons between isotopic systems, showing a lack of correlation between Ti (both δ^{49}Ti and ε^{50}Ti) and δ^{24}Mg, δ^{28}Si, and δ^{44}Ca. Values are the averages for individual CAIs in this study.

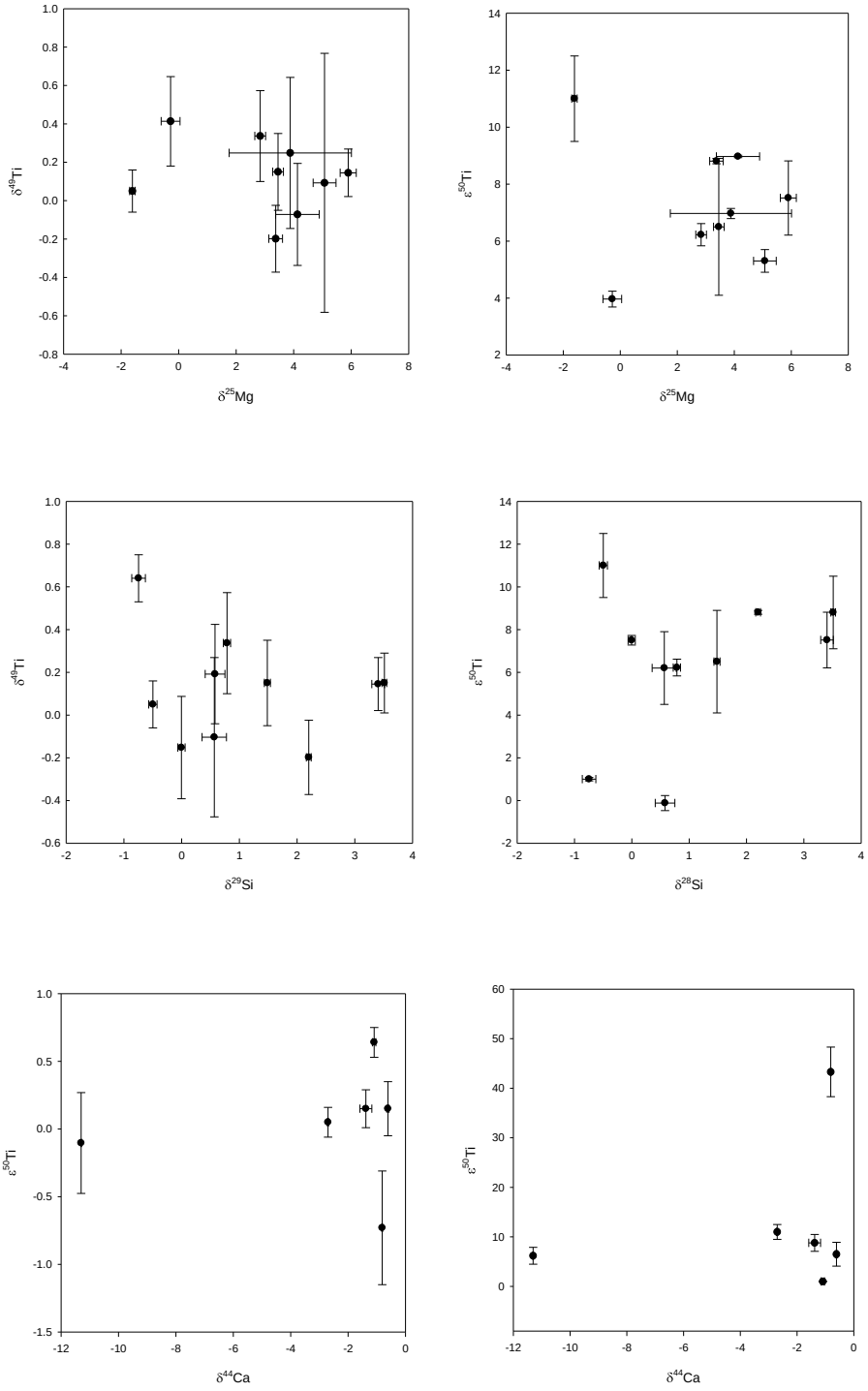

References

Alexander, C.M. O. D. 2001. Exploration of quantitative kinetic models for the evaporation of silicate melts in vacuum and in hydrogen. Meteoritical & Planetary Science **36**, 255-283.

Bullock, E.S., Knight, K.B., Richter, F.M., Kita, N.T., Ushikubo, T., MacPherson, G.J., Davis, A.M., and Mendybaev, R.A. 2013. Mg and Si isotope fractionation patterns in type B1 and B2 CAIs: Implications for formation under different nebular conditions. Meteoritical & Planetary Science **48**, 1440-1458.

Burkhardt, C., Kleine, T., Bourdon, B.,Palme, H., Zipfel, J., Friedrich, J. M., and Ebel D.S. 2008. Hf-W mineral isochron for Ca,Al-rich inclusions: Age of the solar system and the timing of core formation in planetesimals. GCA **72**, 6177-6197.

Chen, H., Lee, T., Lee, D., and Iizuka, Y., 2009. In situ Ti isotopic measurements by laser ablation MC-ICPMS. Terr. Atmos.Ocean Sci. **20**, 703-712.

Connelly Jr., H.C., Ebel, D.S., Weisberg, M.K., Beckett, J.R., and Paque, J.M. 2006. The petrography and geochemistry of an Allende type B CAI: V depletion, relict region, and remelting? LPSC XXXVII, Abstract #1521.

Connelly Jr., H.C., Huss, G.R., Shahar, A., Nagashima, K., Young, E.D., Ebel, D.S., Weisberg, M. K., Beckett, J.R., Paque, J.M., Ma, C., and Rossman, G.R. 2011. Diffusion within the CAI Bocce Ball 1: The redistribution of δ^{26}Mg*correlated with variations in Al/Mg within a type B2 inclusion from Allende. LPS XLII, Abstract #1858.

Davis, A.M. and Hashimoto, A.. 1995. Volatility fractionation of rare earth elements and other trace elements during vacuum evaporation. Meteoritical Society, 500-501.

Davis, A. M., Hashimoto, A., Clayton, R.N., Mayeda, T.K., 1990. Isotope mass fractionation during evaporation of Mg_2SiO_4. Nature **347**, 655-658.

Friedrich, J.M., Ebel, D.S., Weisberg, M.K., and Birdsell J. 2005. The Crucible: an unusual matrix enclosing igneous CAI in NWA2364. LPSC XXXVI, Abstract #1756.

Grossman, L., 1972. Condensation in the primitive solar nebula. Geochimica et Cosmochimica Acta **36**, 597-619.

Grossman, L., Ebel, D.S., Simon, S.B., Davis, A.M., Richter, F.M., and Parsad, N.M., 2000. Major element chemical and isotopic compositions of refractory inclusions in C3 chondrites: The separate roles of condensation and evaporation. Geochimica et Cosmochimica Acta **64**, 2879-2894.

Grossman, L., Simon, S.B., Rai, V.K. Thiemens, M.H., Hutcheon, I.D., Williams, R.W., Galy, A., Ding, T., Fedkin, A.V., Clayton, R.N., and Mayeda, T.K., 2008. Primordial compositions of refractory inclusions. Geochimica et Cosmochimica Acta **72**, 3001-3021.

Huang, S., Farkas, J., Yu, G., Peteav, M. I., and Jacobsen, S.B., 2012. Calcium isotopic ratios and rare earth element abundances in refractory inclusions from the Allende CV3 chondrite. Geochimica et Cosmochimica Acta **77**, 252-265.

Ireland, T.R., Zinner, E.K., Fahey, A.J., and Esat, T.M., 1992. Evidence for distillation in the formation of HAL and related hibonite inclusions. Geochimica et Cosmochimica Acta **56**, 2503-2520.

Jacobsen, S. B., Chakrabarti, R., Ranen, M.C., and Petaev, M.I., 2008. High resolution ^{26}Al-^{26}Mg chronometry of CAIs from the Allende meteorite. LPS XXXIX, Abstract #1999.

Jadhav, M., Amari, S., Marhas, K.K., Zinner, E., Maruko, T., and Gallino, R. 2008. New stellar sources for high-density, presolar graphite grains. The Astrophysical Journal **682**, 1479-1485.

Jouzel, J. and Merlivat L., 1984. Deuterium and oxygen 18 in precipitation: Modeling of the isotopic effects during snow formation. Journal of Geophysical Research **89**, 11749-11757.

Knight, K.B., Kita, N.T., Menybaev, R.A., Richter, F.M., Davis, A.M., and Valley, J.W., 2009. Silicon isotopic fractionation of CAI-like vacuum evaporation residues. Geochimica et Cosmochimica Acta **73**, 6390-6401.

Leya, I., Schönbächler, M., Krähenbühl, U., and Halliday, A. N. 2009. New titanium isotope data for Allende and Efremovka CAIs. The Astrophysical Journal **702**, 1118-1126.

MacPherson, G.J. 2014. Calcium-aluminum-rich inclusions in chondritic meteorites. Treatise on Geochemistry, 2nd Ed.

Niederer, F.R. and Papanastassious, D.A., 1984. Ca isotopes in refractory inclusions. Geochimica et Cosmochimica Acta **48**, 1279-1293.

Niederer, F.R., Papanastassious, D.A., and Wasserburg, G.J., 1985. Absolute isotopic abundances of Ti in meteorites. Geochimica et Cosmochimica Acta **49**, 835-851.

Niemeyer, S. and Lugmair, G. W. 1981. Ubiquitous isotope anomalies in Ti from normal Allende inclusions. EPSL **53**, 211-225.

Nittler, L. R., Alexander, C. O'D., Liu, N., Wang, J. 2017 Extreme chromium isotope anomalies in Orgueil nano-oxides: Presolar type IA supernova condensates. 80th Annual Meeting of the Meteoritical Society. Abstract #6330.

Petaev, M.I. and Jacobsen, S. B., 2009. Petrologic study of SJ101, a new forsterite-bearing CAI from the Allende CV3 chondrite. Geochimica et Cosmochimica **73**, 5100-5114.

Richter, F.M., 2004. Timescales determining the degree of kinetic isotope fractionation by evaporation and condensation. Geochimica et Cosmochimica Acta **68**, 4971-4992.

Richter, F.M., Davis, A.M., Ebel, D.S., and Hashimoto, A., 2002. Elemental and isotopic fractionation of type B calcium- aluminum-rich inclusions: Experiments, theoretical considerations, and constraints on their thermal evolution. Geochimica et Cosmochimica Acta **66**, 521-540.

Richter, F. M., Janney, P.E., Mendybaev, R.A., Davis, A.M., and Wadhwa, M., 2007. Elemental and isotopic fractionation of Type B CAI-like liquids by evaporation. Geochimica et Cosmochimica Acta **71**, 5544-5564.

Shahar, A., and Young, E.D., 2007. Astrophysics of CAI formation as revealed by silicon isotope LA-MC ICPMS of an igneous CAI. Earth and Planetary Science Letters **257**, 497-510.

Simon, J.I. and DePaolo, D.J., 2010. Stable calcium isotopic composition of meteorites and rocky planets. Earth and Planetary Sciences Letters **289**, 457-466.

Simon, J.I., Jordan, M.K., Tappa, M.J., Schauble, E.A., Kohl, I.E., and Young, E.D. 2017. Calcium and titanium isotope fractionation in refractory inclusions: Tracers of condensation and inheritance in the early solar protoplanetary disk. EPSL **472**, 277-288.

Simon, J.I., Young, E.D., Russell, S.S., Tonui, E., Dyl, K.A., and Manning, C.E. 2005. A short timescale for changing oxygen fugacity in the solar nebula revealed by high-resolution ^{26}Al-^{26}Mg dating of CAI rims. EPSL **238**, 272-283.

Williams, C.D., Janney, P.E., Hines R.R, and Wadhwa, M. 2010. Precise titanium isotope compositions of refractory inclusions in the Allende CV3 chondrite by LA-MC-ICPMS. Chemical Geology **436**, 1-10.

Young, E.D., Nagahara, H., Mysen, B.O., and Audet, D.M., 1998. Non-Rayleigh oxygen isotope fractionation by mineral evaporation: Theory and experiments in the system SiO_2. Geochimica et Cosmochimica Acta **62**, 3109-3116.

Young, E.D., Simon, J.I., Galy, A., Russell, S.S., Tonui, E., Lovera, O. 2005. Supra-canonical ^{26}Al/^{27}Al and the residence time of CAIs in the solar protoplanetary disk. Science **308**, 223-227.

Young, E.D. 2016. Bayes' theorem and early solar short-lived radionuclides: The case for an unexceptional origin for the Solar System. The Astrophysical Journal **826**, 129-134.

Zhang, J., Dauphas, N., Davis, A.M., and Pourmand, A. A new method for MC-ICPMS measurement of Ti isotopic composition: Identification of correlated isotopic anomalies in meteorites. JAAS **26**, 2197.

Chapter 3: Iron Isotope Constraints on Planetesimal Core Formation in the Early Solar System

Michelle K. Jordan,[1] HaoLan Tang,[1] Issaku E. Kohl,[1] and Edward D. Young[1]

[1]Department of Earth, Planetary, and Space Sciences, University of California, Los Angeles

3.1. Introduction

The prevalence of metallic planetary cores in the Solar System indicates that core formation is a fundamental process in planet building, making understanding core-mantle differentiation crucial to understanding planetary formation and evolution. However, this endeavor is difficult as we cannot directly sample the cores of currently intact planets and planetesimals. Additionally, samples of planetary mantles are limited for some bodies (Earth and certain meteorite groups) and absent for others. Some evidence for the nature of Earth's core comes from seismology and laboratory experiments. Observations of Earth's magnetic field and orbital characteristics can also be used to inform us about the interior of the planet. However, in order to understand the chemistry and chemical evolution of cores, we must appeal to analogs elsewhere in the Solar System. From a geochemical perspective, indirect methods such as the composition of primitive meteorites, isotopic measurements of meteorite samples, experimental petrology, and theoretical calculations provide us with a way to investigate core formation. Combining these methods allows us to form a more complete understanding of the process of core-mantle differentiation in a planetary body. In this study, we focus on the iron isotope compositions of meteorites and what they reveal about planetary cores.

Iron is one of the most abundant elements in terrestrial bodies. The element's prominence in both the cores and silicate mantles of planetary bodies makes Fe a useful tracer for planetary

differentiation and core formation. Fe stable isotope fractionation provides a tool for reconstructing accretion history and planetary differentiation.

The Fe isotope compositions of Earth, Moon, Mars (SNC meteorites), Vesta (HED meteorites), and several meteorite classes have been previously measured and the data exhibit variability among Solar System materials (Figure 3.1) (Zhu et al., 2002; Kehm et al., 2002; Poitrasson et al., 2004; Weyer et al., 2005; Weyer and Ionov, 2007; Schoenberg and von Blanckenberg, 2006, Horn et al., 2006; Dauphas et al., 2009; Craddock and Dauphas, 2011; Wang et al. 2013). One possible explanation for this variability is differences in the processes that produced the cores of these bodies.

Magmatic iron meteorites are thought to represent the cores of differentiated asteroid-sized bodies. The meteorite record indicates that these metallic cores have high $^{57}Fe/^{54}Fe$ with respect to chondritic composition by ~0.12‰ (Zhu et al., 2002; Kehm et al., 2002; Poitrasson et al., 2004; Weyer et al., 2005; Schoenberg and von Blanckenberg, 2006; Williams et al., 2006.; Horn et al., 2006; Dauphas et al. 2009; Craddock and Dauphas, 2011). This recognized difference between chondrites and magmatic iron meteorites is potentially explained if the heavy isotopes of Fe partition into the metallic melt during planetary differentiation and core formation. While the observation indicates that this may be the case, uncertainty arises due to the probable lack of a cogenetic origin for these rocks. To determine whether or not there is an Fe isotopic signature that accompanies metal-silicate differentiation, we measured the isotopic composition of both the metallic and silicate phases in two differentiated meteorites in which the iron isotopes are in equilibration between the aforementioned phases. Understanding the Fe isotope fractionation that accompanies core should provide insights into the history of accretion for planetary bodies as well as their compositions and relative core sizes.

Previous experimental work and measurements of pallasite meteorites have sought to establish the Fe isotope fractionation between metal and silicate at high temperatures, but results have been inconclusive with respect to both the sign and magnitude of Fe isotope metal-silicate fractionation (Zhu et al., 2002; Weyer et al., 2005; Poitrasson et al., 2005; Poitrasson et al., 2009; Shahar et al., 2015; Elardo and Shahar, 2017; Hin et al., 2012). Pallasites contain large amounts of both silicate (olivine) and Fe-rich metal and are thought to represent the core-mantle boundaries of their asteroidal parent bodies. However, inconsistent results have limited their usefulness. Some results indicate that the metallic phase is high in $^{57}Fe/^{54}Fe$ relative to silicate, some show the opposite, and still others show no discernable difference in Fe isotope ratios (Figure 3.2). The inconsistency may stem from variable degrees of equilibration between the olivine grains and the metallic matrix;some olivine grains may not be isotopically equilibrated with the metallic matrix (Weyer et al., 2005).

Several studies have also reported the Fe isotope fractionation between metal and silicate from piston-cylinder experiments at high temperatures and pressures (Poitrasson et al., 2009; Hin et al., 2012; Shahar et al., 2015; Elardo and Shahar, 2017). These studies have also yielded seemingly inconsistent results, although direct comparisons are complicated by differences in experimental conditions and phase compositions..

In order to determine the equilibrium Fe isotope fractionation between metal and silicate, we measured Fe isotope ratios in metal and silicate coexisting in two aubrite meteorites, Norton County and Mount Egerton. Due to the highly reducing conditions under which these aubrites formed, there is a significant amount of Si present in the metallic phase. The Si isotope ratios in silicates and metals in these differentiated meteorites have already been determined to be in equilibrium (Ziegler et al., 2010) , suggesting that the Fe isotopes are also in equilibrium. The

solubility of Si in Fe-rich metal is temperature dependent, allowing us to estimate a temperature of equilibration for these rocks and therefore the temperature-dependent Fe isotope fractionation between silicate and metal.

3.2. Samples and Analytical Techniques

3.2.1 Samples

The Norton County and Mount Egerton aubrites are differentiated igneous rocks, consisting primarily of nearly FeO-free enstatite with smaller amounts of plagioclase, diopside, olivine, metallic Fe-Ni, troilite, and other trace minerals. Unlike most aubrites, Mount Egerton is not a breccia. The FeO content of the enstatite in aubrites, in general, is much lower than that of terrestrial enstatite (Watters and Prinz, 1979). The low concentration of Fe in the silicate phase results from the extremely reducing conditions under which these meteorites formed; these rocks record some of the most reducing conditions present in Solar System materials (Casanova et al., 1993). These reducing conditions result in some rare minerals, such as oldhamite, which is not found in terrestrial rocks. Aubrites have large negative Eu anomalies, indicating that the rocks were likely formed by fractional crystallization of a melt (Wolf et al.; 1983).

The metal content of aubrite meteorites is variable (0.1-2.3 vol %) with the metal possessing high concentrations of Si due to the reducing conditions under which it formed; Si becomes more siderophile at low oxygen fugacity (Casanova et al., 1993; Wade and Wood, 2005). Metal is present as small inclusions in the enstatite grains, submicron-sized blebs in the matrix, irregularly-shaped grains up to several hundred micrometers, and larger centimeter-sized nodules. The metal is predominantly kamacite and has sulfide and silicate inclusions concentrated towards the grain edges, though these inclusions are rare. Both schreibersite and

perryite are frequently associated with metal grains, with perryite only existing in the larger centimeter-sized nodules (Casanova et al., 1993). Casanova et al. (1993) suggest that the metal in aubrite meteorites represents residual material trapped in a silicate magma during partial melting. A depletion of Cr in aubrites relative to CI chondrites suggests that the metal itself has not undergone fractional crystallization (Casanova et al., 1993).

Ziegler et al. (2010) measured the silicon isotope ratios in the metal and silicate phases of these meteorites and determined the $^{30}Si/^{28}Si$ fractionation between the phases. The agreement in temperature-dependent fractionation between that measured in the meteorite, ab initio calculations, and an experimental determination (Shahar et al., 2009, Zigler et al., 2010) has been taken as strong indication that the Si in metal and in silicate is in isotopic equilibrium. Given the evidence for Si isotopic equilibrium in these rocks, we infer that Fe is also in isotopic equilibrium, making the rocks suitable for our purposes. The temperature of equilibration is revisited in this study, however.

Norton County (Figure 3.3A) is the largest recovered aubrite meteorite. The brecciated meteorite consists of 84.5 vol % enstatite with forsterite, diopside, and plagioclase making up most of the remaining silicate material (Watters and Prinz, 1979). The enstatite in Norton County contains about 0.07 wt. % FeO. The low concentration of Fe in the silicate material makes measurements of the Fe isotope composition of this phase challenging. The metal occurs mainly as irregularly shaped grains and accounts for about 1-1.5 vol.% of the meteorite (Watters and Prinz, 1979; Okada et al., 1988; Casanova et al., 1993). It consists largely of kamacite, with 1.4 to 2 vol. % perryite, and up to 6 vol. % schreibersite (Watters and Prinz, 1979). The kamacite is principally Fe with ~0.91 wt. % Si and ~4.7 wt. % Ni (Watters and Prinz, 1979). Our sample of Norton County comes from the University of New Mexico collection (care of Prof. Carl Agee).

In total, ~104 g of Norton County were obtained; the large sample mass allows for extraction of sufficient silicate-hosted iron to yield a reliable measurement of Fe isotope ratios. We sampled large metal nodules in order to ensure that the metal phase could be easily identified and isolated.

Mount Egerton (Figure 3.3 B) is an unbrecciated meteorite from Western Australia (McCall 1965). It is often classified as an anomalous aubrite due to its relatively high metal content as compared to other aubrite meteorites (Casanova et al., 1993; McCall, 1965). The silicate portion of the meteorite is composed primarily of large enstatite crystals with smaller amounts of diopside (Waters and Prinz, 1979). Similar to Norton County, the enstatite phase contains 0.07 wt. % FeO. The metal, which appears as cm-sized blebs, is kamacite and comprises about 21 wt. % of the meteorite; perryite is associated with the metal phase (Watters and Prinz, 1979; Wai, 1970; Wasson and Wai, 1970; Casanova et al., 1993a). Troilite and schreibersite are minor phases in Mount Egerton (Wasson and Wai, 1970; Watters and Prinz, 1979; Watters and Prinz, 1980; Watters et al., 1980). The kamacite in Mount Egerton contains ~2 wt. % Si and ~6.25 wt. % Ni, with some metal inclusions in the enstatite containing up to 8.25 wt. % Ni (Watters and Prinz, 1979; Watters and Prinz, 1980; Watters et al., 1980). The Mount Egerton samples come from the UCLA collection and consisted of a piece that was mainly silicate material, weighing about 4.5 g and a separate ~340 mg metal slice.

The redox reaction involving oxidized and reduced forms of Si and Fe can be used to calculate equilibration temperatures for highly reduced meteorites because the equilibrium expressed in the redox reaction is highly temperature dependent (Larimer 1968; Wasson et al., 1994). The reaction involves the two most common phases in enstatite chondrites, enstatite and kamacite, thus one can derive metamorphic equilibration temperatures for the aubrite meteorites. Wasson et al. (1994) used the reaction is $2(FeSiO_3)_{pyx} + (Si)_{Fe\text{-}Ni} = 2(Fe)_{Fe\text{-}Ni} + 3(SiO_2)_{crist}$ to

estimate the temperature of Si equilibration in metal. When applied to Norton County, this method suggests an equilibration temperature of 1130 K ± 80 K. For Mount Egerton it yields a temperature of 1200 K ± 80 K. Uncertainties in the activity coefficients and Gibbs free energies of reaction limit the accuracy of the estimated equilibration temperature (Wasson et al., 1994; Ziegler et al. 2010). Once an equilibration temperature has been established, the value can be used in conjunction with the measured metal-silicate fractionation to determine the temperature dependence of Fe isotope fractionation for these phases.

In addition to the aubrite meteorites, we also measured the Fe isotope composition of several magmatic iron meteorites in order to assess whether or not fractional crystallization could have affected their Fe isotope compositions. In the absence of isotopic effects of fractional crystallization, the high δ^{57}Fe values of iron meteorites are more plausibly attributed to metal-silicate differentiation. There are several groups of iron meteorites with varying formation and thermal histories; the groups are classified by their chemical trends. For the magmatic iron groups, or non-silicate bearing groups, the compositional trends suggest solidification of a core from a metallic melt by fractional crystallization as the parent body cooled (Scott, 1972; Scott and Wasson, 1975). The fractional crystallization has been modeled using the Rayleigh equation (Wasson, 1999). Other processes such as assimilation of additional metal, dendritic crystallization, the onset of liquid immiscibility, and incomplete mixing of the molten core may complicate the history of these iron meteorites, but fractional crystallization seems to have dominated (Goldstein et al., 2009).

Group IIIAB iron meteorites were used for Fe isotopic analysis in this study. IIIABs are the most populated iron meteorite group as well as the group with the most well defined fractional crystallization elemental trends. (Goldstein et al., 2009; Wasson, 1999); the

concentrations of several incompatible elements, including arsenic, are correlated with the degree of fractional crystallization in IIIABs. We use the relative concentrations of the highly incompatible arsenic as a measure of degree of fractional crystallization. We measured the δ^{57}Fe of six magmatic iron meteorites from the IIIAB group, with varying As contents (see Results below), and thus, varying degrees of fractional crystallization in order to determine if there was a systematic difference in δ^{57}Fe that could be correlated with the degree of fractional crystallization. The meteorites with higher concentrations of As and higher degrees of fractional crystallization are Grant (15.5 μg/g As), Mount Edith (15 μg/g As), and Buenaventura (19.2 μg/g As) compared with the less evolved rocks that include Haig, Henbury, and Williamstown with As concentrations of about 3 μg/g. All iron meteorite samples are from the UCLA collection.

Our Fe isotopic measurements of iron meteorites are motivated by the study by Hopp et al. (2016) in which Ru isotope ratios were obtained for a collection of magmatic iron meteorites with varying degrees of fractional crystallization. Among the samples in that study were Henbury and Grant, representing samples with very different degrees of fractionation and allowing for direct comparison with our study. Hopp et al. (2016) found that the IIAB and IIIAB magmatic iron meteorites displayed a correlation between degree of fractional crystallization and Ru isotope ratios. $\delta^{102/99}$Ru values range from ~0‰ for those samples with low degrees of crystallization (e.g., Henbury) to ~0.85‰ for samples representing larger fractions of crystallization (e.g., Grant). This result suggests that the lighter isotopes of Ru favor the solid metal phase, leaving the remaining melt enriched in the heavy isotopes of Ru.

3.2.2 Phase separation, dissolution, and ion exchange chromatography

Silicate fractions of the aubrite meteorites were obtained by breaking off sizable enstatite crystals from larger pieces of both Norton County and Mount Egerton. Sample edges were abraded with silicon carbide to remove any lingering Fe-oxide. The enstatite crystals were crushed into fine grains using an agate mortar and pestle; metallic particles were removed from the powder using a hand magnet. A Frantz Magnetic Separator followed by handpicking were also employed to remove sulfide and other minor phases before dissolution. Metal samples for the aubrites and the IIIAB iron meteorites were cut using a diamond-blade saw. In the case of Norton County, we cut metal nodules away from the silicate mass; for Mount Egerton and the iron meteorites, we cut isolated metal pieces into smaller fragments. Iron oxides were removed by abrading with silicon carbide.

Silicate samples were dissolved on a hotplate in a 3:1 mixture of concentrated HF and HNO_3 in sealed Savillex Teflon beakers at ~155°C. After evaporation of the HF-HNO_3 mixture, samples were sequentially fluxed and evaporated in concentrated HNO_3, concentrated HCl, and aqua regia to fully dissolve the sample. The dissolution procedure follows that described in Baker et al. (2012). Metal samples were dissolved in concentrated HCl in sealed Savillex Teflon beakers on a hotplate at ~125°C. The solution was repeatedly centrifuged and decanted to remove any undissolved silicate material that was otherwise unable to be removed from the metal sample. Aliquots from the metal solution are fluxed in concentrated nitric acid to ensure that all Fe was present in the same oxidation state before being loaded onto resin columns.

Both metal and silicate samples were loaded onto an anion exchange column to isolate pure Fe. The silicate Mg:Fe ratio of ~500:1 required adjustment of typical column procedures to prevent column overload..

Column Procedure for Silicate Samples. Fe from the aubrite silicate samples as well as the chondrite samples were purified following the method described by Dauphas et al. (2009). Columns contained 1 mL of pre-cleaned AG1-X8 anion exchange resin (200-400 mesh). Once loaded into the column, the resin was then cleaned again with the following routine: 10 mL 18 MΩ H_2O, 10 mL 1 N HNO_3, 10 mL 18 MΩ H_2O, and 10 mL 0.4 N HCl to remove and Fe that may have been present. The column was then conditioned with 5 mL of 6 N HCl. The sample was loaded in ~0.5-1 mL 6 N HCl, depending on sample size. Non-Fe elements were eluted with 8 mL of 6 N HCl. Fe was eluted using 8 mL of 0.4 N HCl and collected in a clean Savillex beaker. The entire procedure is repeated a second time to ensure purity of the Fe. After collection, samples are dried down to a solid on a hot plate and dissolved again in 1 mL of 2% HNO_3 for analysis.

Column Procedure for Metal Samples. A smaller column, in terms of both length and volume of resin, was used to purify Fe from the metal samples. They consist of Bio-rad Poly-Prep columns with AG 1 – X8 resin (100-200 mesh, chloride form). The volume of resin was adjusted to 0.3 mL. The resin was cleaned with 10 mL of 9 N HCl, 10 mL of 18 MΩ H_2O, 10 mL of 9 N HCl, and 10 mL of 18 MΩ H_2O. The column was then conditioned with 6 mL of 0.5 N HCl and 3 mL of 9 N HCl. Samples were loaded in 300 µL of 9 N HCl. The beaker was washed with 500 µL of 9 N HCl. Matrix elements were eluted using 5 mL of 9 N HCl while Fe was eluted with 4 mL of 0.5 N HCl and collected in clean Savillex Teflon beakers. Samples were dried down on a hot plate at 125°C and subsequently dissolved in 1 mL of 2% HNO_3 for analysis.

Due to the small amount of Fe being measured, it was necessary to ensure low blanks for reliable data. Procedural blanks were run for the column technique to confirm sufficiently low blanks that would not interfere with analyses.

3.2.3 Mass Spectrometry

Data were collected on a ThermoFinnigan Neptune^{TM} multiple-collector inductively coupled plasma-source mass spectrometer (MC-ICP-MS). Samples were run in wet plasma mode. $^{54}Fe^{+}$_, $^{56}Fe^{+}$, $^{57}Fe^{+}$, and $^{58}Fe^{+}$ were measured simultaneously in Faraday cups with 10^{11} Ω amplifier resistors with ion currents between ~ 6×10^{-11} and 1.0×10^{-10} amps for ^{56}Fe. Samples were run at a mass resolving power (instrumental m/Δm) of >8,500 to eliminate interferences from $^{40}Ar^{14}N^{+}$ and $^{40}Ar^{16}O^{+}$; tests demonstrated isotope fidelity with this mass resolving power. Corrections for instrumental mass bias were made using sample-standard bracketing and peak height matching between sample and standard to within 5% of the standard's signal strength. Solutions were measured in a block of 20 cycles with long wash times (200 sec) in between to eliminate the possibility of cross-contamination between the sample and standard. Measurements outside two sigma of the block average were discarded. Samples were measured against our in-house SPEX CertiPrep® 2 standard. Reported values are calculated relative to the Fe standard IRMM-14 based on repeated measurements of our SPEX CertiPrep® 2 standard against IRMM-14.

We tested the column chemistry procedures for isotope fidelity using elemental SPEX CertiPrep® solutions mixed with a matrix composition approximating that of the silicate portion of Norton County. Aliquots of the mixture were processed on the columns according to our procedures and then compared with unprocessed, pure Fe SPEX CertiPrep®. No differences in

Fe isotopic composition were resolved. We also analyzed the eluted matrix to confirm the absence of Fe. Similar tests were performed for solutions mimicking the Fe-Ni alloy using the relevant column procedure.

3.3. Results

Fe isotope compositions for each meteorite and/or phase are reported as per mil deviations from the standard IRMM-14, δ^{57}Fe (Table 3.1). Multiple metal samples were dissolved and measured for both aubrite meteorites. However, only one silicate sample was dissolved and processed for each meteorite. This limited silicate sampling was due to the large amount of material required to obtain enough Fe for an accurate measurement

The average δ^{57}Fe values for the metal fractions from Norton County and Mount Egerton are 0.030‰ ±0.035 (2 SE) and 0.024‰ ±0.015 (2 SE), respectively. The average δ^{57}Fe values for the silicate fractions are -0.058 ‰ ±0.019 (2 SE) and -0.052‰ ±0.012 (2 SE), respectively. The calculated metal-silicate isotopic fractionation, $\Delta^{57}Fe_{metal\text{-}silicate}$, is 0.08‰ ± 0.039 (2 SE) for Norton County and 0.09‰ ± 0.019 (2 SE) for Mount Egerton. The positive value indicates that the heavy isotopes of Fe preferentially partition into the metallic phase during metal-silicate differentiation.

We can use the equilibration temperatures for these rocks in conjunction with the measured $\Delta^{57}Fe_{metal\text{-}silicate}$ to establish a temperature calibration since isotope fractionation at high temperatures varies as $1/T^2$ (Figure 3.4). Using the temperatures of equilibration of 1130 K for Norton County and 1200 K for Mount Egerton, and the measured fractionation, the calibration constant *A* was determined using $\Delta^{57}Fe_{metal\text{-}silicate} = A/T^2$. From *A* we can extrapolate over a range of relatively high temperatures curve. The Norton County data yield $\Delta^{57}Fe_{metal\text{-}silicate} = 1.12 \times 10^5/T^2$

and the Mount Egerton data yield $\Delta^{57}Fe_{metal\text{-}silicate} = 1.09 \times 10^5/T^2$. Uncertainties for these parameters are described in detail in the Discussion. Experimental results are plotted for comparison as well as the fractionation between metal and troilite measured by Wang et al. (2014). Metal-silicate and metal-troilite fractionation should be similar, making this comparison relevant (Polykov et al., 2007). Our results are broadly similar to earlier experimental work, though these experiments represent a variety of metal compositions and conditions making direct comparison difficult.

The measured CM chondrite whole rock samples span a range of $\delta^{57}Fe$ values from -0.030 to 0.020‰ f. These data fall within the typical range of Fe isotope compositions for carbonaceous chondrites. The average value is -0.004 ± 0.002‰.

The $\delta^{57}Fe$ values for the IIIAB iron meteorites range from +0.061 to +0.169‰ (± 0.02 2 SE). The measured values fall within the range of values seen in the literature for both magmatic iron meteorites overall and for IIIAB iron meteorites specifically (Zhu et al., 2002; Kehm et al., 2002; Poitrasson et al., 2004; Weyer et al., 2005; Schoenberg and von Blanckenberg, 2006; Williams et al., 2006.; Horn et al., 2006; Dauphas et al., 2009; Craddock and Dauphas, 2011). All values for the iron meteorites are positive relative to published chondrite values and those obtained as part of this study. Figure 3.5 shows the iron meteorite data from this study along with carbonaceous chondrite data measured on the same instrument at UCLA, illustrating that Fe comprising the iron meteorites is indeed isotopically heavy as compared to chondrites by an amount comparable to that in the literature.

The $\delta^{57}Fe$ values of the iron meteorites are plotted against the degree of fractional crystallization for those meteorites in Figure 3.6. We use arsenic as an indicator of the degree of fractional crystallization. Arsenic is the most incompatible of the commonly reported elements,

with a solid/liquid partition coefficient of D_{As} = 0.22 (Chabot and Jones, 2003), and thus, displays a large range of concentrations among magmatic iron meteorites. The concentration of As in the solid relative to the concentration in the least evolved melt provides a measure of the fraction of melt remaining, *F*, according to the relation:

$$\frac{C_{melt}^{As}}{C_0^{As}} = \frac{m_{melt}^{As}}{m_0^{As}} \frac{M_{melt}}{M_0} \sim F. \quad (3.1)$$

Here C_{melt}^{As} is the concentration of As remaining in the melt, C_0^{As} is the concentration of As in the initial metallic melt, prior to crystallization, m_{melt}^{As} is the mass of As remaining in the liquid, m_0^{As} is the mass of As in the initial system, M_{melt} is the total mass of the melt, and M_0 is the total mass of the initial system. Based on the incompatibility of As, we assume, to a reasonable approximation, that $m_{melt}^{As} \sim m_o^{As}$, and consequently, $C_{melt}^{As}/C_o^{As} \sim M_{melt}/M_o = F$. We take the concentration of As in the initial system to be the concentration of As in the magmatic iron meteorite sample with the lowest concentration of As since the concentration of As in the melt increases as crystallization progresses. We use the As concentration as a measure of the melt remaining in a Rayleigh fractional crystallization model. For Rayleigh fractionation, $R = R_o F^{\alpha-1}$, where *R* is the $^{57}Fe/^{54}Fe$ of the melt, R_o is the $^{57}Fe/^{54}Fe$ of the initial melt, $F = {}^{54}Fe/{}^{54}Fe_o$, and α is the solid/liquid $^{57}Fe/^{54}Fe$ isotopic fractionation factor for Fe.

Because of uncertainties in values for α, several Rayleigh fractionation curves are plotted along with the data in Figure 3.6. The different curves represent the case where the heavy isotopes of Fe partition into the solid metal (α = 1.0002) and the case where the lighter isotopes of Fe partition into the solid metal phase (α = 0.9998). The plot shows that there are no systematic trends among these magmatic iron meteorites; iron meteorites that crystallized late (Buenaventura, Grant, and Mt. Edith) span the same ranges of values for $\delta^{57}Fe$ as those that

crystallized early (Henbury, Haig, and Williamstown), indicating that fractional crystallization did not affect the Fe isotope composition of the magmatic iron meteorites.

3.4. Discussion

Our results indicate that the heavy isotopes of Fe partition into the metallic phase during metal-silicate differentiation. Figure 3.4 shows that the data from both rocks measured in this study are consistent with some previous experimental studies (within error). However, there are some discrepancies, particularly with the experimental work from Elardo and Shahar (2017). Here we address possible explanations for the offset between the measurements in natural samples from this study and some of the prior experimental results.

One reason for discrepancies between our results and some of the earlier experimental results is differences in the compositions of the metallic phases involved. The presence of significant concentrations of the principal non-iron components in the metal phases, Ni and S, can increase the Fe isotope fractionation between metal and silicate (Elardo and Shahar, 2017). The greater the non-iron substitutional constituent, the larger the effect on Fe isotope fractionation. We examine this effect for the aubrite meteorites measured in this study. Elardo and Shahar (2017) plotted $\Delta^{57}Fe_{metal\text{-}silicate}$ as a function of atomic percent Ni in their Fe-Ni alloy and determined a relationship between metal-silicate fractionation factor: $\Delta^{57}Fe_{metal\text{-}silicate} = 0.0112 \cdot (\text{at.\% Ni+S}) + 0.0346$ at 2123 K. Using the average compositions of our aubrite metals (Watters and Prinz, 1979; Watters and Prinz 1980) of 4.7 wt. % Ni for the metal in Norton County and 6 wt. % Ni for the metal in Mount Egerton, we calculate that the $^{57}Fe/^{54}Fe$ metal-silicate fractionation is ~0.085 to 0.1‰ greater than it would otherwise be if no Ni was present (at 2123 K). Adjusting for Ni concentration allows for direct comparisons between the

temperature-dependent $^{57}Fe/^{54}Fe$ metal-silicate fractionation from the experimental data and our measured aubrite data. Nonetheless, even accounting for diluent Ni concentrations, the experimental data and those from the two aubrites reported here are in disagreement, with the experimental data suggesting a greater metal-silicate fractionation.

Another factor that may be responsible for the discrepancy is the validity of the temperature of equilibration in the meteorite samples. Partial melting experiments of enstatite chondrite material can help us assess the equilibration temperature. Aubrites are likely related to enstatite chondrites as the two meteorite groups are both composed primarily of nearly FeO free enstatite, were formed under reducing conditions, and share similar oxygen isotopic compositions (Watters and Prinz, 1979; Clayton et al., 1984; Clayton and Mayeda, 1996; Keil, 2010). Due to the similar mineraologies and apparent oxygen fugacities, enstatite chondrite partial melting experiments are relevant to the temperature of equilibration for the aubrite meteorites measured in this study. McCoy et al. (1999) conducted partial melting experiments of the Indarch enstatite chondrite and found a silicate solidus temperature of 1273 K, with the silicate being completely molten at 1773 K. Based on the Cr-Cr_2O_3 and V-V_2O_3 calibrations of Righter et al. (2017), the experiments were conducted at oxygen fugacities relative to the iron-wüstite buffer of approximately ΔIW−6 to ΔIW −8. The experiments suggest that the previously derived equilibration temperatures of 1130 K for Norton County and 1200 K for Mt. Egerton may be too low.

A study by Berthet et al. (2009) further supports higher temperatures of equilibration for these enstatite-clan meteorites. Berthet et al. (2009) also conducted partial melting experiments on Indarch. The experiments were made over a similar temperature range, but at higher pressure (1 GPa) than the McCoy et al. (1999) experiments (ambient pressure Additionally, the Berthet et

al. (2009) experiments explored various f_{O2} conditions. The more reducing, lower f_{O2} conditions were replicated by adding Si to the starting material at varying weight percent levels to achieve f_{O2} values of from ΔIW – 1.5 to IW – 5. Bethet et al. (2009) found that solidus and liquidus temperatures for the silicate material increased with decreasing fO_2. When melting pure Indarch with no Si metal added (~IW – 1.5), silicate partial melting reached ~7% at 1473 K and was completely molten at 1873 K. The solidus temperature was determined to be slightly below 1473 K. More reducing conditions further increased these temperatures. In the case where 6 wt. % Si metal was added to the starting material (IW – 4.5), the solidus temperature was above 1573 K, with silicate melting reaching 16 vol. % at 1673 K. Previous work suggests that the oxygen fugacity for aubrite equilibration is approximately 4.5 to 6.5 log units below the IW buffer (Righter et al. 2006; Casanova et al. 1993). The higher temperatures for initial melting in the Beth3t et al. study compared with those from the McCoy et al. study can be explained, in part, by the higher pressures for the former; Clapeyron slopes for dry melting suggest that 1 GPa could account for melting temperatures between ~100 and 200 K higher than those temperatures at 1 bar (10^{-5} Pa). The sizes of the parent bodies for these rocks are unknown, and so is the pressure of melting, but regardless, the McCoy et al. (1999) experiments and Bethet et al. (2009) experiments bracket likely melting conditions and are consistent in suggesting that the previously calculated equilibration temperatures for Norton County and Mount Egerton are too low to accommodate melting. We employ updated activity models in order to determine a more accurate temperature of equilibration for the aubrite meteorites analyzed in this study.

Corgne et al. (2008) explore the effects of temperature, pressure, and melt composition on the partitioning behavior of several elements, including Si. Silicon behaves as a siderophile element at low oxygen fugacity. Higher temperatures also increase the affinity of Si for the metal

phase, while the composition of the silicate melt and pressure have negligible effects on solubility. We apply the equation from Corgne et al. (2008) to our system as follows:

$$\log\left(\frac{x_{\mathrm{Si}}^{\mathrm{metal}}}{x_{\mathrm{SiO2}}^{\mathrm{silicate}}}\right) = a + \frac{b}{T} + \frac{cP}{T} + d\frac{nbo}{t} - \Delta IW + 2\log\left(\frac{\gamma_{\mathrm{FeO}}^{\mathrm{silicate}}}{\gamma_{\mathrm{Fe}}^{\mathrm{metal}}}\right) - log\left(\frac{\gamma_{\mathrm{Si}}^{\mathrm{metal}}}{\left(\gamma_{\mathrm{Fe}}^{\mathrm{metal}}\right)^2}\right). \quad (3.2)$$

In Equation (3.2), a, b, c, and d are regression constants, *T* is the temperature in K, *P* is the pressure in GPa, and nbo/t is the molar ratio of non-bridging oxygens to tetrahedral cations in the silicate melt. The mole fraction of the relevant element in the relevant phase is x_M^{phase}. We use this equation to determine the equilibration temperatures based on our understanding of the activity coefficients (γ_M^{phase}) and the oxygen fugacity (f_{O2}) under which aubrite meteorites formed. As suggested by Corgne et al. (2008), we use a value of 0.8 for $\gamma_{\mathrm{Fe}}^{\mathrm{metal}}$ (they also suggest a value of $\gamma_{\mathrm{Fe}}^{\mathrm{metal}}$ = 1 for the primitive mantle, we obtain the same result whether we use 0.8 or 1). The $\gamma_{\mathrm{FeO}}^{\mathrm{silicate}}$ is less well constrained. Corgne et al. (2008) suggest $\gamma_{FeO}^{silicate}$= 3 ± 1 for a MgO content of ~30 wt. %. Holzheid et al. (1997) found that silicate melts with high MgO contents increase the activity coefficient for FeO in the silicate melt. Since both Norton County and Mount Egerton have high MgO contents in the silicate material (~40 wt. %), we evaluated the effect of MgO on $\gamma_{\mathrm{FeO}}^{\mathrm{silicate}}$. The experimental data from Holzheid et al. (1997) are plotted in Figure 3.7. We use the resulting trend line to calculate $\gamma_{\mathrm{FeO}}^{\mathrm{silicate}}$ (MgO = 40 wt. %) and the associated errors. From this relationship we find that $\gamma_{\mathrm{FeO}}^{\mathrm{silicate}}$ = 5.83 ± 0.95 (1 S. E.). Other parameters and reference values are taken from the Corgne et al. (2008) paper and adjusted for temperature and pressure where necessary. We use an f_{O2} of IW – 6.5 as suggested by literature values reported for aubrite meteorites (Righter et al., 2006). With these parameters, we adjust the equilibration temperature to a value that reproduces the Si concentrations in the metals for

Norton County (0.91 wt % Si) and Mount Egerton (2 wt. % Si). From this exercise, we estimate equilibration temperatures of ~1415 K for Norton County and 1460 K for Mount Egerton. These temperatures are higher than the previous estimates by ~200 degrees but are consistent with the partial melting experiments, which suggest silicate melting begins at a minimum of 1273 K for an aubrite-like composition. The temperature calibrations for $\Delta^{57}Fe_{metal\text{-}siliacate}$ implied by these new equilibration temperatures and our measured Fe isotope ratio data are plotted in the top panel of Figure 3.8. The results for both a 5 and 6 wt. % Ni calibration from the experiments in Elardo and Shahar (2017) are also shown for comparison.

Error envelopes for the temperature-dependence of $\Delta^{57}Fe_{metal\text{-}siliacate}$ are based on the uncertainty of A (σ_A) in the relationship between fractionation and temperature, $\Delta^{57}Fe_{metal\text{-}siliacate} = A/T^2$. The uncertainty in the temperature coefficient A is

$$\sigma_A = \sqrt{T^4\sigma^2_{\Delta 57Fe} + \left(2 \cdot \Delta^{57}\mathrm{Fe}\right)^2 \sigma_T^2}, \tag{3.3}$$

where $\sigma^2_{\Delta 57\mathrm{Fe}}$ is the 1 s.e. uncertainty in the measured isotope ratios and σ_T^2 is the uncertainty in temperature. For Norton County and Mount Egerton, the temperature uncertainties of ±17.5 K arise from the uncertainties in $\gamma_{FeO}^{silicate}$ of ~ +/- 1 derived from the fit in Figure 3.7, translating to uncertainties in A of +/- 4 x 10^4 for Norton County and 2.2 x 10^4 for Mount Egerton (or 1-2%). For the experiments, there is no uncertainty in temperature and the term $\left(2 \cdot \Delta^{57}Fe\right)^2 \sigma_T^2$ goes to zero. At these higher temperature calibrations, the plot shows that there is marginal agreement at the extremes of the error envelopes.

The uncertainties in the activity coefficient of FeO in the silicate melt go beyond those obtained from the fit in Figure 3.7. Wood and Wade (2013) attempted to constrain the activity coefficient of FeO in silicate melts over a range in compositions. They amassed data for 83

experiments from several different studies in the literature, including Holzheid et al. (1997). In all of these experiments, the authors had measured the FeO content of the silicate melt in equilibrium with metal (Fe-bearing alloy) at known f_{O2}. Wade and Wood (2013) fit the data to obtain the relationship between silicate melt composition and $\gamma_{FeO}^{silicate}$. The results of this model do not agree with the relationship shown in Figure 3.7. The Wade and Wood (2013) results suggest that a value for $\gamma_{FeO}^{silicate}$ of 5.83 may be too high and that the coefficient is not as sensitive to melt composition as suggested in the work of Holzheid et al. Wade and Wood provide an equation for $\gamma_{FeO}^{silicate}$ as a function of melt compositions, but the equation cannot be used to extrapolate beyond the range of composition space spanned by the experimental data set. Our enstatite composition of 0.07 wt. % Fe for the aubrite meteorites is outside the range covered by their analysis. Nonetheless, the results of Wade and Wood at face value suggest FeO activity coefficients near unity. For completeness, we also perform our calculations with $\gamma_{FeO}^{silicate} = 1$ to explore the sensitivity of the results to this activity coefficient. The resulting values for A are $2.33 \times 10^5 \pm 5.3 \times 10^4$ for Norton County and $2.14 \times 10^5 \pm 2.8 \times 10^4$ for Mount Egerton. The results are plotted in Figure 3.8. The lower gamma value yields a higher temperature of equilibration and shifts the curves for Norton County and Mount Egerton to the right, resulting in a higher degree of agreement between our study and the experimental work of Elardo and Shahar (2017).

Because the exact value of the activity coefficient for FeO in silicate is not known, and because the oxygen fugacity calculated for a given temperature and Si concentration in metal depends on this coefficient, we derive a range of temperatures from Equation (3.2) by applying a range of values for both f_{O2} and $\gamma_{FeO}^{silicate}$. Figure 3.9 shows several temperature curves that are dependent on f_{O2} and $\gamma_{FeO}^{silicate}$. We adopt the temperatures of 1415 K for Norton County and

1460 K for Mount Egerton, as these values take into consideration the high MgO value of the rocks and are consistent with the relevant melting experiments. They are also a lower bound for the discussion that follows.

With an estimate for the equilibration temperature and thus, equilibrium metal-silicate Fe isotope fractionation, we examine what this information reveals about the cores of planetesimals. Thermal models (Figure 3.10) of Vesta show that the core reached a temperature of ~1800 K (model published by one of us in Zhou et al., 2013). We use our calibrations established at 1415 K and 1460 K for the Norton County and Mount Egerton meteorites, respectively, in conjunction with mass balance, to calculate the δ^{57}Fe values for the silicate and metallic phases of a body as a function of core size where core and mantle equilibrated at 1800 K (i.e. Vesta). The mass balance equation is

$$\delta^{57}Fe_{\text{metal}} = \delta^{57}Fe_{\text{bulk}} + x_{\text{Fe}}^{\text{silicate}}\Delta^{57}Fe_{\text{metal-silicate}}(T)\,. \quad (3.4)$$

We use our measured $\Delta^{57}Fe_{\text{metal-silicate}}$ and Equation (3.4) to determine the fractions of Fe in silicates and metals in order for the iron cores to have higher $^{57}Fe/^{54}Fe$ than the silicate mantles assuming $\delta^{57}Fe_{\text{bulk}}$ = chondrite (Figure 3.11). The two solid lines in Figure 3.11 represent δ^{57}Fe values for coexisting metal and silicate as a function of the fraction of iron contained in the silicate portion of the body. For a body with a core/mantle mass ratio like the Earth, the silicate should be low in δ^{57}Fe and metal should be nearly chondritic because the core dominates the iron budget. Conversely, smaller cores with greater fractions of the Fe in the silicate mantles increase the δ^{57}Fe of the core to values greater than chondritic. However, even at extremely small core sizes, the observed elevated $^{57}Fe/^{54}Fe$ among magmatic iron meteorites relative to chondrite is difficult to explain using the fractionation between silicate and metal that we observe in the meteorites themselves.

The high $^{57}Fe/^{54}Fe$ among magmatic iron meteorites could be explained, at least qualitatively, using our calibration if planetesimals had relatively small cores *and* these cores had impurities consistent with the 8-10 wt. % Ni content of most magmatic iron meteorites. With small core sizes (~15% by mass), a $\Delta^{57}Fe_{metal\text{-}silicate}$ with a value of approximately 0.19‰ could account for the observed difference between iron meteorites and chondrites. Such small core sizes are not unreasonable (Toplis et al., 2013). The metal/silicate $^{57}Fe/^{54}Fe$ fractionation of 0.19‰ can be reconciled with our data within errors if we adjust our results to accommodate the Ni content of magmatic iron meteorites using the dependence of fractionation on Ni content from Elardo and Shahar (2017). Although the values for Ni contents of iron meteorites ranges from 5-60 wt. %, the vast majority fall between 5 and12 wt. %, with an average of ~8-10 wt. % for magmatic iron meteorites (Goldstein et al., 2009). In order to accommodate the more typical Ni contents we use the $d\Delta^{57}Fe/d$[%Ni] relationship from Elardo and Shahar combined with our average measured metal/silicate fractionation factor from the aubrites to arrive at the expression

$$\Delta^{57}Fe_{metal\text{-}silicate} = 7.1x10^4/T^2 + 0.0112(\%Ni - 5.6). \quad (3.5)$$

For this calculation, we use the higher temperatures of equilibration obtained from $\gamma FeO = 1$ in order to maximize the fractionation factor. The value for *A* and the atom % Ni of 5.6 in Equation (3.5) are both averages for the two aubrites. The results from Equation (3.5) are not especially sensitive to the choice of γFeO. For example, at 1800K and a 10%Ni content, the calculated $\Delta^{57}Fe_{metal\text{-}silicate}$ is 0.072 ‰ using the *A* values for $\gamma FeO = 1$ while the $\Delta^{57}Fe_{metal\text{-}silicate}$ value for $\gamma FeO = 5.8$ is 0.067 ‰ at the same temperature.

The mass balance equation assumes that the bulk composition of the planetary body is chondritic. There are reasons to question this assumption. Hin et al. (2017) found that chondrites are ~0.02‰ lower in $^{25}Mg/^{24}Mg$ than Earth, Mars, eucrites, and angrites. Their modeling

suggests that this heavy signature of various planetary bodies can result from evaporation of molten rock after collisions during the accretionary growth phase of planetesimals. This effect would have similar consequences for Si and Fe if scaled to the equilibrium vapor/melt fractionation factors for those systems. As a result, iron meteorite parent bodies may have accreted from objects that were already heavy in $^{57}Fe/^{54}Fe$ relative to chondrite. The data in Table 3.1 show that the metal in aubrites is low in $^{57}Fe/^{54}Fe$ relative to the IIIAB iron meteorites. We show in this study that the heavier isotopes of Fe partition in the metal phase during metal-silicate differentiation in natural systems. We postulate that a scenario could exist in which aubrites are pre-collisional materials and that the $\delta^{57}Fe$ of metal in aubrites increases due to metal-silicate differentiation. Subsequent to this mechanism, evaporation during collisions causes preferential loss of the heavier isotopes of Fe, leaving planetesimal cores even heavier due to the combined processes of differentiation and evaporation.

As a final alternative interpretation, we consider the possibility for sub-solidus equilibration at the temperatures previously obtained for these rocks. In this case, we assume that the initial temperatures of equilibration for the aubrite meteorites are correct, 1130 K for Norton County and 1200 K for Mount Egerton. These temperatures were calculated using the redox reaction from Wasson et al. (1994). Consistency between theory, experiments, and measurements for metal-silicate Si isotope partitioning in these rocks as described by Ziegler at al. (2010) argues for the lower temperatures of equilibration. If we assume that the lower temperatures of equilibration are in fact correct, then we must use the same temperatures of equilibration for the Fe isotope data and return to our original temperature calibration in Figure 3.4. In this low temperature equilibration case, it becomes impossible to attribute the difference in Fe isotope composition of iron meteorites and chondrites to metal-silicate differentiation. For

the low temperature equilibration scenario, the high $^{57}Fe/^{54}Fe$ of iron meteorites cannot be attributed to simple core formation and would require a post-formation evaporation event.

3.5. Conclusion

We determined the Fe isotope fractionation between the metal and silicate phases of two aubrite meteorites, Norton County and Mount Egerton. We find that the metallic phase is high in $^{57}Fe/^{54}Fe$ with respect to the silicate phase, and that $\Delta^{57}Fe_{metal\text{-}silicate}$ (relative to IRMM-14) is 0.08‰ for Mount Egerton and 0.09‰ for Norton County. Based on prior work suggesting isotope partitioning at equilibrium, two different cases were explored for estimating the temperature of equilibration. In the lower temperature case, we use the temperatures of equilibration calculated via the method of Wasson et al. (1994), 1130 K for Norton County and 1200 K for Mount Egerton. In this case, we are unable to explain the observed difference in the Fe isotope compositions of magmatic iron meteorites and chondrites as being the result of planetesimal differentiation.

In the higher temperature scenario, we use updated activity models and adopt a range of activity coefficients for FeO in the silicate melt with corresponding ranges in oxygen fugacity. The updated activity models suggest higher temperatures of equilibration, 1415 K for Norton County and 1460 K for Mount Egerton. If these temperatures are correct, we are able to explain the iron and chondrite meteorite data through differentiation if the planetesimal cores were relatively smaller (~15% by mass) and there were large impurities in the core, on the order of those present in magmatic iron meteorites (~8-10%).

Finally, the enrichment in $^{57}Fe/^{54}Fe$ of iron meteorites can potentially be explained by the combined mechanisms of metal-silicate differentiation and evaporation of melt formed by

collisions. Both these mechanisms result in heavier iron isotope compositions and their collective effect could possibly produce the correct magnitude of enrichment.

6. Acknowledgements

We would like to thank Edwin Schauble and Anat Shahar for helpful discussions, Carl Agee for providing us with the Norton County sample, and John Wasson for providing us with the Mount Egerton sample, all iron meteorite samples, and useful discussions. Funding was provided by a grant from the NASA Emerging Worlds program.

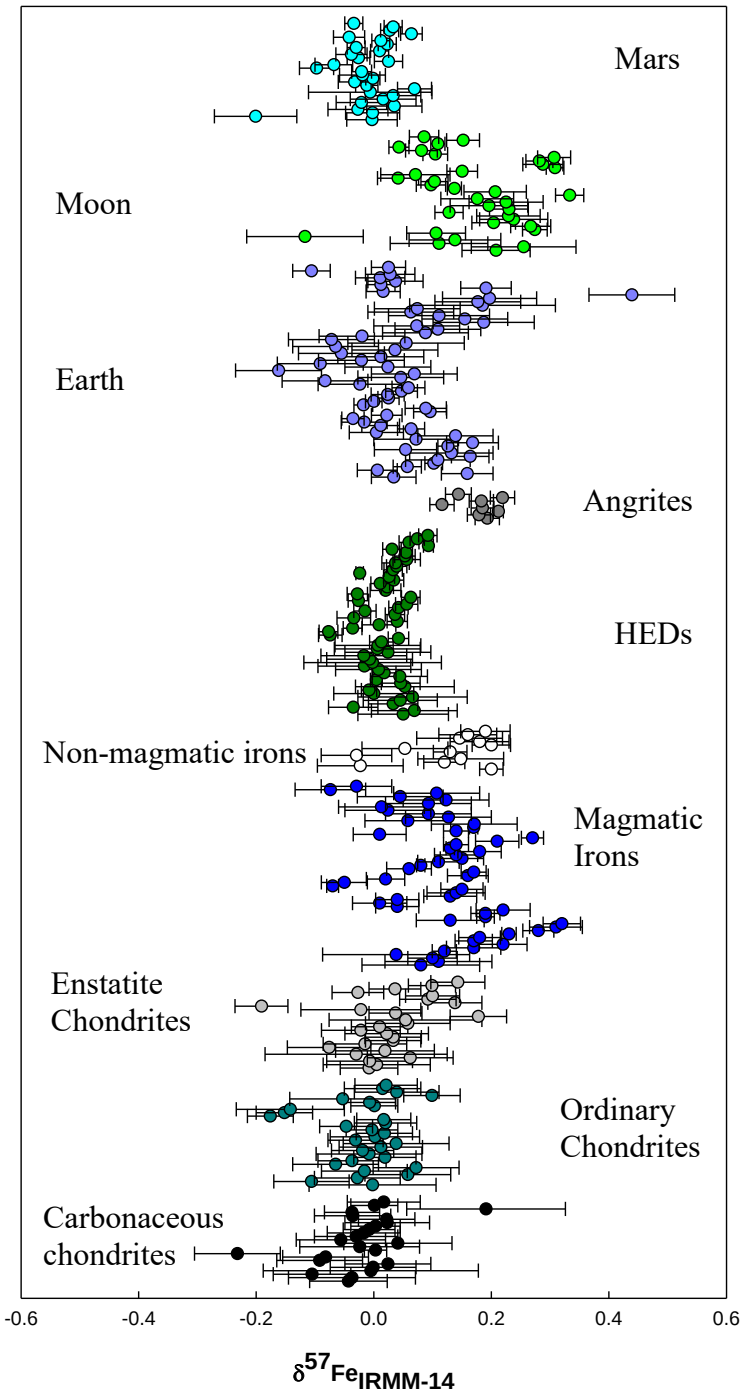

Figure 3.1 The Fe isotope composition of several planets and meteorite groups are plotted to show the variability among different Solar System bodies. Note that iron meteorites, Earth, Moon, and angrites are all isotopically heavy relative to chondrite. Data are compiled from the following studies: Zhu et al., 2002; Kehm et al. 2002; Poitrasson et al., 2004; Weyer et al., 2005; Weyer and Ionov, 2007; Schoenberg and von Blanckenberg, 2006; Horn et al., 2006; Dauphas et al., 2009; Craddock and Dauphas, 2011; Wang et al., 2013.

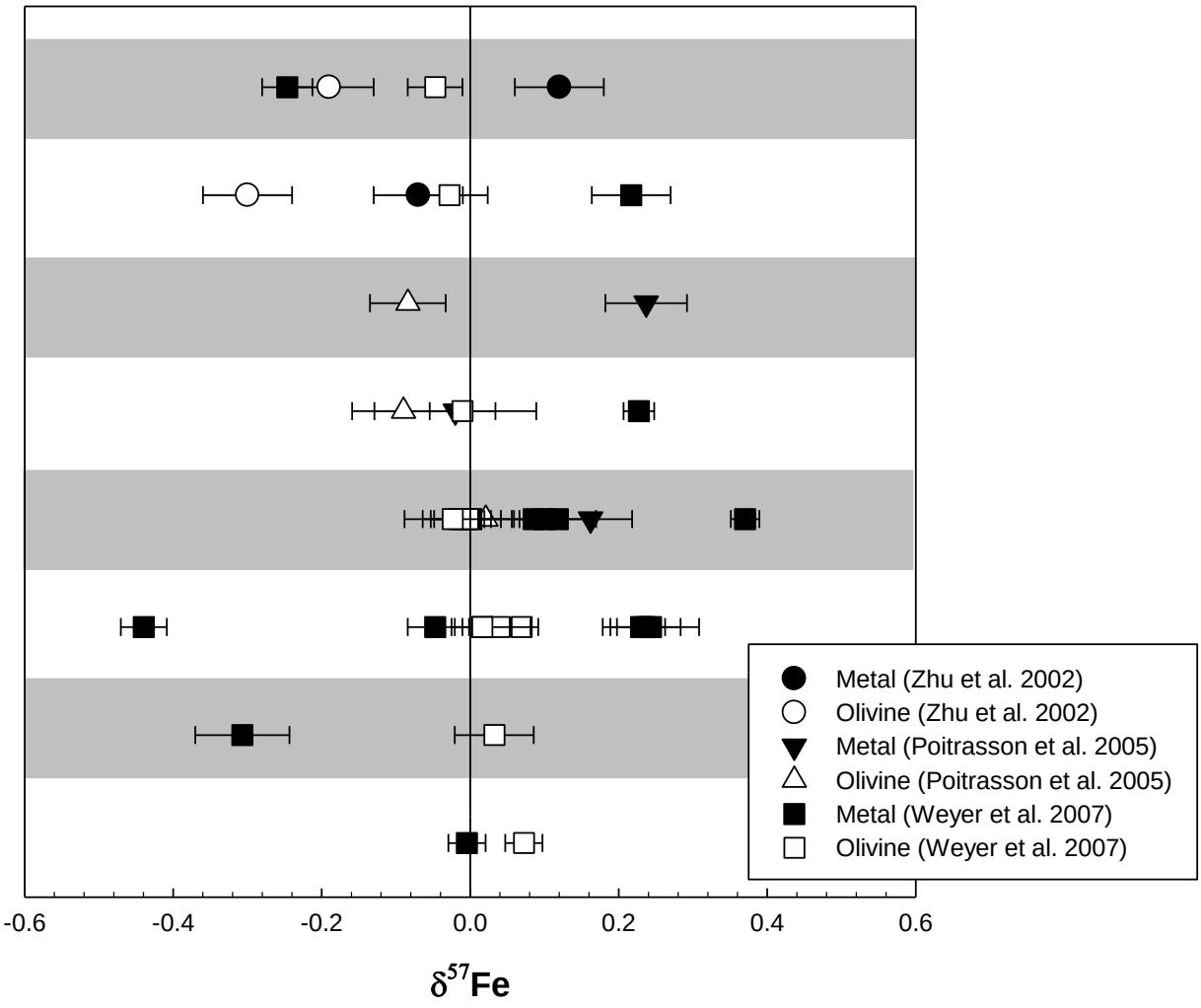

Figure 3.2: Measurements of olivine and metal separates are plotted here. Black symbols represent metal separates and white symbols represent olivine separates. Various shapes indicate that the data were collected from different groups. Each white or gray band represent a specific pallasite meteorite. The studies attempt to measure the equilibrium Fe isotope fractionation between metal and silicate, but show no systematic trend. Data are compiled from the following studies: Zhu et al., 2002, Poitrasson et al., 2005; and Weyer et al., 2007.

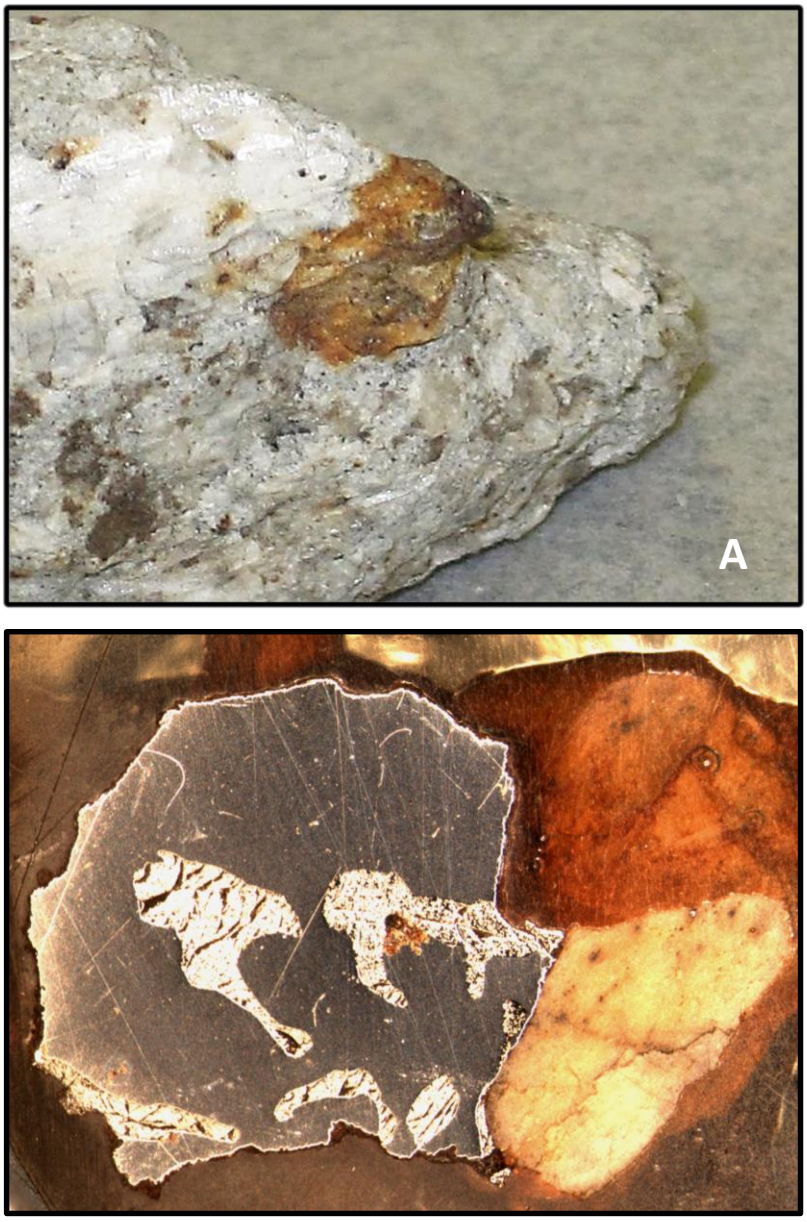

Figure 3.3: A. An image of the Norton County aubrite meteorite showing large enstatite crystals and metal nodules and blebs. B. Thick section of Mount Egerton showing both the metal and silicate phase. Aubrites were formed under reducing conditions and have significant Si in the metallic phase and minimal Fe in the enstatite as a result.

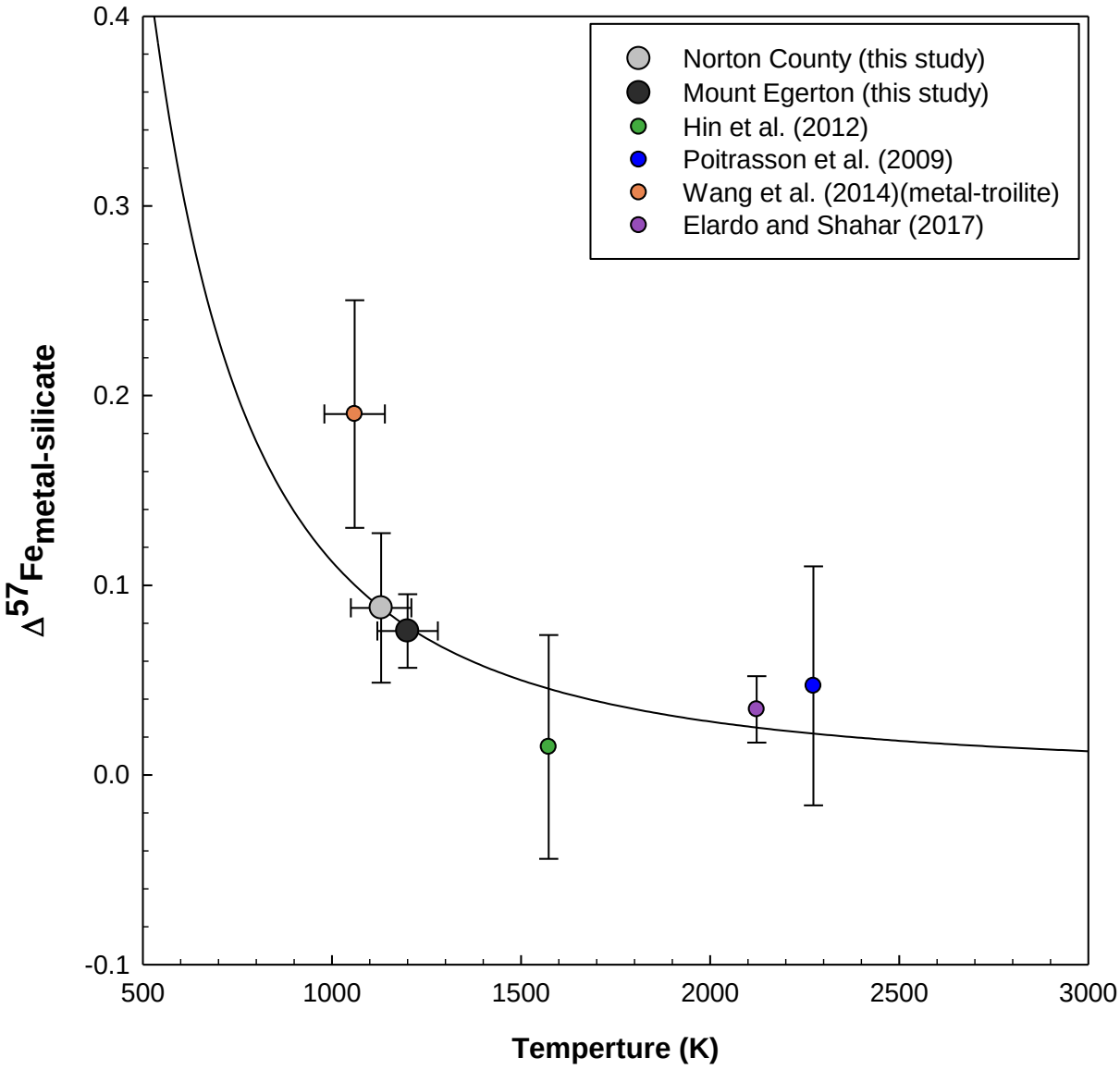

Figure 3.4: Aubrite $\Delta^{57}Fe_{metal\text{-}silicate}$ and accompanying temperature calibration. Experimental data measuring Fe metal-silicate equilibrium fractionation from several studies is plotted for reference, though direct comparison is difficult due to the varying parameters of the experiments. The metal-troilite fractionation measured by Wang et al. (2014) in natural samples is also plotted as metal-troilite fractionation is expected to be similar to metal-silicate fractionation (Polykov, 2007). Within error, our results are broadly consistent with the experimental data.

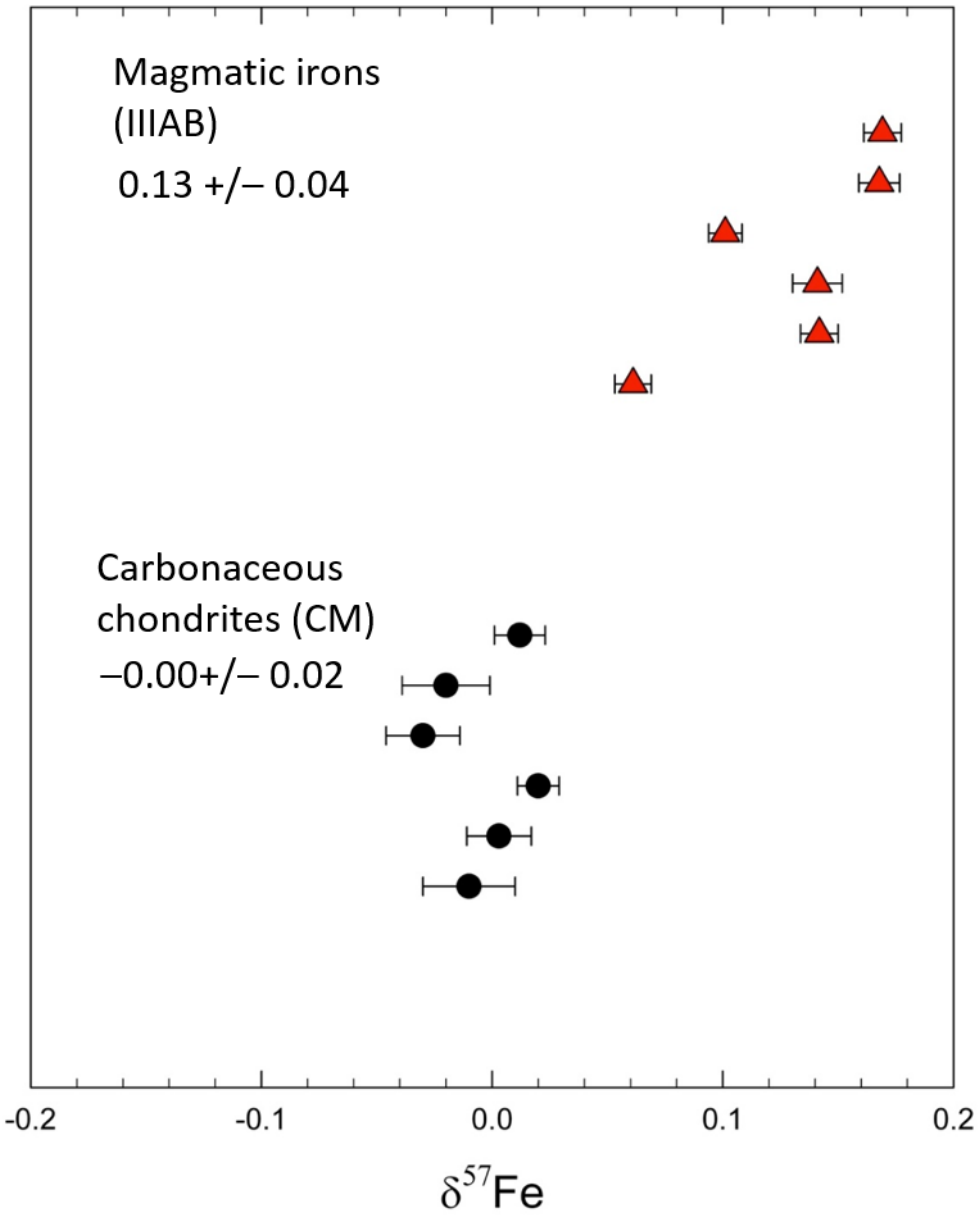

Figure 3.5: Fe isotope compositions for IIIAB iron meteorites and CM chondrites ThermoFinnigan Neptune™ MC-ICPMS at UCLA. The difference in composition measured in our lab is the same as that from the literature data, showing that magmatic iron meteorites are enriched in $^{57}Fe/^{54}Fe$ relative to chondrite.

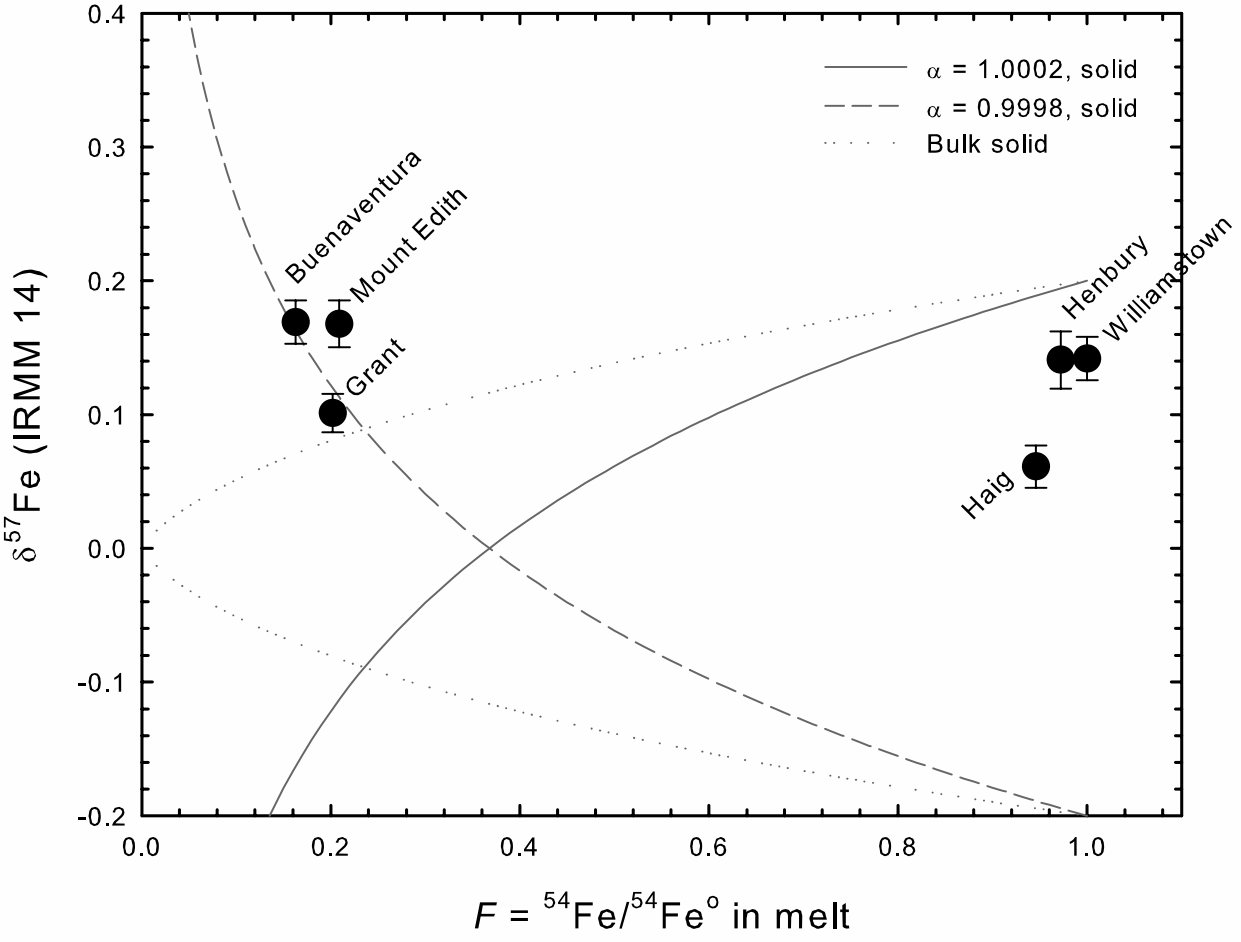

Figure 3.6: The IIIAB iron meteorite data measured in this study are plotted as a function of the degree of fractional crystallization. A value of F = 1 indicates that all Fe is in the melt, F = 0 indicates that all Fe is in the solid metal phase. The figure shows that there is no correlation between Fe isotope fractionation and degree of fractional crystallization. Also plotted are Rayleigh fractionation curves for a compatible element (α = 1.002) and an incompatible element (α = 0.9998). Again, we see that fractional crystallization does not affect Fe isotope composition as the early crystallizing solids do not fall on predicted curve.

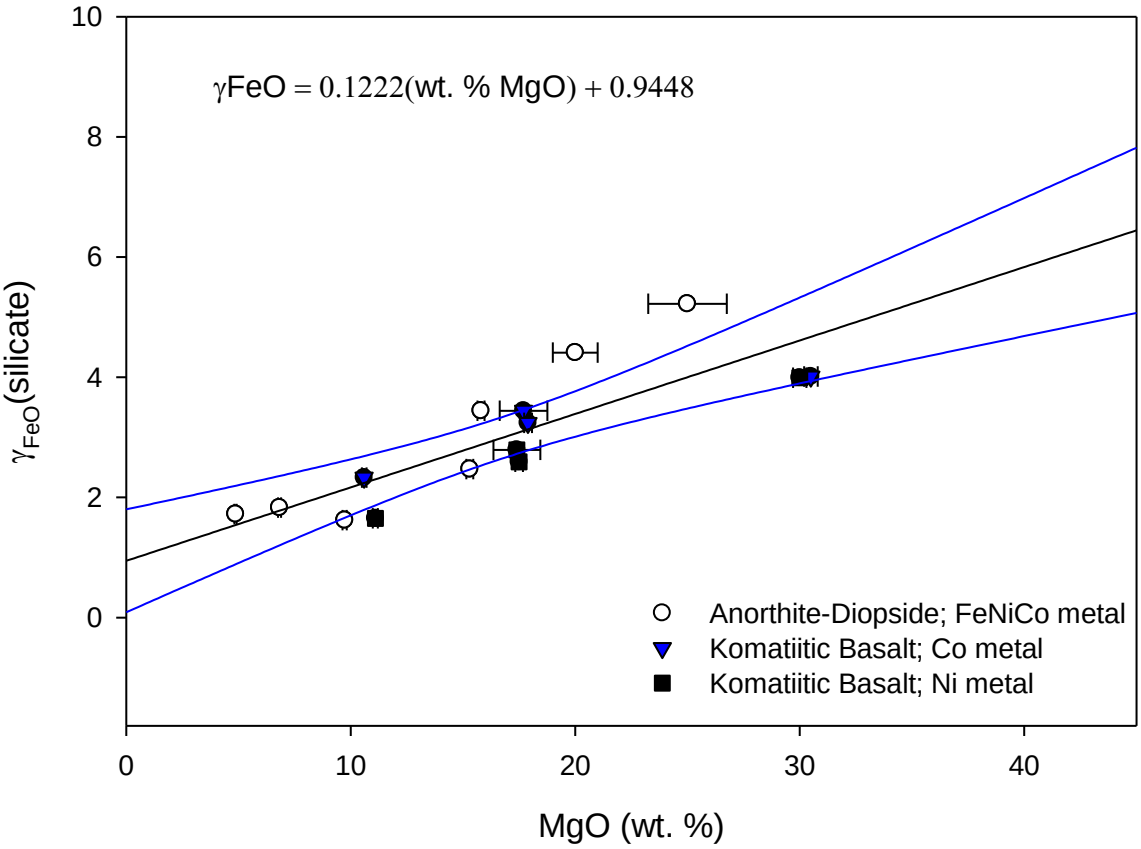

Figure 3.7: Activity coefficients for FeO in silicate as a function of the MgO content of the silicate. These data were measured in experiments by Holzheid et al. (1997). We use the data to estimate the appropriate activity coefficient for the aubrite meteorites, which have ~40 wt. % MgO in the silicate phase. This activity coefficient is then used in our equilibrium temperature calculation.

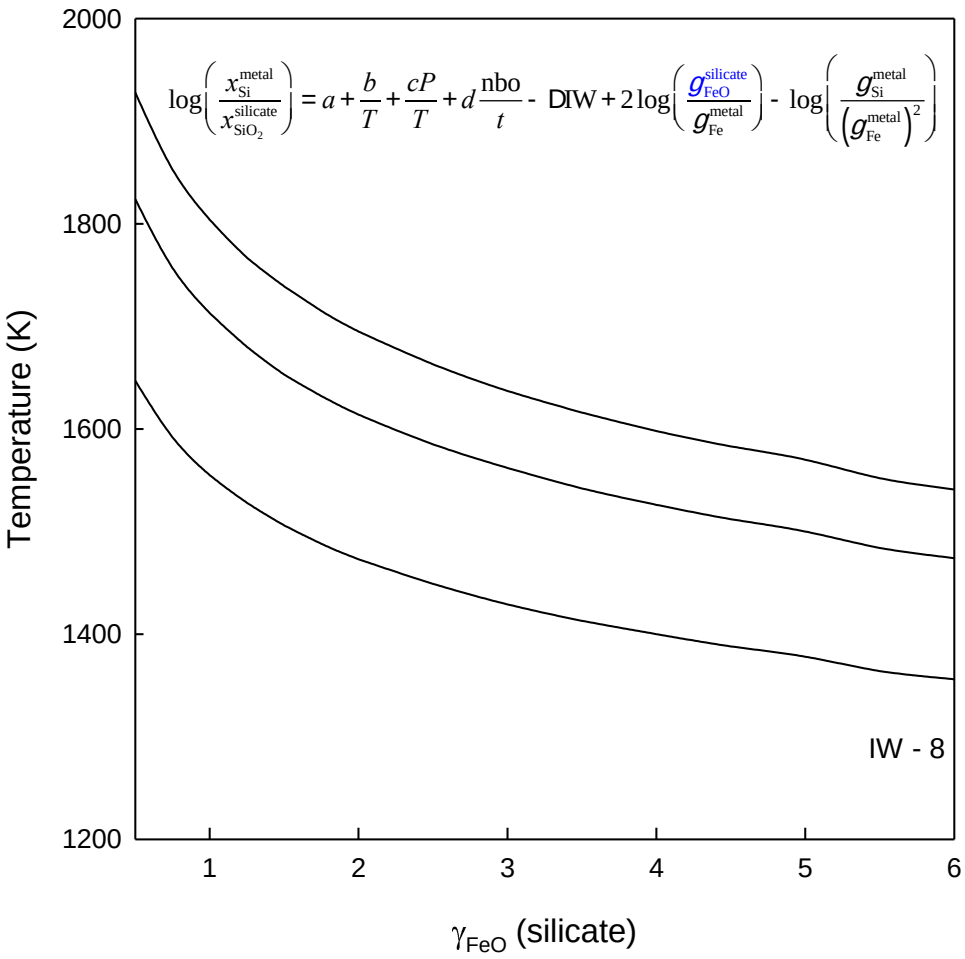

Figure 3.8: Using the displayed equation, we calculate the temperature of equilibration for the aubrite meteorites, Norton County and Mount Egerton, as a function of oxygen fugacity (curves) and the activity coefficient of Feo in the silicate melt (x axis). The shaded region shows the plausible regime of temperatures based on the likely values of the parameters in question. We consider a value of ~IW – 6.5 for the aubrite meteorites based on the literature data and value of 4 for the activity coefficient based off of the discussion in Corgne et al. (2008) to calculate our equilibration temperatures.

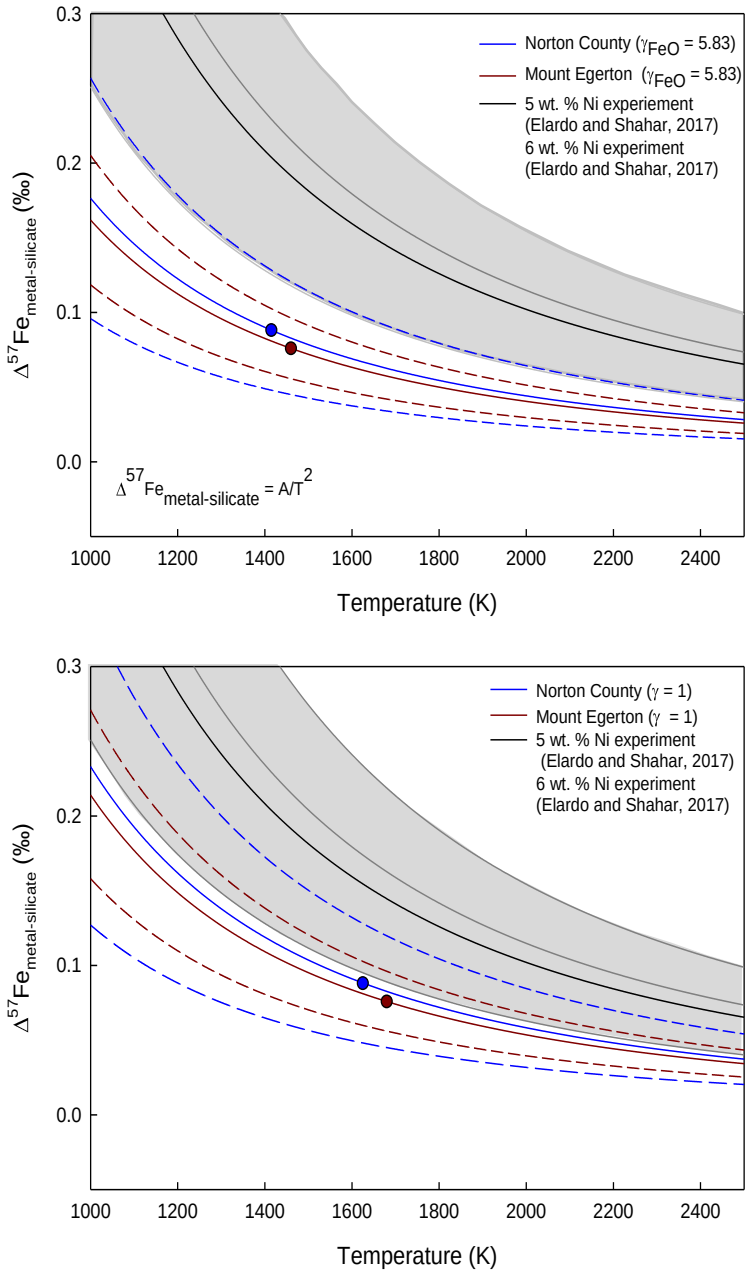

Figure 3.9: Comparison of Fe metal-silicate fractionation in natural samples (this study) and experiments (Elardo and Shahar, 2017). The curves are temperature calibrations using the measured fractionation. Here, we use the newly calculated temperatures of equilibration, 1415 K for Norton County and 1460 K for Mount Egerton. The dashed lines represent the uncertainty in temperature (uncertainty in $\gamma_{FeO}^{silicate}$) and the uncertainty in our measurement. For the temperature calibration, calculated using experimental data from Elardo and Shahar (2017) we choose a Ni content of 6 wt. %, which falls within the range for the aubrites in this study. Dashed lines for the experimental data reflect the uncertainty in the measured $\Delta^{57}Fe_{metal\text{-}silicate}$.

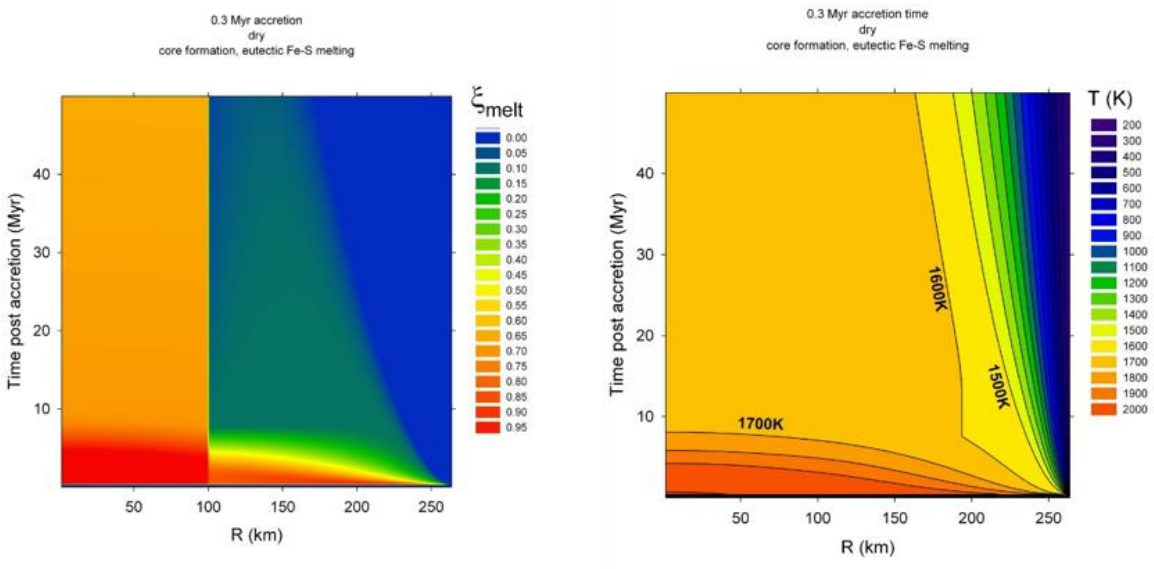

Figure 3.10: Thermal models for Vesta. The diagram on the right shows the melt fraction through time (post accretion) as a function of the radius of the body. The diagram on the left shows the temperature of the body through time as a function of radius. Based on these models we expect core-mantle equilibration to occur at temperatures >1700 K.

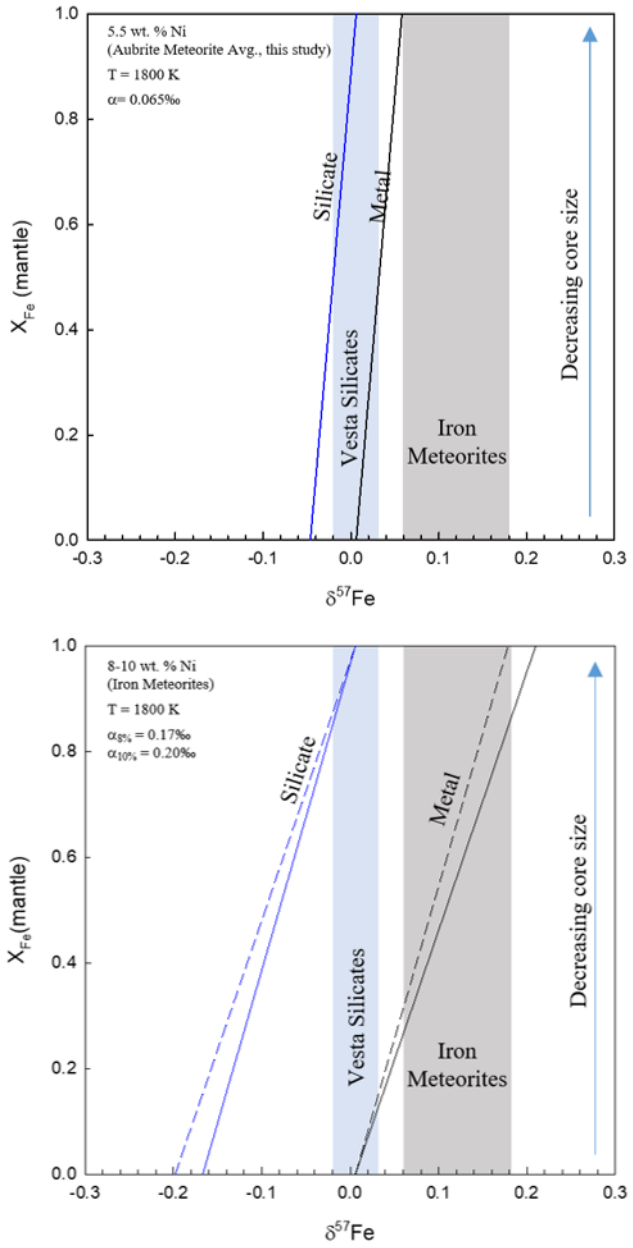

Figure 3.11: The measured Δ57Femetal-silicate can be used to assess if Fe isotope fractionation due to differentiation can explain the observed Fe isotope compositions of Solar System bodies. Here we show how the δ^{57}Fe of the metal and silicate phases varies as a function of core size as a result of the mole fraction of Fe that is present in the core vs. mantle. We use the temperature of equilibration for a Vesta sized body, 1800 K. The top panel uses the fractionation measured in the aubrite meteorites in this study. The bottom panel adjusts for the higher Ni content of iron meteorites and uses a larger α. Dashes lines are the case where Ni content is 8 wt. % and solid lines represent the case where Ni content is 10 wt. %.

Table 1

Sample	Type	Avg. Ni Content (wt. %)	$\delta^{57}Fe_{IRMM-14}$	2 S.E.	n
Norton County Metal	Aubrite	4.7	0.0304	0.0347	4
Norton County Silicate	Aubrite		-0.0577	0.0185	1
Mount Egerton Metal	Aubrite	6	0.0242	0.0154	2
Mount Egerton Silicate	Aubrite		-0.0517	0.0118	1
Haig	IIIAB Iron	7.32	0.0611	0.0157	1
Williamstown	IIIAB Iron	7.38	0.1418	0.0162	1
Henbury	IIIAB Iron	7.59	0.1410	0.0214	1
Grant	IIIAB Iron	9.29	0.1011	0.0145	1
Mount Edith	IIIAB Iron	9.37	0.1678	0.0177	1
Buenaventura	IIIAB Iron	9.77	0.1692	0.0161	1
Murchison	CM Chondrite		-0.010	0.041	1
Murchison	CM Chondrite		0.003	0.028	1
Murry	CM Chondrite		0.020	0.018	1
Murry	CM Chondrite		-0.030	0.031	1
Nagoya	CM Chondrite		-0.020	0.037	1
Nagoya	CM Chondrite		0.012	0.022	1

Table 3.1: Fe isotope meteorite data collected on the ThermoFinnigan Neptune™ MC-ICPMS at UCLA. Values for δ^{57}Fe are reported relative to the Fe standard IRMM-14. Ni content is listed for metallic phases as it affects fractionation and is an indicator of the degree of fractional crystallization in magmatic iron meteorites. The value for n indicates the number of samples that were separately dissolved from larger meteorite specimens; each dissolved sample was measured numerous times.

References

Baker, J. A., Schiller, M., and Bizzaro, M. 2012. ^{26}Al-^{29}Mg deficit dating ultramafic meteorites and silicate planetesimals differentiation in the early Solar System? GCA **77**: 415-431.

Barrat, J. A., Greenwood, R. C., Keil, K., Rouget, M. L., Boesenberg, J. S., Zanda, B., Franchi, I. A. 2016. The origin of aubrites: Evidence from lithophile trace element abundances and oxygen isotope compositions. GCA **192**: 29-48.

Berthet, S., Malavergne, V., and Righter, K. 2009. Melting of the Indarch Meteorite (EH4 Chondrite) at 1 GPa and variable oxygen fugacity: Implications for early planetary differentiation processes. GCA **73**: 6402-6420.

Casanova, I., K. Keil, and H.E. Newsom. 1993 Composition of metal in aubrites: Constraints on core formation. Geochemica et Cosmochemica Acta **57**: 675-682.

Chabot, N. L., and Jones, J. H. 2003. The parameterization of solid-liquid metal partitioning of siderophile elements. Met. & Planet. Sci. **38**: 1425-1436.

Clayton, R. N., and Mayeda, T. K. 1996. Oxygen isotope studies of achondrites. GCA **60**: 1999-2017.

Clayton, R. N., Mayeda, T. K., and Rubin, A. E. 1984. Oxygen isotopic compositions of enstatite chondrites and aubrites. JGR **89**: C245 – C249.

Craddock, P. R., and Dauphas, N. 2011. Iron isotope compositions of geological reference materials and chondrites. Geostand. Geoanal. Res. **35**: 101–123

Dauphas, N., Craddock, P.R., Asimow, P. D., Bennett, V. C., Nutman, A. P,, and Ohnenstetter, D. 2009. Iron isotopes may reveal the redox conditions of mantle melting from Archean to present. EPSL **288**: 255-267.

Dauphas, N., Pourmand, A., and Teng, F-Z. 2009. Routine isotopic analysis of iron by HR-MC-ICPMS: How precise and how accurate? Chem. Geol. **267**: 175-184.

Elardo, S. M. and Shahar, A. 2017. Non-chondritic iron isotope ratios in planetary mantles as a result of core formation. Nature Geoscience **10**: 317 – 321.

Goldstein, J. I., Scott, E. R. D., and Chabot N. L. 2009. Iron meteorite: Crystallization, thermal history, parent bodies and origin. Chemie der Erde 69: 293-325.

Hin, R. C., M. W. Schmidt and B. Bourdon (2012). Experimental evidence for the absence of iron isotope fractionation between metal and silicate liquids at 1 GPa and 1250-1300°C and its cosmochemical consquences. Geochemica et Cosmochemica Acta **77**: 164-181.

Hopp, T., Fischer-Gödde, M., and Klein, T. 2016. Ruthenium isotope fractionation during planetesimals core crystallization. LPSC XLVII, 1231.

Horn, I., von Blanckenburg, F., Schoenberg, R., Steinhoefel, G., and Markl, G. 2006. In situ iron isotope ratio determination using UV-femtosecond laser ablation with application to hydrothermal ore formation processes. GCA **70**: 3677-3688.

Kehm, K., Hauri, E. H., Alexander, C. M. O'D., and Carlson, R. W. 2003. High precision iron isotope measurements of meteoritic material by cold plasma ICP-MS. GCA **67**: 2879-2891.

Keil, K. 2010. Enstatite achondrite meteorites (aubrites) and the histories of their asteroidal parent bodies. Chem. Erde—Geochem. **70**, 295–317.

Laramir, J. W. 1968. Experimental studies on the system Fe-MgO-SiO_2-O_2 and their bearing on the petrology of chondritic meteorites. GCA **32**: 1187-1207.

McCall, G. J. H. 1965. A meteorite of unique type from Western Australia: The Mount Egerton stony-iron. Mineral Mag. **35**: 241-249.

McCoy, T.J., Dickinson, T.L., Lofgren, G.E., 1999. Partial melting of the Indarch (EH4) meteorite: a textural, chemical, and phase relations view of melting and melt migration. Meteorit. Planet. Sci. **34**, 735–746.

Okada, A., Keil, K., Taylor, J., Newsom, H., 1988. Igneous history of the aubrite parent asteroid—evidence from the Norton County enstatite achondrite. Meteoritics **23**, 59–74.

Poitrasson, F., Halliday, A.N., Lee, D., Levasseur, S., Teutsch, N. 2004. Iron isotope differences between Earth, Moon, Mars and Vesta as possible records of contrasted accretion mechanism. Earth and Planetary Science Letters **223**: 253-266.

Poitrasson, F., Levasseur, S., Teutsch, N. 2005. Significance of iron isotope mineral fractionation in pallasites and iron meteorites for the core-mantle differentiation of planets. Earth Planetary Science Letters **234**: 151-164.

Polyakov, V. B., Clayton, R. N., Horita, J., and Mineev, S. D. 2007. Equilibrium iron isotope fractionation factors of minerals: Reevaluation from the data of nuclear inelastic resonant X-ray scattering and Mössbauer spectroscopy. GCA **71**: 3833-3846.

Righter, K., Drake, M. J., and Scott, E (2006). Compositional Relationships Between Meteorites and Terrestrial Planets. In: Lauretta, D.S., McSween Jr., H.Y. (Eds.), Meteorites and the Early Solar System II. University of Arizona Press, Tucson, pp. 803–828. in collaboration with Lunar and Planetary Institute, Houston.

Schoenberg, R. and von Blanckenberg, F. 2006. Modes of planetary-scale Fe isotope fractionation. EPSL **252**: 342-359.

Scott, E. R. D. 1972. Chemical fractionation in iron meteorites and its interpretation. GCA **36**: 1205-1236

Scott, E. R. D. and Wasson, J. T. 1975. Classification and properties of iron meteorites. Reviews of Geophysics and Space Physics **13**: 527 – 546.

Shahar, A., Hillgren, V.J., Horan, M.F., Mesa-Garcia, J., Kaufman, L.A., and Mock, T.D., 2015. Sulfur-controlled iron isotope fractionation experiments of core formation in planetary bodies. GCA **150**, 253-264.

Shahar, A., V. J. Hillgren, E.D. Young, Y. Fei, C. A. Macris and L. Dent (2011). High-temperature Si isotope fractionation between iron metal and silicate. Geochemica et Cosmochemica Acta **75**: 7688 7697.

Shahar, A., and Young, E.D., 2007. Astrophysics of CAI formation as revealed by silicon isotope LA-MC ICPMS of an igneous CAI. Earth and Planetary Science Letters 257, 497-510.

Shahar, A., K. Ziegler, E. D. Young, A. Ricolleau, E. A. Schauble and Y. W. Fei (2009). Experimentally determined Si isotope fractionation between silicate and Fe metal and implications for Earth's core formation. Earth and Planetary Science Letters **288**: 228-234.

Toplis, M. J., Mizzon, H., Monnereau, M., Forni, O., McSween, H. Y., Mittlefehldt, D. W., McCoy, T. J., Prettyman, T. H., De Sanctis, M. C., Raymond, C. A., and Russell, C. T. 2013. Chondritic models of 4 Vesta: Implications for geochemical and geophysical properties. Met. & Planet. Sci. **48**: 2300-2315.

Wade, J. and B. J. Wood. 2005. Core formation and the oxidation state of the Earth. Earth and Planetary Science Letters **236**: 78-95

Wait, C. M. 1970. The metal phase of Horse Creek, Mount Egerton, and Norton County enstatitic meteorites. Mineral. Mag. **37**: 905-908

Wang, K., Moynier, F., Dauphas, N., Barrat, J-A., Craddock, P., Sio, C. K. 2012. Iron isotope fractionation in planetary crusts. GCA **89**: 31-45.

Wang, K., Savage, P. S., and Moynier, F. 2014. The iron isotope composition of enstatite meteorites: Implications for their origin and the metal/sulfide Fe isotopic fractionation factor. GCA **142**: 149-165.

Wasson, J. T. 1999. Trapped melt in IIIAB irons; solid/liquid elemental partitioning during the fractionation of the IIIAB magma. GCA **63**: 2875- 2889.

Wasson, J. T., Choi, B., Jerde, E. A., and Ulff-Moller, F. 1998. Chemical classification of iron meteorites: XII. New members of the magmatic groups. GCA **62**: 715-724.

Wasson, J. T., G. W. Kallemeyn and A. E. Rubin. 1994. Equilibration temperatures of EL chondrites: A major downward revision in the ferrosilite contents of enstatite. Meteoritics **29**: 658-662.

Wasson, J. T., and Wai, C. M. 1970. Composition of metal, schreibersite, and perryite of enstatite achondrites and the origin of enstatite chondrites and achondrites. GCA **34**: 169-184.

Watters T. R. and M. Prinz (1979). Aubrites: Their origin and relationship to enstatite chondrites. 10th Lunar and Planetary Science Conference, pp 1073-1093.

Watters, T.R., Prinz, M., 1980. Mt. Egerton and the aubrite parent body. LPSC XI, pp. 1225–1227.

Watters, T.R., Prinz, M., Rambaldi, E.R., Wasson, J.T., 1980. ALHA 78113, Mt. Egerton and the aubrite parent body. Meteoritics **15**, 386.

Weyer, S., A. D. Anbar, G. P. Brey, C. Muncker and A. B. Woodland (2005). Iron isotope fractionation during planetary differentiation. Earth and Planetary Science Letters **240**: 251-265.

Weyer, S. and D. A. Ionev (2007). Partial melting and melt percolation in the mantle: the message from Fe isotopes. Earth and Planetary Science Letters **259**: 119-133.

Williams, H. M., Markowski, A., Quitté, G., Halliday, A. N., Teutsch, N., and Levasseur, S. 2006. Fe isotope fractionation in iron meteorites: New insights into metal-sulphide segregation and planetary accretion. EPSL **250**: 486-500.

Wolf, R., Ebihara, M., Richter, G. R., and Anders, E. 1983. Aubrites and diogenites: Trace element clues to their origin. GCA **47**: 2257-2270.

Wood, B. J. and Wade, J. 2013. Activities and volatilities of trace components in silicate melts: a novel use of metal-silicate partitioning data. Mineral Petrol. **166**: 911-921.

Zhou, Q., Q.-Z.Yin, E. D. Young, X.-H. Li, F.-Y. Wu, Q.-L. Li, Y. Liu and G.-Q. Tang (2013). SIMS Pb-Pb and UPb age determination of eucrite zircons at < 5 μm scale and the first 50 Ma of thermal history of Vesta. Geochemica et Cosmochimica Acta **110**: 152-175.

Zhu, X.K., Guo, Y., Williams, R.J.P., O'Nions, R.K., Matthews, A., Belshaw, N.S., Canters, G.W., de Waal, E.C., Weser, U., Burgess, B.K., Salvato, B. 2002. Mass fractionation processes of transition metal isotopes. Earth and Planetary Science Letters **200**: 47-62

Ziegler, K., E. D. Young, E.A. Schauble and J.T. Wasson (2010). Metal-silicate silicon isotope fractionation in enstatite meteorites and constraints on Earth's core formation. Earth and Planetary Science Letters **295**: 487-496.